Title

ANGLE-RESOLVED PHOTOELECTRON SPECTROSCOPY APPLIED TO THE DETERMINATION OF THE SURFACE ELECTRONIC STRUCTURE OF CRYSTALLINE METALS

Author

Williams, Richard Stanley.

Publication Date

1978-05-01

LBL-7676

ANGLE-RESOLVED PHOTOELECTRON SPECTROSCOPY APPLIED TO THE DETERMINATION OF THE SURFACE ELECTRONIC STRUCTURE OF CRYSTALLINE METALS

Richard Stanley Williams
(Ph. D. thesis)

May 1978

Prepared for the U. S. Department of Energy
under Contract W-7405-ENG-48

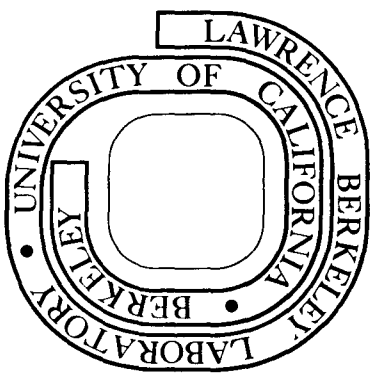

LBL-7676

DISCLAIMER

ANGLE-RESOLVED PHOTOELECTRON SPECTROSCOPY APPLIED TO THE DETERMINATION OF THE SURFACE ELECTRONIC STRUCTURE OF CRYSTALLINE METALS

Contents

ANGLE-RESOLVED PHOTOELECTRON SPECTROSCOPY APPLIED TO THE DETERMINATION OF THE SURFACE ELECTRONIC STRUCTURE OF CRYSTALLINE METALS

Richard Stanley Williams

ABSTRACT

The experimental determination of solid state electronic band structure has been shown to be feasible through angle resolved photoelectron spectroscopic (ARPES) studies of the valence bands of oriented copper single crystals. In order to assign features observed in ARPES spectra to solid state energy bands, the theoretical description of the photoemission process must be understood in detail. For this purpose, the influence of the excitation process, hot electron transport, and surface effects on observed spectra are considered carefully. First, photoemission from atomic neon is examined theoretically to learn the nature of the continuum final state and its relationship to the total and differential atomic cross-sections. The directionality of the band-like final states in a crystalline solid is then determined by examining ARPES spectra collected from Cu single crystals. Inelastic scattering processes in a solid cause attenuation of photocurrent, which is studied by studying the surface sensitivity of plasmon loss satellites in photoemission spectra of Al and In. The effect of photocurrent damping on ARPES valence band spectra of copper

is then investigated by examining the relaxation of crystal momentum selection rules with increased surface sensitivity. The presence of the surface itself is important in determining angular distributions, as shown by measurements of photoelectron refraction. Photoemission is also possible from states localized at the surface, and examples of surface state photoemission are found from the (111) and (211) surfaces of copper. Finally, the dynamic effects of thermal lattice disordering are shown to be extremely important in photoemission studies applied to band structure determinations, as electron-phonon interactions can suppress the information content of an ARPES spectrum drastically.

I. INTRODUCTION

The study of electronic structure and the relationship of electronic to physical and functional properties of matter are themes of major importance in chemistry. Most modern techniques used for the elucidation of electronic structural information are spectroscopic in nature; they deal with observation of the interaction of a portion of the electromagnetic spectrum with the system to be studied. In most cases, the physical property of a system being studied can not be observed directly, but must be inferred indirectly by the observation of a somewhat related spectroscopic property of the system. Photoelectron spectroscopy (PES), however, provides a rather clear picture of the quantum mechanical electronic level structure of matter, and is very closely related to the development of quantum mechanics itself.[1]

Physically, photoelectron spectroscopy is the measurement of photoelectric current as a function of the kinetic energy of the electrons emitted by a sample irradiated with a constant energy photon beam. The kinetic energy (E_{kin}) of detected photoelectrons may be related to the initial state energy (or binding energy, E_B) levels of the material studied by the conservation of energy condition

$$E_B = h\nu - E_k \qquad (1)$$

where $h\nu$ is the energy of the incident radiation. Thus, an electronic energy level is detected in PES as a peak in the photoelectron current versus energy distribution curve (EDC). Since the final state observed is a continuum state of the system, the portion of the electromagnetic

spectrum which may be used for PES studies extends from the ultraviolet well into the hard x-ray regime (where Compton scattering and e^--p^+ pair production become important[2]). Traditionally, the field of photoemission has been segmented into two subdivisions due to the limited number of photon source available; the ultraviolet PES regime (or UPS) utilized radiation created in gas discharges ($h\nu \leqslant 40.8$ eV) and the x-ray PES regime (or XPS) relied on emissions from standard x-ray tubes ($h\nu \geqslant 1254$ eV). However, the advent of continuously tunable synchrotron radiation sources is acting to close the photon energy gap and obscure the division into two separate research areas.

Over the past decade avances in technology have allowed great improvements in experimental technique to collect, and theoretical appreciation to interpret, PES data. Perhaps the most important contributions have been in the areas of vacuum technology, which allows better control of the sample and experimental parameters, and the introduction of large capacity, high speed computers, which enable extensive comparison between theoretical models and experimental data. This interaction between theory and experiment has been the essential driving force which has propelled PES to its present level of sophistication.

The detailed application of photoemission theory to atomic systems has been described by Fano and Cooper.[3] In particular, the photoelectron cross sections, both total and differential, have been shown to be extremely sensitive to the initial and final atomic wavefunctions. Thus, the measurement of atomic photoelectron cross sections as a function of excitation energy and emission angle is potentially a very

powerful technique for determining the ground state charge distribution of atomic species. Chapter II of this dissertation, which acts as an introduction to the photoemission process, investigates the nature of the final state in a photoemission transition involving a single atomic center; the specific example chosen is neon. Several approximations to the continuum state are tested, and it is found that excellent agreement between experimental and calculated absolute and differential cross sections for neon can be obtained for the proper choice of final state wave function. Due to the extreme accuracy with which atomic continuum states may be determined, atomic photoemission is extremely well understood.

The level of general understanding is quite different for photoemission from solids, although interest in solid state photoemission is intense as demonstrated by the number of recent theoretically related articles[4,5,6] and review monographs[7,8] appearing on the subject. The essential aspects of angle-resolved PES (ARPES) as applied to crystalline solids were presented by Mahan[9] in 1970, but only recently has the theory presented then become fully appreciated. The remainder of this thesis is devoted to considering various aspects of the extremely involved theory of ARPES spectra from the valence band region of single crystalline solids and providing experimental verification and clarification of the points raised.

In Chapter III the peak structure of valence band ARPES of Cu single crystals is interpreted in terms of a simple model which only considers single electron excitations to a free-electron-like final

state band structure of an infinite solid. This model explains the energy positions of the spectra quite well. Experimental demonstrations of many body effects on solid state photoemission spectra are presented in Chapter IV, which considers photoelectron finite mean-free paths in solids and their influence on plasmon loss features observed in PES spectra of Al and In. Chapter V reveals how the simple direct transition model outlined in Chapter III is modified by the presence of a surface and attentuation of photoelectric current during transport through the crystal to the surface. The effect of these factors is to introduce a crystal momentum broadening into the final states of the transition and consequently increase the number of initial states sampled in the ARPS valence band spectrum. The effect of the surface itself is considered in Chapter VI; in particular measurements of the amount of refraction suffered by a photoelectron crossing the solid-vacuum interface at Cu(100) and (111) surfaces are presented. Photoemission from electronic states localized at Cu (111) and (211) single crystal surfaces is considered in Chapter VII. Finally, Chapter VIII investigates the nature of the temperature dependence of ARPES spectra of copper and shows that electron-phonon interactions break down the solid state crystal momentum selection rules at elevated temperatures.

The emphasis of this thesis is the experimental demonstration of several of the major factors influencing photoemission from solids. Several effects have been neglected;primary among them the influence of the Auger lifetime of the hole left by the photoelectron on the experimental spectra. The work presented in this thesis builds upon and is

complementary to the dissertations of Kowalczyk[10] and McFeely.[11] Although primarily an experimental thesis, detailed descriptions of the equipment and procedures utilized for the research presented here are omitted for brevity, as they have already been covered thoroughly by Apai[12] and Wehner,[13] who collaborated in most of these investigations.

REFERENCES

1. J. G. Jenkin, R. C. G. Leckey and J. Liesegang, J. Electron Spectrosc. Relat. Phenom. 12, 1 (1977).

2. W. Heitler, The Quantum Theory of Radiation (Oxford University Press, London, 1954).

3. U. Fano and J. W. Cooper, Rev. Mod. Phys. 40, 441 (1968).

4. P. J. Feibelman and D. E. Eastman, Phys. Rev. B10, 4932 (1974).

5. B. Feuerbacher and R. F. Willis, J. Phys. C 9, 169 (1976).

6. J. B. Pendry, Surf. Sci. 57, 679 (1976).

7. M. Cardona and L. Ley, editors, Photoelectron Spectroscopy of Solids (Springer-Verlag, Heidelberg, 1977).

8. A. D. Baker and C. R. Brundle, editors, Electron Spectroscopy: Theory, Techniques, and Applications (Academic Press, New York, 1977).

9. G. D. Mahan, Phys. Rev. B2, 4334 (1970).

10. S. P. Kowalczyk, Ph.D. Thesis, University of California, Lawrence Berkeley Laboratory Report, LBL-4319 (1976) unpublished.

11. F. R. McFeely, Ph.D. Thesis, University of California, Lawrence Berkeley Laboratory Report, LBL-5414 (1976) unpublished.

12. G. R. Apai, Ph.D. Thesis, University of California, Lawrence Berkeley Laboratory Report, LBL-6906 (1977), unpublished.

13. P. S. Wehner, Ph.D. Thesis, University of California (1978), unpublished.

II. DIFFERENTIAL PHOTOEMISSION CROSS SECTIONS OF Ne*

Observation of photoemission spectra provides detailed information about both the initial and final electronic structure of the system under study. Energy and angular dependent studies of photoemission cross sections made possible by several new photon sources, especially synchrotron radiation, can provide a sensitive probe of gaseous species, liquids, solid surfaces, and adsorbates. However, in order to interpret PES in terms of electronic structure a good model of the transition from initial to final states is necessary.

The detailed many-electron theory of photoemission for gaseous atomic species is well known.[1] Recently, steps have been taken to formulate viable theories of photoemission for molecular species[2] and solid surfaces.[3] In many cases, these approaches consider one-electron transitions to final continuum states that are approximated by a plane wave (PW) or an orthogonalized plane wave (OPW).[4] The validity of calculations employing PW or OPW continuum functions and neglecting final state relaxation must be established before they may be applied to the interpretation of experimental results that are now appearing.

This chapter presents photoemission cross sections and asymmetry parameters[5] for the 1s, 2s, and 2p orbitals of neon, calculated by several methods. Intercomparisons of these results and comparison with experiment are utilized to ascertain the validity of the various approximations employed. Chapter II.A focuses on various approximations to continuum functions; Chapter II.B deals with the effects of final state

relaxation. Further discussion concerning the relation of photoemission cross sections to ground state wave functions (charge distributions) appears in Chapter II.C.

A. Atomic Continuum Wavefunctions

The final state of a photoemission transition is of special interest because at least one electron of the system under study is in the continuum. In this section the differential photoemission cross section $d\sigma(\varepsilon)/d\Omega$ of neon, calculated using plane wave (PW), orthogonalized plane wave (OPW), and Hartree-Fock (HF) continuum functions are compared with experiment. The rationale for this comparison is to test the sensitivity of photoemission cross sections to the form of the final state continuum function and to evaluate the accuracy of the PW and OPW approaches. It is shown that calcualted neon cross sections depend strongly on the model used for the continuum state and that both the PW and OPW models are quite poor approximations for those continuum states which exhibit large phase shifts.

Following Cooper and Manson,[6] the differential photoemission cross section from the $n\ell^{th}$ shell of an atom as a function of final state continuum electron kinetic energy ε in the dipole approximation is

$$\frac{d\sigma_{n\ell}(\varepsilon)}{d\Omega} = \frac{\sigma_{n\ell}(\varepsilon)}{4\pi}\left[1 - \frac{1}{2}\beta(\varepsilon)\ P_2(\cos\theta)\right] \quad , \qquad (1)$$

where θ is the angle between an incident beam of unpolatized radiation and the photoelectron wave vector. In the one electron partial wave approximation the total cross section is

$$\sigma_{n\ell}(\varepsilon) = \frac{\omega(2\pi)^2 e^2 \hbar^2}{c} \frac{N_{n\ell}}{3(2\ell+1)} \left[\ell\left(R_{n\ell}^{\varepsilon\ell-1}\right)^2 + (\ell+1)\left(R_{n\ell}^{\varepsilon\ell+1}\right)^2\right] \quad (2)$$

where ω is the angular frequency of the incident radiation, $N_{n\ell}$ is the occupation number of the $n\ell^{th}$ subshell, and the $R_{n\ell}^{\varepsilon\ell\pm1}$ are defined in the dipole length and velocity formulations by

$$R_{n\ell}^{\varepsilon\ell\pm1} = \int_0^\infty P_{\varepsilon\ell\pm1}(r)\ rP_{n\ell}(r)\ dr = \quad (3)$$

$$\frac{1}{M_e\omega}\int_0^\infty P_{\varepsilon\ell\pm1}(r)\left(\frac{d}{dr} + \frac{2\ell+1\pm1}{2r}\right) P_{n\ell}(r)\ dr \quad .$$

The continuum functions $P_{\varepsilon\ell}(r)$ are normalized to a Dirac delta function in ε.[7]

The asymmetry parameter[8] $\beta(\varepsilon)$ is given by

$$\beta(\varepsilon) = \quad (4)$$

$$\frac{\ell(\ell-1)\left(R_{n\ell}^{\varepsilon\ell-1}\right)^2 + (\ell+1)(\ell+2)\left(R_{n\ell}^{\varepsilon\ell+1}\right)^2 - 6\ell(\ell+1)\left(R_{n\ell}^{\varepsilon\ell-1}\right)\left(R_{n\ell}^{\varepsilon\ell+1}\right)\cos\left(\xi_{\ell+1}-\xi_{\ell-1}\right)}{(2\ell+1)\left[\ell\left(R_{n\ell}^{\varepsilon\ell-1}\right)^2 + (\ell+1)\left(R_{n\ell}^{\varepsilon\ell+1}\right)^2\right]}$$

for continuum function phase shifts $\xi_{\ell\pm1}(\varepsilon)$ in the $\ell \pm 1$ channel defined for scattering from a nonzero potential.

In this formulation two outgoing channels for the photoelectron are explicitly defined by dipole selection rules. The total photoelectron flux depends only upon the sum of the electron fluxes in the

two channels, but the angular dependence of intensity is sensitive to the interference between the channels. Thus the phase shifts $\xi_{\ell\pm1}(\varepsilon)$ can have a significant effect upon the angular distribution of photoelectron flux.

Utilizing the Rayleigh expansion,[9] a PW can be expressed as a superposition of spherical waves, each with its associated n and ℓ values. The normalized radial component of the PW ℓ channel is

$$P^{PW}_{\varepsilon\ell}(r) = \sqrt{\frac{2M_e k}{\pi\hbar^2}}\, r j_\ell(kr) \qquad (5)$$

$$\xrightarrow{r\to\infty} \sqrt{\frac{2M_e}{\pi\hbar^2 k}}\, \sin\left(kr - \frac{1}{2}\ell\pi\right) \quad .$$

where $j_\ell(kr)$ is a Spherical Bessel Function. In this zeroth order Born approximation the effect of the atomic potential on the photoelectron is completely ignored. One way to introduce an effective atomic potential[10] is to Schmidt orthogonalize the PW orbital to the bound states of the system. The radial component of the OPW is then

$$P^{OPW}_{\varepsilon\ell} = \sqrt{\frac{2M_e k}{\pi\hbar^2}} \left\{ r j_\ell(kr) - \sum_{\ell'=\ell} \int_0^\infty P_{n'\ell'}(r)\, r j_\ell(kr)\, dr P_{n'\ell'}(r) \right\} \qquad (6)$$

where the summation is taken over all bound states with the same angular momentum quantum number as the continuum channel. This orthogonalization alters the wavefunction near the origin but has no effect on its delta function normalization or asymptotic form (i.e., no phase shift

is introduced).

A more exact method of including the effect of the atomic potential is to require that the continuum function be an eigenfunction of the atomic Hamiltonian. In this study the single particle Hartree-Fock equation including Lagrange multipliers to assure orthogonality to the bound states was integrated numerically for the given atomic configuration[11] and photoelectron kinetic energy ε. The asymptotic form of these numerical solutions is

$$P^{HF}_{\varepsilon\ell}(r) \xrightarrow[r\to\infty]{} \sqrt{\frac{2M_e}{\pi\hbar^2 k}} \sin\left(kr - \frac{1}{2}\ell\pi - \frac{e^2 M_e}{\hbar^2 k}\ln 2kr + \xi_\ell(\varepsilon)\right) \quad , \tag{7}$$

where

$$\xi_\ell(\varepsilon) = \delta_\ell(\varepsilon) + \sigma_\ell(\varepsilon) \quad , \tag{8}$$

$$\sigma_\ell(\varepsilon) = \arg\Gamma\left(\ell + 1 - i\frac{e^2 M_e}{\hbar^2 k}\right) \tag{9}$$

and $\delta_\ell(\varepsilon)$ is the phase shift of the HF continuum function with respect to the regular Coulomb wavefunction. The wavefunctions were generated using Bates' program[12] modified to yield phase shifts.[13] The bound state orbitals used were those of Bagus.[14]

The partial wave approach for the PW and OPW cross section calculations was used to allow a direct comparison with the more exact HF results. Another mathematically equivalent formulation utilizes the fact that a plane wave is an eigenfunction of the momentum operator.[15] The dipole velocity transition matrix element is proportional to the product of the magnitude of the electron wave vector and the Fourier

transform of the initial-state orbital. Including the constraint of orthogonality to the bound state orbitals yields the cross section section

$$\sigma_T(\varepsilon) = \frac{8\pi e^2 k}{3M_e c\omega} \frac{N_{n\ell}}{(2\ell+1)} \left\{(2\ell+1)\, k^2 f_{n\ell}^2 + \ell\left(G_{\ell-1}^2 + 2kf_{n\ell}G_{\ell-1}\right) + (\ell+1)\left(G_{\ell+1}^2 - 2kf_{n\ell}G_{\ell+1}\right)\right\} \quad (10)$$

and the asymmetry parameter

$$\beta(\varepsilon) = \left[2(2\ell+1)^2 k^2 f_{n\ell}^2 + \ell(\ell-1)\left(G_{\ell-1}^2 + 2kf_{n\ell}G_{\ell-1}\right) + (\ell+1)(\ell+2)\left(G_{\ell+1}^2 - 2kf_{n\ell}G_{\ell+1}\right) + 6\ell(\ell+1)(kf_{n\ell}G_{\ell-1} - kf_{n\ell}G_{\ell+1} - G_{\ell-1}G_{\ell+1})\right] / \quad (11)$$

$$\left\{(2\ell+1)\left[(2\ell+1)\, k^2 f_{n\ell}^2 + \ell\left(G_{\ell-1}^2 + 2kf_{n\ell}G_{\ell-1}\right) + (\ell+1)\left(G_{\ell+1}^2 - 2kf_{n\ell}G_{\ell+1}\right)\right]\right\},$$

where

$$f_{n\ell} = \int_0^\infty r j_\ell(kr)\, P_{n\ell}(r)\, dr \quad (12)$$

and

$$G_{\ell\pm1} = \sum_{n'} \int_0^\infty r j_{\ell\pm1}(kr)\, P_{n'\ell\pm1}(r)\, dr \int_0^\infty P_{n'\ell\pm1}(r) \left(\frac{d}{dr} + \frac{2\ell+1\pm1}{2r}\right) P_{n\ell}(r)\, dr \quad (13)$$

for photoemission from the $n\ell^{th}$ one-electron orbital and the summation extending over the bound orbitals with the same symmetry as the $\ell \pm 1$ continuum channel.

From Eq. (11) it is seen that $\beta(\varepsilon) = 2$ for plane wave photoionization independent of the energy ε and the symmetry of the initial bound state. In the OPW case, β can assume values other than 2, but must approach 2 in the limit of large k. The remaining discussion of PW and OPW cross sections will deal with the partial-wave form. In these cases, the velocity and length total cross sections have the same qualitative appearance, but the length calculations yield cross sections an order of magnitude greater than the velocity results. The PW and OPW length results are excluded from the following discussion.

Comparisons of $\sigma_{n\ell}(\varepsilon)$ and $\beta_{2p}(\varepsilon)$ calculated for the various continuum wavefunction approximations with experiment are shown in Figs. 1-4. The PW and OPW calculations give poor results for 1s and 2s photoemission, but the 2p total cross section results are qualitatively correct. However, the angular dependence given by the PW and OPW calculations for 2p photoemission is totally incorrect. The different HF continuum function calculations agree very well with experiment, and will be more thoroughly discussed in Chapter II.B. In the remainder of Chapter II.A the PW and OPW results are discussed.

For 1s photoemission (Fig. 1), the PW velocity cross section rises slowly by several orders of magnitude from threshold to a maximum near a photon energy of 1400 eV and then falls gradually at higher energies. The OPW calculation is closer to the observed cross section at threshold, but then falls to a spurious local minimum at about 1050 eV and rises from there to approach the PW cross section asymtotically. The PW and OPW results are qualitatively incorrect for $h\nu < 1500$ eV and

have not attained the correct slope at $h\nu$ = 2000 eV. Orthogonalization of the plane wave for the $1s \rightarrow \varepsilon p$ photoemission channel does not improve the calculated cross section over the PW case.

The $2s \rightarrow \varepsilon p$ channel (Fig. 2) shows large increases in cross section at threshold and spurious minima for both PW and OPW calculations. Again the slope at high photon energy is too gradual and the OPW result is no better than the PW result.

The $2p \rightarrow (\varepsilon s, \varepsilon d)$ PW and OPW calculations (Fig. 3) are quite close to both the HF and experimental results. The PW and OPW values are too large at higher energies, but they appear to have the correct limiting slope. Orthogonalization of the εs channel to the 1s and 2s occupied orbitals appears to have improved the agreement with experiment considerably in the medium energy range. Finally, both PW and OPW cross sections are fair even close to threshold.

However, the $\beta_{2p}(\varepsilon)$ value calculated by Eq. (4) is 2, as predicted by Eq. (11). The OPW $\beta_{2p}(\varepsilon)$ results are also in serious disagreement with experiment. Thus, although OPW and PW closely predict the 2p total cross section, they fail badly in describing the <u>differential</u> cross section.

These findings may be interpreted in terms of the behavior of the continuum functions in the region of space where the bound atomic states have appreciable amplitude; this behavior being correlated with the phase shifts of the "actual" continuum functions. An illustration of this effect is offered in Fig. 5. Here are presented the radial parts of the HF and PW continuum functions for 1s photoionization at $h\nu$ = 1100 eV,

near the region where OPW theory predicts a spurious minimum in the cross section. Although the shape of the two continuum functions is virtually identical after the first period there is a significant positive phase shift of the HF continuum function with respect to the plane wave. This phase shift reflects the different behavior of the two wavefunctions near the nucleus. It can be seen that the HF continuum function is orthogonal to the 2p radial wavefunction (the overlap integral is less than 10^{-5}). It is also fairly obvious that orthogonalizing the plane wave to the 2p wavefunction will decrease the PW amplitude in the region where the 1s radial function is large, thus resulting in a very small transition matrix element. This result is independent of the relative phases of the wavefunctions involved. An analytical illustration of this result is obtained by writing Eq. (6) in the simple form

$$|\mathrm{OPW}\rangle = |\mathrm{PW}\rangle - \langle 2p|\mathrm{PW}\rangle|2p\rangle, \tag{14}$$

then calculating $\langle 1s|\vec{\nabla}|\mathrm{OPW}\rangle$, which will be minimal in the energy range for which

$$\langle 1s|\vec{\nabla}|\mathrm{PW}\rangle \approx \langle 1s|\vec{\nabla}|2p\rangle\langle 2p|\mathrm{PW}\rangle. \tag{15}$$

Now $\langle 1s|\vec{\nabla}|2p\rangle$ is a constant, while $\langle 1s|\vec{\nabla}|\mathrm{PW}\rangle$ and $\langle 2p|\mathrm{PW}$ are proportional to Fourier transforms of the $|1s\rangle$ and $|2p\rangle$ atomic functions. Since both $|1s\rangle$ and $|2p\rangle$ are nodeless, the Fourier transform of each will rise with increasing photon (and photoelectron) energy to maxima, then decrease, with the maximum for the $|2p\rangle$ Fourier transform coming at a lower energy than that of the $|1s\rangle$. Since the value of $\langle 1s|\vec{\nabla}|2p\rangle$ is in general large, a cross over energy will exist at which $\langle 1s|\vec{\nabla}|\mathrm{OPW}\rangle = 0$. This spurious zero in σ_{1s} is an inevitable and completely artifical consequence of

attempting to represent the continuum photoelectron state by a basis set of only the two functions $|PW\rangle$ and $|2p\rangle$.

Examination of Fig. 6 shows the phase shifts $\delta_\ell(\varepsilon)$ of the HF continuum functions. The phase shifts $\sigma_\ell(\varepsilon)$ are much smaller than $\delta_\ell(\varepsilon)$ for all but the lowest energies. The εs and εp photoemission channels have large phase shifts with respect to normal Coulomb waves. Thus, for these channels, both Coulomb waves and plane waves ($V(r) = 1/r$ and $V(r)=0$ continuum functions) must differ greatly from the actual continuum functions for small r. Matrix elements calculated with these approximations will be very much in error. However, the εd channel phase shifts are fairly small and the $\ell=2$ part of a plane wave should be a good approximation to the HF and "actual" continuum functions. Comparison of the individual matrix elements for $s \rightarrow p$, $p \rightarrow s$, and $p \rightarrow d$ transitions confirms these expectations (Table 1).

The fair agreement with experiment of the PW and OPW total cross section calculations results from the dominance of the εd channel to the total photoemission cross section. The improvement of the OPW results over the PW results is due to a fortuitous cancellation of εS intensity by the orthogonalization to 1s and 2s states. Since the HF 2p cross section is $\sim 90\%$ d-channel contribution over most of the energy range of Fig. 3, we see that the PW approximation is improved by considering only the $2p \rightarrow \varepsilon d$ PW channel. The marked disagreement between experimental and OPW asymmetry parameters arises because of the poor OPW εs channel approximation and the absence of phase shift information.

It is now possible to generalize the above information to establish the limits within which OPW and PW calculations may be used at

least semi-quantitatively. Consulting Manson's paper[16] on the Z, ℓ, and ε dependence of continuum electron phase shifts calculated in a central-potential model, one notes the excellent agreement between the phase shifts of Fig. 6 and those calculated by Manson for Z = 10. By considering continuum channels with small phase shifts, rough upper limits on Z can be assigned for which plane waves should be fair approximations to the "actual" continuum functions. Only the partial wave corresponding to the $\ell \rightarrow \ell + 1$ final state channel of a photoemission transition are well approximated by plane waves. For a particular angular momentum ℓ continuum function phase shifts become large for Z just great enough to have a bound state with angular momentum ℓ. Calculations for which only the $\ell \rightarrow \ell + 1$ PW channel is considered should yield fair total photoemission cross sections for 1s and 2s shells up to Z = 4, 2p shells up to Z = 12, 3d shells up to Z = 38, and 4f shells up to Z = 88. For slightly higher atomic numbers results should be qualitatively correct, but agreement cannot be expected when Z is almost large enough to support a bound shell with the same symmetry as the continuum channel in question. For initial states with a node in the radial wavefunction, a PW cross section calculation will yield a marked local minimum in the cross section as a function of energy (Fig. 2 and Ref. 17), but assignment of this minimum as a spurious result or a real Cooper minimum requires care.

B. Many-Body (Relaxation) Contributions to Atomic Photoemission Cross Sections

Previous exhaustive and extensive studies of atomic photoemission processes[5] have explicitly considered the effects of intrachannel coupling, core relaxation, interchannel coupling, and electron correlation (see especially the Ph.D. Thesis of R. L. Martin for a discussion of photoemission satellite structure[5]). In these calculations, only single-configuration initial and final states were utilized. Intrachannel coupling was treated implicitly through the use of the Hartree-Fock continuum functions[18] for cases both with and without inclusion of core relaxation. Interchannel coupling was neglected, but has already been shown to be small for neon photoemission.[19]

The inclusion of final-state relaxation in the model for calculating photoemission transitions modifes the HF results in three ways. First, the one-electron transition matrix element is changed because the continuum wavefunction is calculated in the relaxed potential of the ion. Second, because one-electron orbitals of the initial and final states with the same symmetry but different principal quantum numbers are no longer orthogonal, virtual transitions of the type ($1s \rightarrow 2p$, $2p \rightarrow \varepsilon p$) are now allowed. Finally, because equivalent passive orbitals of the initial and final states are not identical, their overlap integrals must be less than unity, which will decrease all the contributions to the total matrix element. The expression for the total cross section, Eq. (2), and the asymmetry parameter, Eq. (4) retain the same form in the case of excitations from closed shells except that the one-electron radial matrix

elements for a transition from a one-electron initial state $n\ell$ to a final continuum state $\varepsilon\ell \pm 1$ are replaced by sums over radial matrix elements of the form

$$R_{n\ell}^{\varepsilon\ell\pm1} = \sum_{k=1}^{N} \det \left\{ \int_0^\infty P'_{\tau(i)}(r) \; \hat{O}_j^k \; P_{\tau(j)}(r)\, dr \right\} , \tag{16}$$

$$\hat{O}_j^k = \begin{cases} 1 \text{ for } j \neq k \\ r \text{ or } \frac{1}{M_e \omega} \left(\frac{d}{dr} + \frac{2\ell_j + 1 \pm 1}{2r} \right) \text{ for } j = k \end{cases} , \tag{17}$$

where N is the total number of electrons of the system and the curly brackets denote an N × N matrix with column index i ($\tau(i) = (n\ell m_\ell m_s)_i$) for the N different final state one-electron orbitals, including the continuum orbital, and row index j, for the N initial state orbitals. The final state radial wavefunctions are primed to emphasize that they are not identical to the corresponding initial state orbitals. The ij^{th} element is zero for $j \neq k$ unless $(\ell m_\ell m_s)_i = (\ell \pm 1\ m_\ell m_s)_j$. Thus the transition matrix element for the HFR (HF with relaxation) case may be quite different from the corresponding one-electron HF matrix element.

The neon 1s photoemission cross sections for the length and velocity approximations differed by less than 1% in both the HF and HFR calculations. At energies above 1200 eV the HFR cross sections agree quite well with experiment (Fig. 2), and are to be preferred over the HF results. However, at lower energies the HF calculation is closer to experiment, except very near threshold (Fig. 1, insert). This is probably due to the neglect of correlation between the slow photoelectron and the

electrons of the remaining ion in our calculations. Right at threshold the virtual processes are quite important, but at higher energies they become small (see Fig. 7). The turning-over of the experimental $\sigma(1s)$ as threshold is approached from above (Fig. 1, insert) arises from such processes, and it is significant that the HFR model reproduces this behavior while HF does not. The phase shifts for the HF and HFR εp continuum functions (Fig. 6) differ by 10% over the whole range of the calculation, showing the fairly large effect of the relaxed potential in determining the continuum wavefunction for an electron excited from a core state.

Relaxation effects are small for neon 2s photoemission, as seen by the small differences in continuum function phase shifts (Fig. 6) and total cross sections (Fig. 2). The HF and HFR cross-section calculations are only distinguishable below 200 eV photon energy, where the HFR velocity approximation is seen to agree most closely with experiment.

Relaxation changes the potential experienced by the photoelectron very little for the 2p photoemission, yet the εd channel phase shifts (Fig. 6) differ significantly for HF and HFR continuum functions at low energy. However, the cross section and asymmetry parameter differences are very small for the two approaches (Figs. 3 and 4). Both the energy and angular dependence of 2p photoemission calculations are in excellent agreement with experiment, with the velocity results being slightly superior.

Slight oscillations[20] occur in the calculated HF and HFR asymmetry parameters above 500 eV which are absent from the OPW calculations. However, these oscillations, which amount to 2% or less of the magnitude

of β, are not entirely consistent among the various HF calculations. Further calculations of β utilizing CI wavefunctions for the initial and final states—and small energy separations between values of $\beta(\varepsilon)$ are required to evaluate whether these oscillations are indeed real or artifacts of the present calculation.

For the cases reported here virtual excitation processes were largely compensated by the change in the one-electron matrix elements due to the relaxed potential. Relaxation is seen to have a very small effect on valence orbital photoemission at all but the lowest photon energies. The one electron picture of photoemission is a quite good approximation for computing cross sections of primary transitions as long as the continuum function used is adequate.

C. Determination of Initial State Properties

Several important considerations have arisen from the calculations presented in the preceding two subchapters. The first is that the quality of the continuum state used to calculate a differential photoemission cross section is of the utmost importance in achieving agreement with experiment. Secondly, the photocurrent emitted by gas phase atomic (and molecular) species displays considerable anisotropy, which is related to interference between two (or more) outgoing ℓ partial-wave channels. Finally, including many electron effects in the cross section calculations modulates the one electron results, but does not drastically alter the character of the computed photocurrent. The use of approximate final state wave functions and the exploitation of the photocurrent

anisotropy to determine initial state properties (geometrical orientation and charge distributions) requires further discussion.

Rabalais and co-workers[21] have calculated photoemission cross sections for neon and several small molecules using PW and OPW continuum functions. They reported results for Ne PW total cross sections that agree closely with the PW results reported here, but they did not list enough OPW cross sections to make comparisons. Molecular photoemission total cross sections calculated by the PW approach for CH_4, NH_3, and H_2O resemble the Ne results closely[21] and can be only slightly better due to the smaller nuclear charges of the central species (it is noted specifically that all these molecular calculations exhibit a local minimum in 2s-like shells similar to that in Fig. 2). Calculations for s-like shells of molecules with more massive atoms such as H_2S are probably not qualitatively correct.

Other workers have also considered molecular photoionization. Hush[22] used an OPW model in which the average potential experienced by the photoelectron is used to give an effective kinetic energy for the continuum electron. This model yields slightly improved total cross sections for small molecules, but will still have the same difficulties as the PW method for large atoms and will be unable to yield angular distributions of photoelectrons.

Ritchie[23] is currently developing procedures to calculate molecular photoemission which explicitly consider the nuclear and electronic potentials. An important consideration of this work is to formulate general procedures for converting observed differential photocurrents into maps of the initial state wave functions (charge distributions). Chapman and

Hayes[24] have developed methods for computing photocurrents using continuum state expansions about the molecular center of mass. Pseudopotential models have also been considered[25] and have yielded very promisng results for molecular photoemission. Using an X-α scattered wave approach, Dehmer and Dill found strong interchannel coupling effects[26] at low energies which are strictly molecular phenomena and require accurate wavefunctions to handle correctly. These "shape resonances" may be considered to arise from scattering of photoelectrons between atomic centers of a molecule. Davenport[27] has used such a formulation to compute photocurrents from oriented CO and N_2 molecules, which have been used extensively in photoemission studies of adsorbates.[28]

Gadzuk[4] and Liebsch[4] have considered photoemission from adsorbates on oriented surfaces in PW approximations. Their work has concentrated on obtaining angular distributions of photoelectrons from the adsorbate-surface system. Although the angular dependence of photoemission for a given ℓ channel of an adsorbed species and surface geometry may be correctly determined, the plane wave treatment is incapable of treating interference between different allowed ℓ channels.

The information content of valence band differential cross sections of solids (especially single crystals) and adsorbate systems is potentially very great. Since crystalline axes and adsorbed molecule orientations are fixed in space, the anisotropies in photocurrents should be much more pronounced than in the gas phase, where an average over all orientations must be considered. Indeed, as mentioned above, the orientation of CO on several transition metal surfaces has been studied by

several groups[28] who compared experimentally determined photoemission intensities with Davenport's calculations.[27] A proper understanding of photoemission data should also yield the nature of the bonding at surfaces and in solids through the determination of the electronic wave-functions of the systems studied. However, before this understanding can be achieved, the nature of uniquely solid state photoemission phenomena must be studied. The remainder of this thesis will focus on solid state photoemission. Perhaps it should be mentioned here that photoemission from solid surfaces and adsorbate systems is far from being completely explained, but the promise of determining not only energy levels but also initial state wave functions from photoemission measurements is rapidly being fulfilled.

REFERENCES

*This chapter appeared in part as "Comparison of Final State Approximations in the Calculation of Total and Differential Cross Sections of Neon," R. S. Williams and D. A. Shirley, J. Chem. Phys. 66, 2378 (1977).

1. U. Fano and J. W. Cooper, Rev. Mod. Phys. 40, 441 (1968); J. Cooper and R. N. Zare, Lectures in Theoretical Physics, Vol. 11c, edited by S. Geltman, K. Mahanthappa, and W. Brittin (Gordon and Breach, New York, 1969), pp. 317-337.
2. B. Ritchie, J. Chem. Phys. 60, 898 (1974); B. Schneider and R. S. Berry, Phys. Rev. 182, 141 (1969).
3. B. Feuerbacher and R. F. Willis, J. Phys. C9, 169 (1976); G. D. Mahan, Phys. Rev. B 2, 4334 (1970).
4. F. O. Ellison, J. Chem. Phys. 61, 507 (1974); J. W. Gadzuk, Phys. Rev. B 12, 5030 (1974); A. Liebsch, Phys. Rev. B 13, 544 (1976).
5. Ne differential photoemission cross sections have been calculated by many authors using different approaches. R. J. W. Henry and L. Lipskey, Phys. Rev. 153, 51 (1967); M. Y. Amusia, N. A. Cherepkov, and L. V. Chernysheva, Sov. Phys.-JETP 33, (1971); D. J. Kennedy and S. T. Manson, Phys. Rev. A 5, 227 (1972); F. M. Chapman and L. L. Lohr, Jr., J. Amer. Chem. Soc. 96, 4731 (1974); P. G. Burke and K. T. Taylor, J. Phys. B 8, 2620 (1975); R. L. Martin and D. A. Shirley, Phys. Rev. A 13, 1475 (1976), R. M. Martin, Ph.D. Thesis, University of California Lawrence Berkeley Laboratory Report, LBL-5167 (1976) unpublished.

6. J. W. Cooper and S. T. Manson, Phys. Rev. 177, 157 (1969).

7. R. A. Buckingham, Quantum Theory I. Elements, edited by D. R. Bates (Academic Press, New York, 1961), p. 147

8. See especially the second reference of footnote 1.

9. A. R. Edmonds, Angular Momentum in Quantum Mechanics, (Princeton University Press, Princeton), 1960, p. 80.

10. L. L. Lohr, Jr., Electron Spectroscopy, edited by D. A. Shirley, (North-Holland, Amsterdam, 1972), p. 245.

11. For further discussion see the third reference of footnote 5.

12. G. N. Bates, Computer Phys. Commun. 8, 220 (1974).

13. M. J. Seaton and G. Peach, Proc. Phys. Soc. (London) 79, 1296 (1962).

14. P. S. Bagus, Phys. Rev. 139, A619 (1965).

15. H. A. Bethe and E. E. Salpeter, Quantum Mechanics of One- and Two-Electron Atoms, (Springer-Verlag, Berlin, 1957), pp. 295-320.

16. S. T. Manson, Phys. Rev. 182, 97 (1969).

17. P. S. Wehner, J. Stöhr, G. Apai, F. R. McFeely, R. S. Williams, and D. A. Shirley, Phys. Rev. B 14, 2411 (1976).

18. See section 5 of the first reference of footnote 1.

19. See the first reference of footnote 5.

20. Oscillations of this type in calculations of β have also been observed by C. Fadley (private communication).

21. J. W. Rabalais, T. P. Debies, J. L. Berkosky, J.-T. J. Huang, and F. O. Ellison, J. Chem. Phys. 61, 516 (1974); J. W. Rabalais, T. P. Debies, J. L. Berkosky, J.-T. J. Huang, and F. O. Ellison,

J. Chem. Phys. 61, 529 (1974); J. W. Rabalais and T. P. Debies, J. Electron Spectrosc. 5, 847 (1974).

22. P. R. Hilton, S. Nordholm, and N. S. Hush, Chem. Phys. 15, 345 (1976).

23. B. Ritchie, J. Chem. Phys. 60, 898 (1974); B. Ritchie, J. Chem. Phys. 61, 3279 (1974); B. Ritchie, J. Chem. Phys. 63, 1351 (1975).

24. F. M. Chapman, Jr. and E. F. Hayes, J. Chem. Phys. 67, 2974 (1977).

25. B. Schneider and R. S. Berry, Phys. Rev. 182, 141 (1969).

26. J. L. Dehmer and D. Dill, J. Chem. Phys. 65, 5327 (1976).

27. J. W. Davenport, Phys. Rev. Lett. 36, 945 (1976).

28. R. J. Smith, J. Anderson, and G. J. Lapeyre, Phys. Rev. Letts. 37, 1081 (1976); G. Apai, P. S. Wehner, R. S. Williams, J. Stöhr, and D. A. Shirley; Phys. Rev. Letts. 37, 1497 (1976); C. L. Allyn, T. Gustafeson, and E. W. Plummer, Chem. Phys. Lett. 47, 127 (1977).

29. A. Liebsch, Electron and Ion Spectroscopy of Solids, edited by W. Dekyser, J. Vennik, and L. Fiermans (Plenum, New York) to be published; S. Y. Tong and C. H. Li, Bull. Am. Phys. Soc. 23, 417 (1978).

30. F. Wuilleumier, Adv. X-ray Anal. 16, 63 (1973).

31. J. A. R. Samson, J. Opt. Soc. Am. 55, 935 (1965).

Table I.[a]

Photon Energy	2s → εp		2p → εs		2p → εd	
	HF	PW	HF	PW	HF	PW
50	.205	-.074	-.199	.441	-.445	-.342
100	.332	-.447	-.154	.484	-.437	-.375
200	.329	-.121	-.110	.388	-.307	-.301
300	.293	-.036	-.086	.309	-.216	-.239
400	.260	-.110	-.070	.251	-.161	-.195
500	.233	-.147	-.059	.210	-.126	-.162
1000	.153	-.171	-.031	.105	-.055	-.081
1500	.114	-.147	-.020	.065	-.022	-.035
2000	.091	-.125	-.0.14	.045	-.022	-.035

[a] Numerical values of the matrix element $\langle f|\frac{d}{dz}|i\rangle$ for initial states (i) 2s and 2p and for some HF and PW final states (f). Note that the plane wave matrix elements for the 2s → εp and 2p → εs transitions have the opposite sign of the corresponding HF matrix elements.

FIGURE CAPTIONS

Fig. 1. Calculated neon 1s photoionization cross sections versus photon energy compared with the experimental values of Wuilleumier (W) in Ref. 30. For the Hartree-Fock continuum function calculations the dipole length and velocity approximations yield results indistinguishable on the scale presented here.

Fig. 2. Calculated neon 2s photoionization cross sections versus photon energy. The experimental values (W) are from Ref. 30. Dipole length and velocity approximations are denoted by L and V respectively.

Fig. 3. Calculated neon 2p photoionization cross sections versus photon energy. The experimental values are (W) from Ref. 30 and (S) from Ref. 31.

Fig. 4. The asymmetry parameter β for neon 2p photoionization as a function of photon energy. The experimental values (W) are from Ref. 30.

Fig. 5. Comparison of the radial part of the HF εp wave ejected from Ne 1s by an 1100 eV photon with the p component of a plane wave with identical kinetic energy. The continuum functions in this figure are not normalized.

Fig. 6. The phase shift $\delta(\varepsilon,\ell)$ with respect to a normal Coulomb wave for Hartree-Fock continuum functions calculated in unrelaxed and relaxed (R) final state atomic potentials versus continuum electron kinetic energy.

Fig. 7. Percent contribution to the total n electron transition matrix element due to the various virtual processes allowed when relaxation is considered in the Ne 1s photoionization.

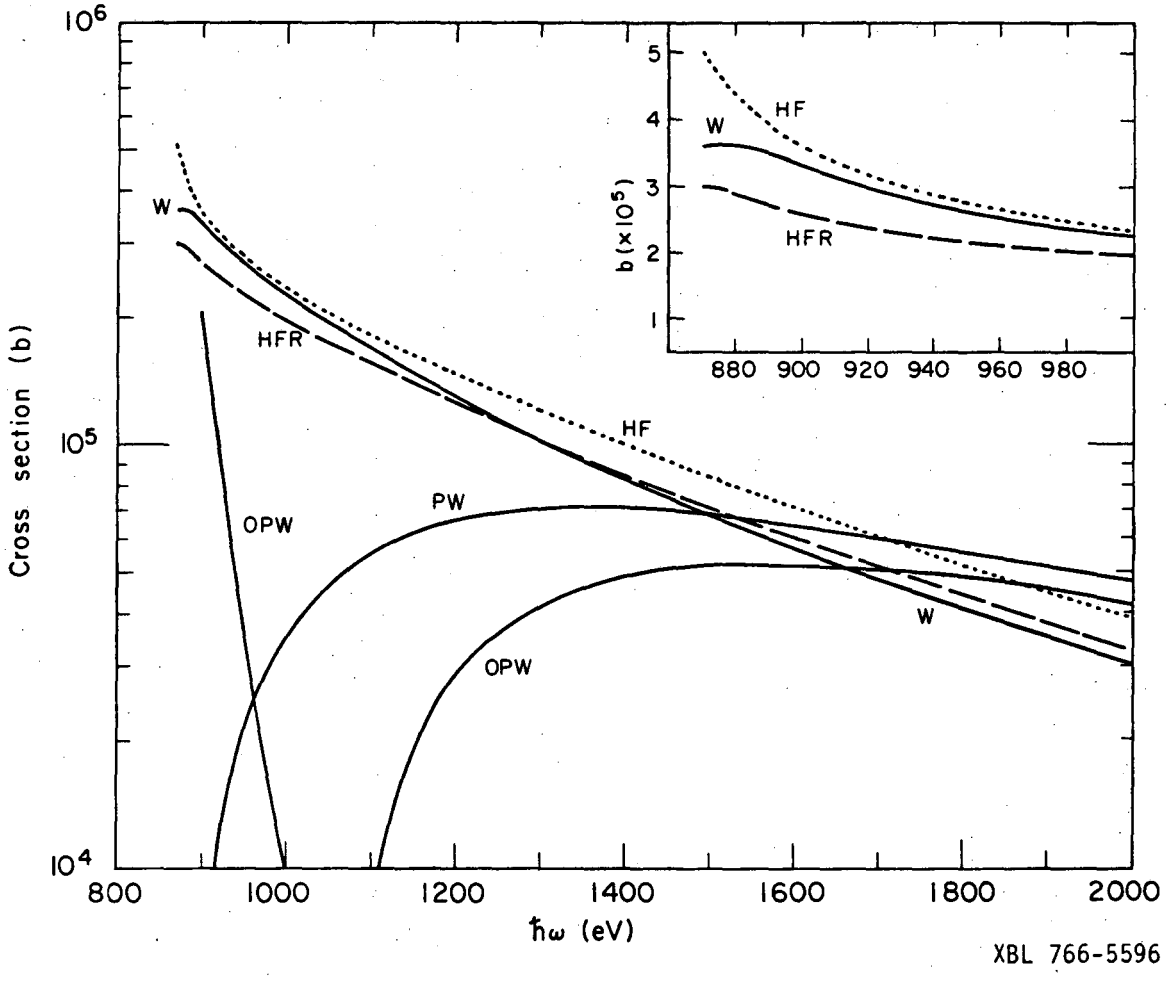
Cross section (b)
10^6
10^5
10^4
800
1000
1200
1400
1600
1800
2000
$\hbar\omega$ (eV)
W
HFR
HF
OPW
PW
OPW
W
b (x 10^5)
5
4
3
2
1
880
900
920
940
960
980
HF
W
HFR
XBL 766-5596

Fig. 1

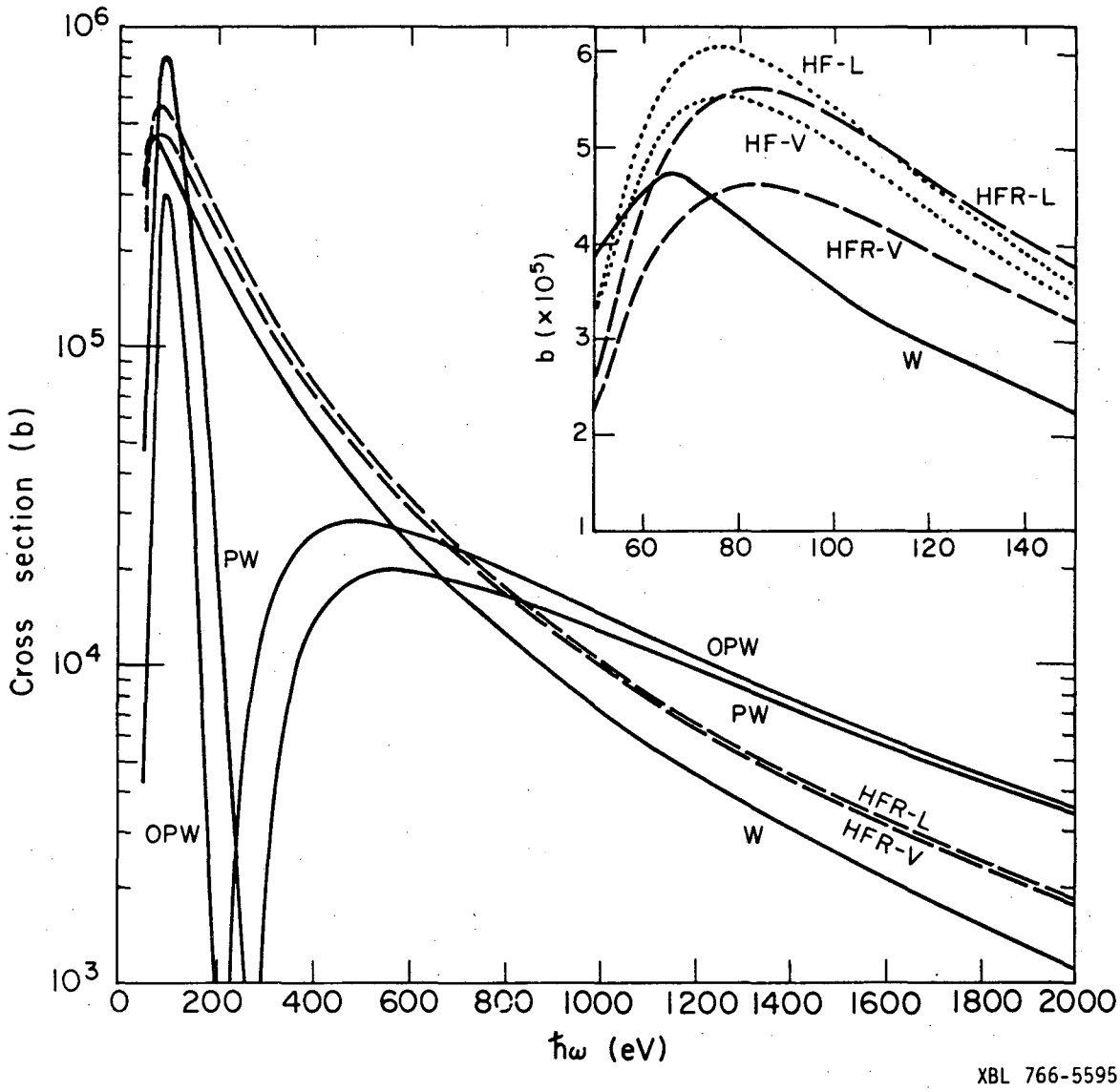
Cross section (b)
10^6
10^5
10^4
10^3
0
200
400
600
800
1000
1200
1400
1600
1800
2000
$\hbar\omega$ (eV)
PW
OPW
OPW
PW
HFR-L
HFR-V
W
b (x 10^5)
1
2
3
4
5
6
60
80
100
120
140
HF-L
HF-V
HFR-L
HFR-V
W
XBL 766-5595

Fig. 2

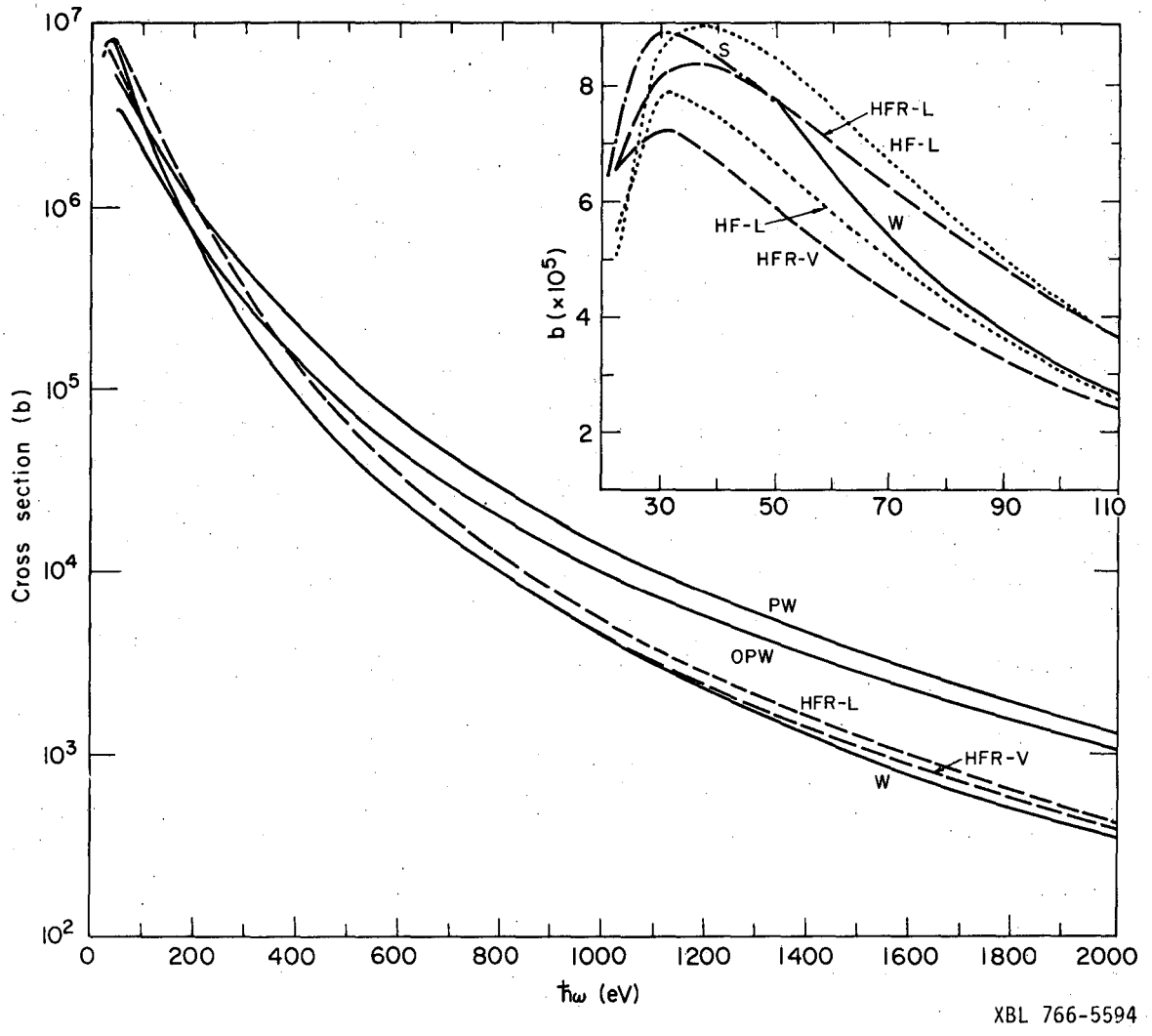
Cross section (b)
10^7
10^6
10^5
10^4
10^3
10^2
0
200
400
600
800
1000
1200
1400
1600
1800
2000
$\hbar\omega$ (eV)
PW
OPW
HFR-L
HFR-V
W
b ($\times 10^5$)
8
6
4
2
30
50
70
90
110
S
HFR-L
HF-L
W
HF-L
HFR-V
XBL 766-5594

Fig. 3

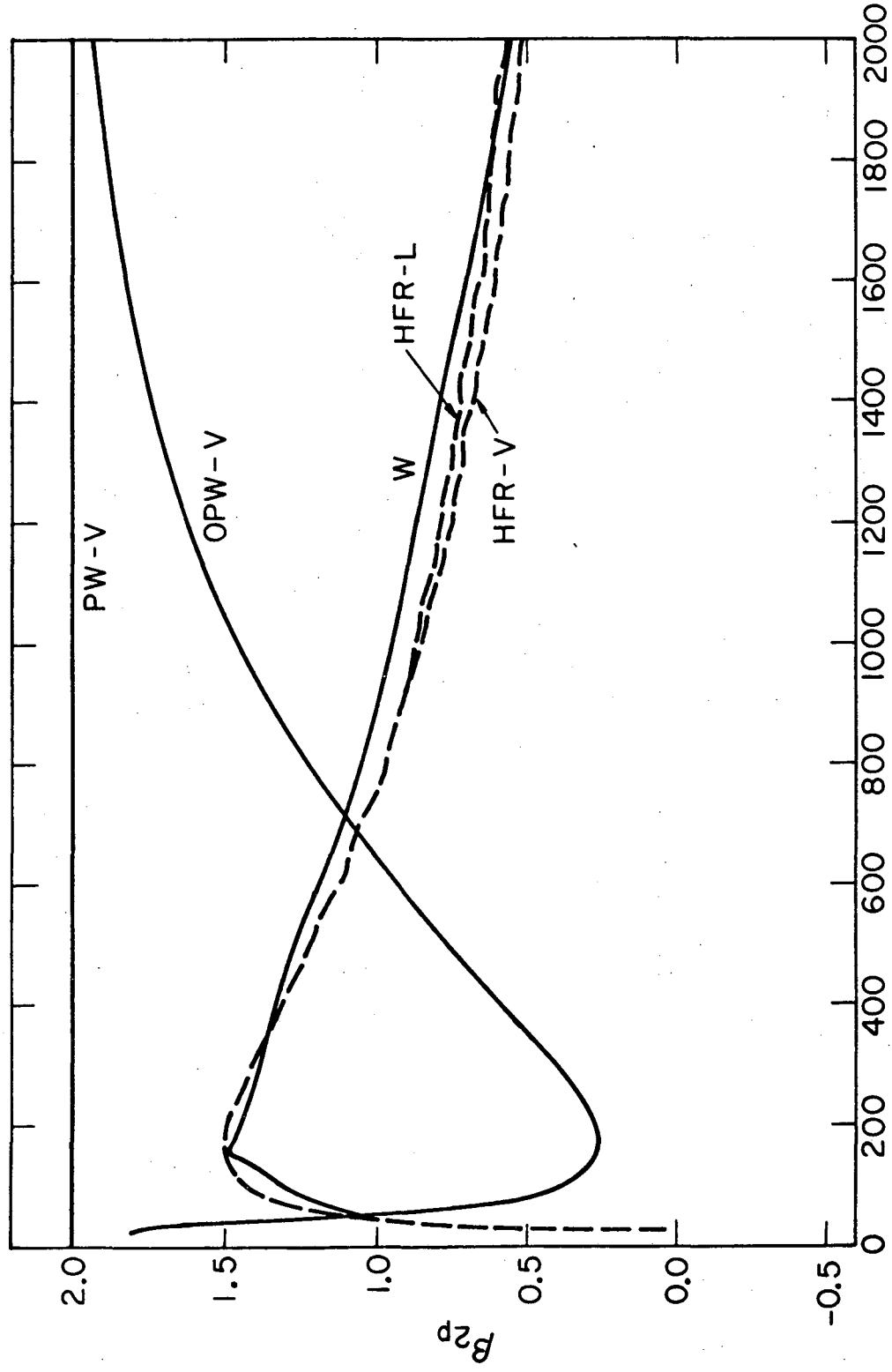

XBL766-5598

Fig. 4

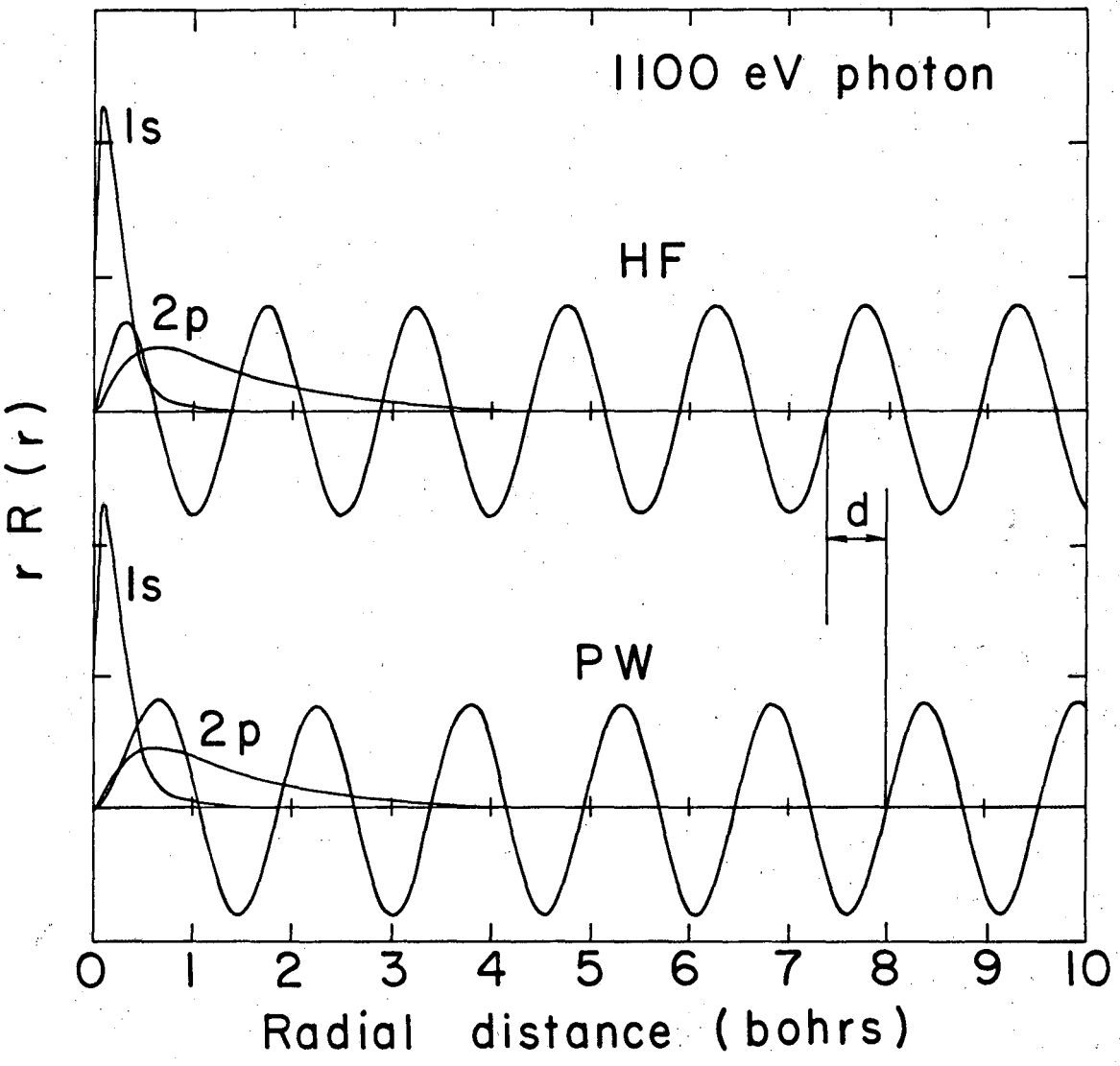

XBL7510-8621

Fig. 5

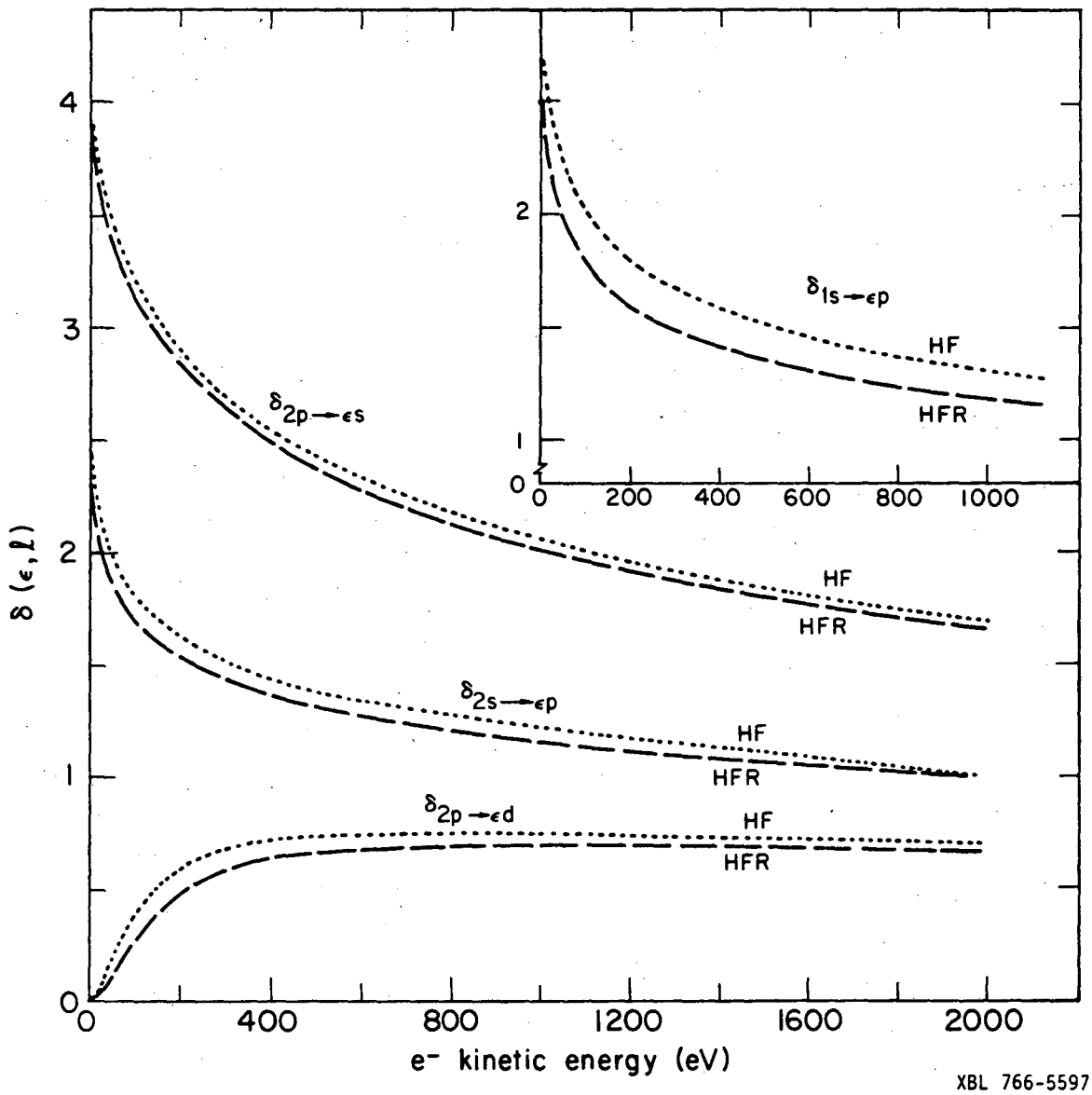
δ (ε, ℓ)
e⁻ kinetic energy (eV)
δ2p→εs
HF
HFR
δ2s→εp
HF
HFR
δ2p→εd
HF
HFR
δ1s→εp
HF
HFR
0
400
800
1200
1600
2000
0
200
400
600
800
1000
XBL 766-5597

Fig. 6

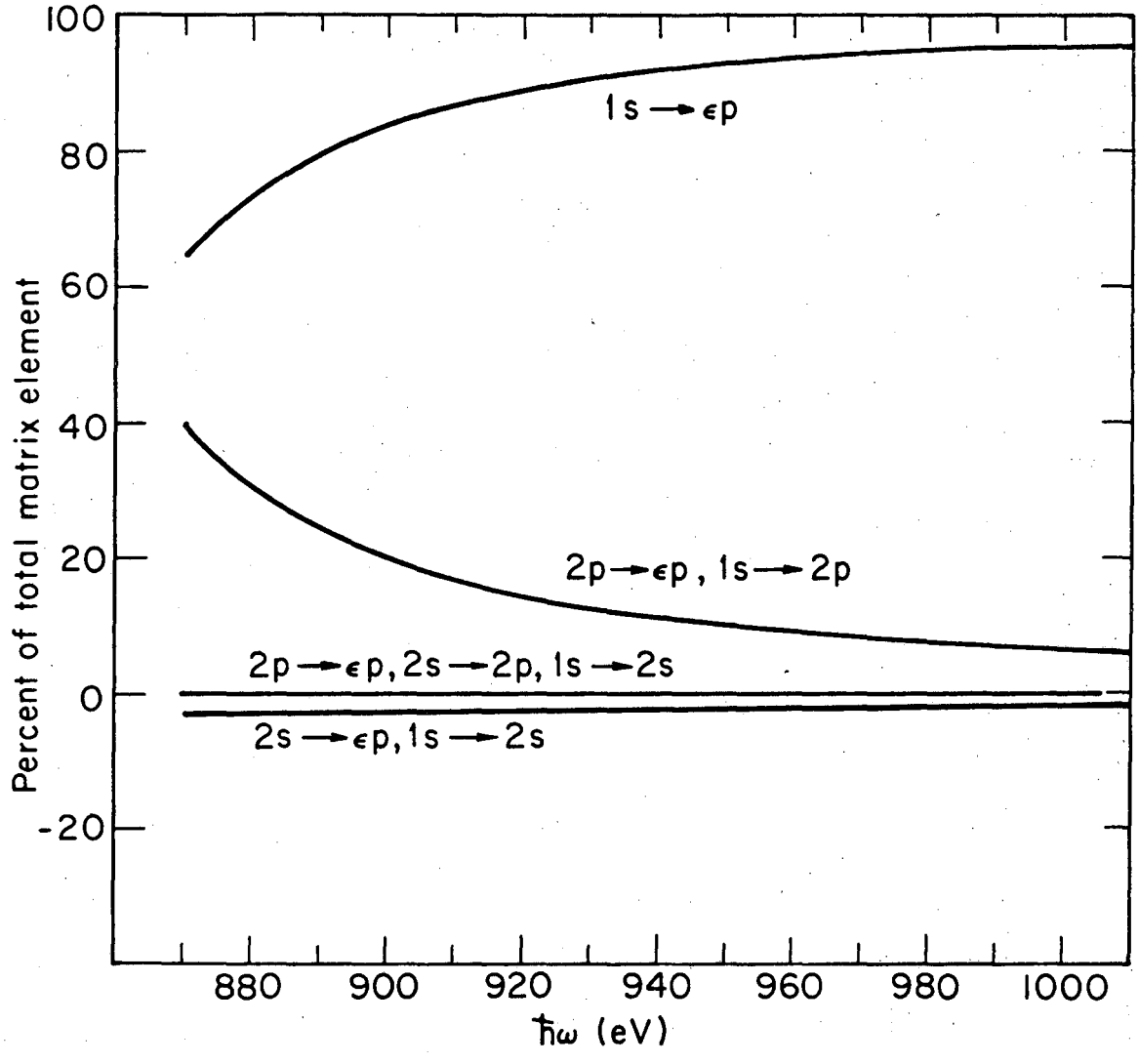
100
80
60
40
20
0
-20
Percent of total matrix element
1s → εp
2p → εp , 1s → 2p
2p → εp, 2s → 2p, 1s → 2s
2s → εp, 1s → 2s
880
900
920
940
960
980
1000
ħω (eV)
XBL766-5599

Fig. 7

III. ANGLE RESOLVED PHOTOEMISSION FROM SOLIDS

In discussing ARPES from solids, one must first define the angle of interest. Solid state PES spectra are functions of the photoelectron emission angles with respect to bulk crystalline axes and the sample surface. They are also dependent on the angle between the incident photon direction and the photoelectron momentum vector, the sample surface (and whether the radiation is unpolarized or s- or p-polarized), and the crystalline axes. Most frequently, ARPES is used to denote momentum resolution of photoelectrons - ie. the angle of photoelectron emission with respect to the crystalline axes - and this is the usage intended for the purposes of this chapter. The effects of the other angles on solid state ARPES spectra will be discussed in varying detail later.

The selection of the final state momentum of a photoelectron as well as the energy locates the final state rather precisely in the extended zone scheme. Due to the direct or vertical nature of the photoexcitation process, the initial state of the photoelectron can be determined knowing only the excitation energy and the reciprocal lattice vector involved in the electronic transition. Thus, an experimental determination of the initial state band structure of a crystalline solid should be possible using ARPES.

Copper has been the subject of numerous angle-integrated[1-3] and angle-resolved[2,4-8] photoemission (ARPES) studies. Because of its accurately known band structure,[9,10] it has served as a model system for the theoretical interpretation of the details of the photoemission

process.[1,8,10] Following the early work of Smith,[11] it is now generally accepted that bulk photoemission from polycrystalline and single crystal Cu surfaces is adequately described by direct (momentum conserving) transitions in the three step model.[12] At photon energies which allow the entire valence band (VB) region to be studied ($\geqslant$ 10 eV) calculation of the excitation step is usually sufficient to explain the energy positions of the dominant experimental features.[8,10,11]

Although direct transition theory accounts quite well for low photon energy photoemission from polycrystalline Cu samples, the interpretation of ARPES spectra was somewhat clouded by the existance of different models for the inclusion of the additional constraint of momentum resolution which were consistent with the angle integrated studies. Most of the difficulty encountered when constructing a model of angle-resolved photoemission involved the directional nature of the final state bands in the crystal[12] and the extent to which the surface and photocurrent damping effects altered conservation rules.[13] A popular construct was the one dimensional density of states model (ODDOS),[14] which hypothesized the breakdown of the crystal momentum conservation condition normal to the crystal surface due to the termination of the bulk periodicity at the interface and the existance of a finite inelastic mean free path for the photoelectron. However, a much simpler direct transition model,[8] which ignores the surface altogether, has been shown to yield excellent agreement with experimental energy distribution curves (EDC's) collected in ARPES studies of Cu single crystals. In this chapter, studies are presented which relate directly to the nature of crystal momentum conservation conditions,

the high energy conduction bands, and the selection rules governing photoemission transitions within the framework of this simplified model.

A. Experimental

The data presented here were collected using the variable photon energy sources available at the 4°[16] and 8°[17] ports of Beam Line I at the Stanford Synchrotron Radiation Laboratory (SSRL).[18] Copper single crystals were cut with surface orientations paralleling the (100), (110), (111) and (211) planes, with the orientations and quality of the surfaces checked by taking Laue back-reflection photographs and in some cases LEED spectra. After polishing and etching of the surfaces, the crystals were installed in the photoemission chamber. Final cleaning of the crystal surfaces was accomplished by argon ion bombardment, followed by annealing to high temperatures (~ 800°C) to remove surface defects. The cleanliness of the sample surfaces could then be monitored in situ by Auger or photoemission spectroscopy. Further specific details of the facilities, cleaning procedures, and geometries used for these experiments are considered individually.[2,7,15,19]

B. Normal Emission Geometry and Band Mapping

In Fig. 1 are shown a series of ARPES spectra collected normal to the (111) face of a Cu single crystal. The spectra were obtained using the 7-35 eV photon energies available from the 8° beam port at SSRL. The large variations in the spectra as a function of photon energy are immediately obvious. Since all these spectra have the same

component of surface parallel crystal momentum ($k_{||} = 0$), the ODDOS model would predict only minor spectral changes with photon energy and so is obviously not applicable to Cu ARPES in this photon energy regime.

The band structure of Cu extending 25 eV above the Fermi level is presented in Fig. 2 in order to reconsider the direct transition model in more detail. The final state band (band 7) along the Γ-L direction of momentum space (ie. momentum along the [111] axis of real space) appears to be very free electron-like from 7-25 eV above the Fermi level. This band is nominally the final state to which the photoelectrons are excited in Fig. 1.

In the three step model of photoemission,[20] photoexcitation of an electron to a final state above the vacuum level, transport of the photoelectron to the surface, and escape of the hot electron across the solid-vacuum interface are considered separately. A simple model may then be constructed for angular dependent photoemission, which was first treated in detail by Mahan[21] for free electron-like metals, by considering the Fermi's Golden Rule formula

$$J(E_f,\vec{k}_f,h\nu) \propto \sum_{\vec{k}_i}^{\vec{k}_i \subset BZ} \sum_{E_j(\vec{k}_i)}^{E_j < E_F} |\langle E_f,\vec{k}_f|\vec{A}\cdot\vec{P}|E_j,\vec{k}_i\rangle|^2$$

$$\times \delta[E_F - E_j - h\nu] \qquad (1)$$

for the photocurrent J inside an infinite crystal as a function of the photon energy and the photoelectron energy and crystal momentum. The

summations are over all initial momentum states $\vec{R}_i$ in the first Brillouin Zone (BZ) and all the occupied energy levels $E_j < E_F$. The $\vec{A}\cdot\vec{P}$ term is the usual interaction Hamiltonian between a time varying electromagnetic field and an electron eigenstate, where the spatial part of $\vec{A}$ is proportional to $\vec{\varepsilon}\exp(i\vec{k}_{h\nu}\cdot\vec{r})$ with $\vec{\varepsilon}$ and $\vec{k}_{h\nu}$ the polarization and wavevector of the photon field, respectively (the wavevector will be taken as real since the attenuation of the electromagnetic field in a solid is negligible with respect to electron mean free paths). The $\vec{p}\cdot\vec{A}$ term cannot rigorously be set equivalent to zero by any Gauge transformation due to the anisotropy of the electric field across the vacuum-solid interface, but will be neglected anyway. The delta function expresses the necessary conservation of energy condition.

For the final state a single plane wave $|E_f,\vec{k}_f\rangle = \exp(i\vec{k}_f\cdot\vec{r})$ is chosen, where $\vec{k}_f$ denotes the photoelectron <u>propagation direction</u> as well as the wavelength inside an infinite crystal. The mechanics of how this final state is detected will be ignored for the present. The initial state wave function must in general satisfy the Bloch condition

$$|E_j,\vec{k}_i\rangle = \sum_{\vec{R}} e^{i\vec{k}_i\cdot\vec{R}}\ \phi_j(\vec{r}-\vec{R}) \qquad (2)$$

where the ϕ_j's are atomic or Wannier functions and the $\vec{R}$'s are all the lattice vectors of the infinite solid. Using the above wave functions to evaluate the matrix element in Eq. (1) yields the result:[22]

$$|\langle E_f,\vec{k}_f|\vec{A}\cdot\vec{p}|E_j,\vec{k}_i\rangle|^2 = \cos^2\gamma\ \Phi_j^2(\vec{k}_f)\,\Big|\sum_{\vec{R}} \exp[i(\vec{k}_f-\vec{k}_i-\vec{k}_{h\nu})\cdot\vec{R}]\Big|^2 \quad . \qquad (3)$$

Here γ is the angle between $\vec{\varepsilon}$ and $\vec{R}_f$, $\Phi_j(\vec{k}_f)$ is the Fourier transform of $\phi_j(\vec{r})$ evaluated for $\vec{k}_f$, and the term

$$\Big|\sum_{\vec{R}} \exp[i(\vec{k}_f - \vec{k}_i - \vec{k}_{h\nu})\cdot\vec{R}]\Big|^2 \quad \text{is zero}$$

unless $(\vec{k}_f - \vec{k}_i - \vec{k}_{h\nu})\cdot\vec{R}$ is some multiple of 2π, in which case the sum becomes infinite. Thus, in order for a transition to be allowed, $\vec{k}_f - \vec{k}_i - \vec{k}_{h\nu}$ must be a reciprocal lattice vector $\vec{G}$ of the crystal. The final form of the squared transition matrix element in this approximation is

$$|\langle E_f,\vec{k}_f|\vec{A}\cdot\vec{p}|E_j,\vec{k}_i\rangle|^2 \propto \cos^2\gamma\ \Phi_j^2(\vec{k}_f)\,\delta(\vec{k}_f - \vec{k}_i - \vec{k}_{h\nu} - \vec{G}) \quad . \qquad (4)$$

For photon energies below ~ 200 eV the momentum $\vec{k}_{h\nu}$ is completely negligible; the delta function (or crystal momentum selection rule) then is the so called direct or vertical transition requirement. It is a consequence of the assumptions that the initial state is a Bloch sum and that the crystal is infinite in extent.

The energy and crystal momentum conservation requirements for a photoemission transition are illustrated by rigidly shifting the final state band of a band structure vertically downward by an amount equal to

the photon energy. A transition is allowed whenever the final and initial state bands cross, and should manifest itself as a peak in an ARPES spectrum. Conversely, by assuming a nearly free electron-like final state as shown in Fig. 2, it should be possible to assign peaks in ARPES spectra of single crystals to initial state bands and thus map out the band structure of the material studied. Such a comparison is shown in Fig. 3, where the agreement between Burdick's band structure and the experimentally determined bulk band positions is excellent.

ARPES spectra have also been collected in a normal emission geometry from the Cu(111), (110), and (100) faces for photon energies ranging from 32 eV to 160 eV. The validity of a nearly free electron-like final state band approach in this energy regime has been questioned[13] due to the increase in the density and crossing frequency of bands populated at these higher photon energies. However, a single empty lattice band and the spectra collected at these energies (Fig. 4) yields experimental band structures in excellent agreement with Burdick's calculations, as seen in Fig. 5. Thus, perhaps surprisingly, the validity of the single band final state approximation and the vertical transition requirement holds quite well for Cu photoemission using photon energies from 7 to 160 eV.

This observation may be used to analyze the nature of the final state bands themselves. The unbound electron states may be conveniently expressed in a plane wave basis as

$$|E_f,\vec{k}_f\rangle = \sum_{\vec{G}} a_{\vec{G}} \exp[i(\vec{k}_f + \vec{G}) \cdot \vec{r}], \quad \text{where}$$

the summation is over all $\vec{G}$ vectors (including $|\vec{G}| = 0$), and $\vec{k}_f$ is the nominal single plane wave momentum of the state considered in the extended zone scheme. However, the actual final state band must have nearly the same directional characteristics for electron propagation in the solid as the free electron band already considered. The apparent validity of this model in accounting for photoemission peak positions implies $a_{(0,0,0)} > a_{\vec{G}\neq(0,0,0)}$. This observation is further supported by the observation that none of the Cu spectra presented show clear evidence for photopeaks arising from G vectors other than (0,0,0) (termed secondary Mahan cone emission[21]). However, a single plane wave final state is not expected to yield accurate cross section information. This may be seen by writing the transition matrix element for the actual final state[23]

$$|\langle E_f,\vec{k}_f|\vec{A}\cdot\vec{p}|E_i,\vec{k}_i\rangle|^2 \propto \left|\sum_{\vec{G}} a_{\vec{G}}\cos\gamma_{\vec{G}}\,\Phi_j(\vec{k}_f+\vec{G})\;\delta(\vec{k}_f-\vec{k}_i-\vec{G})\right|^2 \qquad (5)$$

where γ_G is the angle between $\vec{k}_f + \vec{G}$ and the polarization vector of the radiation field $\vec{\varepsilon}$. It is seen from this expansion that the $\cos\gamma_{\vec{G}}\,\Phi_j(\vec{k}_f+\vec{G})$ term in the summation may act to offset the small $a_{\vec{G}}$ term for $\vec{G} \neq (0,0,0)$ and modify the value of the transition probability considerably from a single plane wave form. In fact single plane wave final states do yield rather poor results in calculating relative peak intensities in ARPES spectra,[8] and the number and quality of terms that must be retained in the expansion of the final state is uncertain. Perhaps methods using atomic continuum functions that couple to the

high energy bands of the crystal would yield valid results more readily[24] than a plane wave expansion.

C. Polarization Selection Rules

In addition to the conservation conditions there exist uniquely solid state selection rules in ARPES that deal with final states observed along symmetry directions and the vector nature of the exciting radiation. From a group theoretical point of view, the final state in solid state photoemission must be compatible with the symmetry of the outer product of the initial state and the transition operator.[25] Since an ARPES experiment chooses a particular final state (which has particular symmetry properties), the initial states that may be sampled are determined by the orientation of the radiation polarization with respect to the crystalline axes of the sample.[26]

Again considering photoemission in an infinite solid lattice (ignoring how the radiation got there) the transition matrix element has been expressed as $\langle E_f,\vec{k}_f|\vec{A}\cdot\vec{p}|E_i,\vec{k}_j\rangle$. To determine the polarization selection rules for photoemission from fcc crystals, the character tables of Slater are helpful.[25] The procedure is to form the outer product of the irreducible representations of the vector components ε_x, ε_y, and ε_z (ie., the projections of the polarization vector onto the crystalline coordinate axes) with the irreducible representation of the final state $|E_f,\vec{k}_f\rangle$ (which belongs to the identity element for the group of symmetry operations about the axis of emission). This product is simply the irreducible representation of the component of the vector potential considered, which must also be the symmetry of the

initial states allowed in the photoemission transition. Table 1 contains the photon polarization selection rules governing photoemission transitions into the [001], [011], [111] and [211] directions of an fcc crystal. These rules are only rigorous along the emission directions specified, but they should be generally applicable for ARPES spectra with good angular resolution.

Thus it is seen that by properly orienting the radiation polarization along the crystalline axes, it is possible to select (and thus identify) initial states according to their symmetry classification. Figure 6 shows spectra collected normal to a (211) crystal face for two different photon polarizations, as shown in the insets. The differences in photoemission peak intensities for spectra collected with the same photon energy but different polarizations (except at 14 and 16 eV photon energies, to be discussed in chapter V), are quite well correlated to the selection rules presented in Table 1. Figure 7 presents the occupied bands of copper for the [211] direction in momentum space compared to ARPES peak positions for the two symmetry orientations in which the spectra were collected.

D. A Note of Caution

The crucial revelation that yielded band structure information from ARPES data was that the final state bands in a solid do contain directional information. Although Mahan's[21] definitive work on photoemission appeared in 1970, several later implementations of ARPES spectra calculation schemes obscured the relatively simple relation between ARPES spectra and band structure. A case in point is

provided by the work of Christensen and Feuerbacher,[12] (CF) where the "direct transition" model employed by these authors differs from the one presented above. In the CF model, any final band state that appears on the momentum axis of the BZ that points into the electron detector and conserves energy is an allowed photoemission final state. In the spirit of angle integrated UPS spectral calculations,[11] the ARPES spectrum is generated by computing the energy conserving product of the initial and final density of states that lie on a particular symmetry axis of the BZ. The spectra calculated by the CF model contain "secondary Mahan cone" intensity from bands that lie on the symmetry axis weighted equally to the primary emission. This model yields the same results as the single band direct transition for low electron kinetic energies, since only one band is present in the band structure. However, at energies high enough above the vacuum level that additional $\vec{G}$ vectors begin to contribute states to the band structure, the CF model becomes invalid.

For ARPES spectra from W single crystal faces the CF model achieved reasonable agreement to the experimental measurements at low photon energies.[12] However, Heiman, et al.[27] (HNR) applied the same model to calculate photoemission spectra normal to a Cu(110) surface for 16.8 and 21.2 eV photon energies. There are two energy conserving bands along the Γ-K-X symmetry axis of the band structure for $h\nu$ = 16.8 eV and three for $h\nu$ = 21.2 eV. When the calculated spectra did not agree with their measurements but their experimental spectra were very similar, HNR concluded that the direct transition model had broken down for photoemission from the Cu(110) face. In fact, their spectra are

in excellent agreement with the single band direct transition model,[15] as are the spectra collected in the 32-160 eV photon energy range presented in Fig. 4. The results of HNR do show that secondary Mahan cone emission in their spectra is unimportant, since strong peaks due to secondary cones in their calculation do not appear in the experimental spectra.

This section is intended as a precautionary note. The photoemission literature contains a great many excellent papers dealing with the different aspects of ARPES from valence bands. However, there are many different models that bear the name "direct transition theory," and care should be taken to ascertain the physical assumptions used in a model and then classify it according to taste rather than gather a possibly incorrect notion regarding the contents of a paper from its title or abstract.

In this regard, comparing calculated spectra to experiment to test the hypotheses of a model rather than selecting specific features (ie. peak positions) to compare can be deceiving due to the great deal of uncertainty that still exists about solid state photoemission. In the remainder of this theis, trends observed in experimental ARPES spectra will be discussed in terms of the available theory without attempting to synthesize the spectra themselves.

REFERENCES

1. For a review in the range $h\nu < 25$ eV see D. E. Eastman in Vacuum Ultraviolet Radiation Physics, edited by E. E. Koch, R. Haensel, and C. Kunz (Pergamon, Vieweg, 1974), p. 417.
2. For a review in the range 30 eV $\leqslant h\nu \leqslant$ 200 eV see D. A. Shirley, J. Stöhr, P. S. Wehner, R. S. Williams, and G. Apai, Physica Scripta 16, 398 (1977).
3. J. Stöhr, F. R. McFeely, G. Apai, P. S. Wehner, and D. A. Shirley, Phys. Rev. B14, 4431 (1975).
4. W. Gerhardt and E. Dietz, Phys. Rev. Lett. 26, 1477 (1971).
5. H. Becker, E. Dietz, N. Gerhardt, and H. Angermüller, Phys. Rev. B12, 2084 (1975).
6. L. Ilver and P. O. Nilsson, Solid State Commun. 18, 677 (1976).
7. J. Stöhr, G. Apai, P. S. Wehner, F. R. McFeely, R. S. Williams, and D. A. Shirley, Phys. Rev. 14, 5144 (1976).
8. L. F. Wagner, Z. Hussain, and C. S. Fadley, Solid State Commun. 21, 257 (1977).
9. G. A. Burdick, Phys. Rev. 129, 138 (1963).
10. J. F. Janak, A. R. Williams, and V. L. Moruzzi, Phys. Rev. B11, 1522 (1975).
11. N. V. Smith, Phys. Rev. Lett. 23, 1452 (1969); Phys. Rev. B3, 1862 (1971).
12. B. Feuerbacher and N. E. Christensen, Phys. Rev. B10, 2373 (1974); N. E. Christensen and B. Feuerbacher, Phys. Rev. B10, 2349 (1974).

13. P. J. Feibelman and D. E. Eastman, Phys. Rev. B10, 4932 (1974).

14. T. Grandke, L. Ley, and M. Cardona, Phys. Rev. Letts. 38, 1033 (1977).

15. J. Stöhr, P. S. Wehner, R. S. Williams, G. Apai, and D. A. Shirley, Phys. Rev. B17, 587 (1978).

16. F. C. Brown, R. Z. Bachrach, S. B. M. Hagström, N. Lien, and C. H. Pruett, Vacuum Ultraviolet Radiation Physics, edited by E. E. Koch, R. Haensel, and C. Kunz (Pergamon, Vieweg, 1974), p. 785.

17. V. Rehn, A. D. Baer, J. L. Stanford, D. S. Kyser, and V. O. Jones, ibid., p. 780.

18. S. Doniach, I. Lindau, W. E. Spicer, and H. Winick, J. Vac. Sci. Technol. 12, 1123 (1975).

19. R. S. Williams, P. S. Wehner, S. D. Kevan, R. F. Davis, and D. A. Shirley, to be published.

20. H. Y. Fan, Phys. Rev. 68, 43 (1945); W. E. Spicer, Phys. Rev. 112, 114 (1958).

21. G. D. Mahan, Phys. Rev. B2, 4334 (1970).

22. J. W. Gadzuk, Electronic Structure and Reactivity of Metal Surfaces, edited by E. G. Derouane and A. A. Lucas (Plenum, New York, 1976), pp. 341-388.

23. N. V. Smith, Photoelectron Spectroscopy of Solids, edited by M. Cardona and L. Ley (Springer-Verlag, Heidelberg, 1977).

24. D. Liebowitz, M. Sagurton, J. Colbert, and N. J. Shevehik, Phys. Rev. Letts. 39, 1625 (1977).

25. J. C. Slater, Symmetry and Energy Bands in Crystals (Dover, New York, 1972).

26. J. Hermanson, Solid State Commun. 22, 9 (1977).

27. P. Heimann, H. Neddermayer, and H. F. Roloff, Phys. Rev. Lett. 37, 775 (1976).

Table I. Bulk Photoemission Polarization Selection Rules for fcc Crystals.[a]

Coordinate Axes			Irreducible Representations	Final State Symmetry	Allowed Initial Symmetries		
x	y	z			ϵ_x	ϵ_y	ϵ_z
[100]	[010]	[001]	$\Delta_1\Delta_1'\Delta_2\Delta_2'\Delta_5$	Δ_1	Δ_5	Δ_5	Δ_1
[001]	[1$\bar{1}$0]	[110]	$\Sigma_1\Sigma_2\Sigma_3\Sigma_4$	Σ_1	Σ_3	Σ_4	Σ_1
[$\bar{1}$10]	[$\bar{1}\bar{1}$2]	[111]	$\Lambda_1\Lambda_2\Lambda_3$	Λ_1	Λ_3	Λ_3	Λ_1
[$\bar{1}$11]	[01$\bar{1}$]	[211]	AB[b]	A	A	B	A

[a] The electron propagation direction defines the z-axis in each case.

[b] Since the [211] axis in momentum space has no special symmetry designation, the symbols A and B chosen to represent the even and odd states, respectively, are those for the usual C_2 symmetry classification.

FIGURE CAPTIONS

Fig. 1. ARPES spectra collected normal to the (111) surface of a Cu single crystal for photon energies between 7 and 32 eV. The feature seen in most of the spectra at 0.3 ± 0.1 eV E_B is due to a surface state present on the (111) face of Cu. The remaining features arise from transitions out of bulk initial state bands.

Fig. 2. The band structure of Cu along several of the major symmetry axes of the BZ is shown for electron energies up to 30 eV above E_F. In the Γ-L direction, corresponding to an electron propagation direction along the [111] axis, there is only a single (free-electron like) final state band available for photoelectron transitions, making this an especially attractive direction for band structure studies by ARPES.

Fig. 3. A comparison of the theoretical bulk band structure of Burdick with the peak positions of the ARPES spectra of Fig. 1. The experimental data were located on the E vs $\vec{k}$ plot by shifting the final state Γ-L band (Fig. 2) vertically downward by an amount equal to the photon energy of the transition in question to locate the allowed $\vec{k}$ coordinates, and then on this line the peak binding energies, referenced to the Fermi level, were plotted (as illustrated for the spectrum at 20 eV photon energy). A photon energy scale for the transitions is shown above the Fermi level for clarity.

Fig. 4. ARPES spectra collected normal to the three low-index crystal faces of Cu in the photon energy regime spanning 32 to 160 eV. The angular resolution was ~ 15 msterad and the energy resolution was better than or equal to 0.2 eV.

Fig. 5. Comparison of experimental peak positions from Fig. 4 with Burdick's band structure of Cu for the three directions investigated. Due to the lack of calculated band structures for Cu more than 30 eV above E_F, an empty lattice final state band (with the zero of energy chosen to coincide with the s-like initial state of the band structure calculation at Γ) was used determine the $\vec{k}$ coordinates of the experimental points. The inset of the top of each panel shows the propagation direction of the photoelectron in the extended zone scheme, and the bottom inset establishes the correspondence between photon energy and the part of the BZ sampled. The scales for each panel are arbitrary.

Fig. 6. ARPES spectra collected in normal emission from a Cu (211) surface for photon energies between 8 and 34 eV. The spectra in the two panels arise from different orientations of the electric field polarization vector $\vec{\varepsilon}$ with respect to the crystalline axes, as shown in the insets of each panel. For the panel on the right, $\vec{\varepsilon}$ was contained in the $(01\bar{1})$ plane (a reflection plane for the (211) surface), while for the panel on the lift $\vec{\varepsilon}$ had components both normal to and within the $(01\bar{1})$ plane.

Fig. 7. Comparison of the peak positions of Fig. 6 with initial state bands of Cu plotted for the [211] direction (calculated by an interpolation scheme fit to Burdick's bands[9]). In both panels the B symmetry initial states are plotted as broken lines and the A symmetry states as solid lines. The most intense peaks in the spectra from the left panel of Fig. 6 correspond to B initial states (top panel). The most intense peaks from the right panel of Fig. 6 correspond to A states.

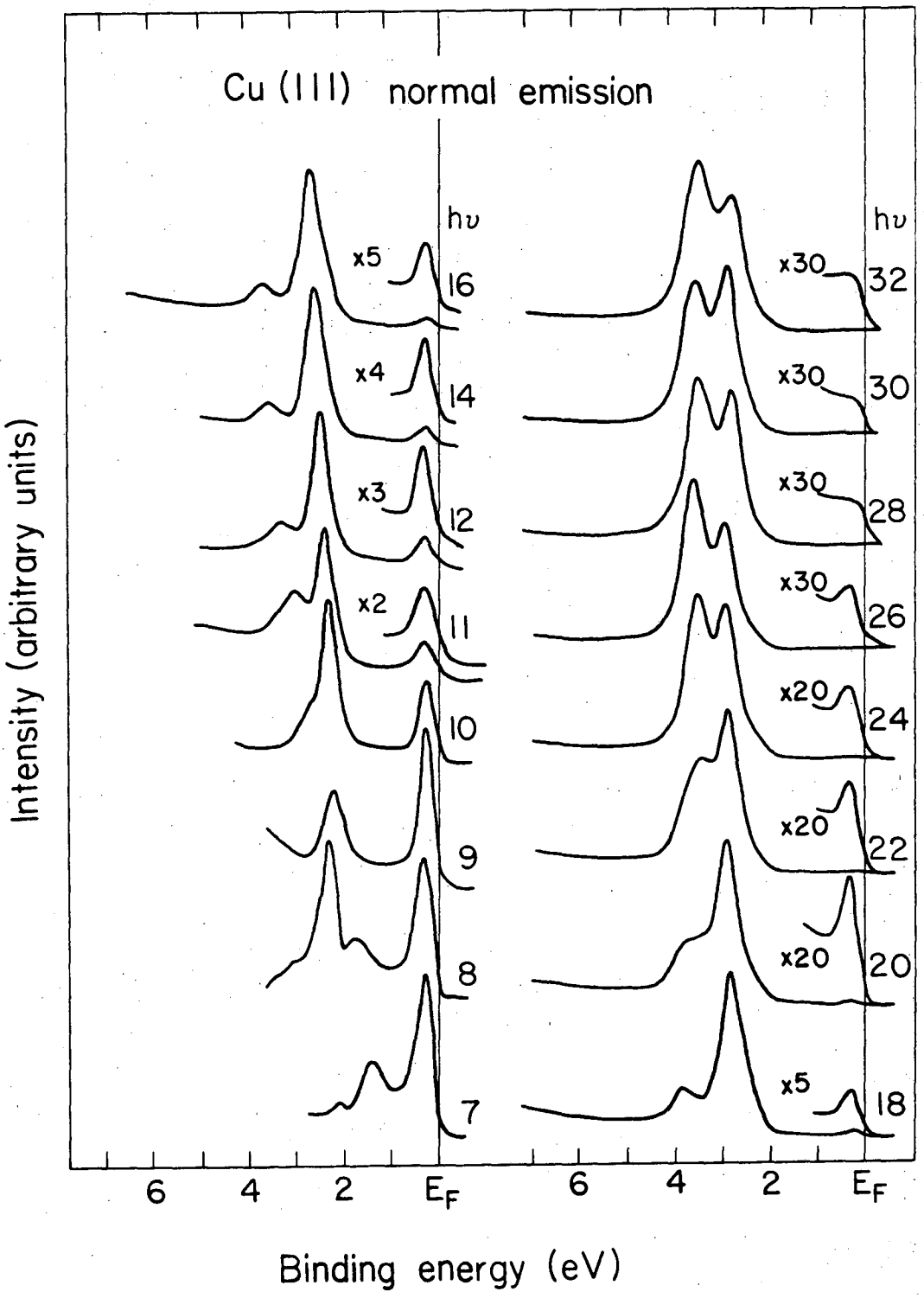

XBL 785-8815

Fig. 1

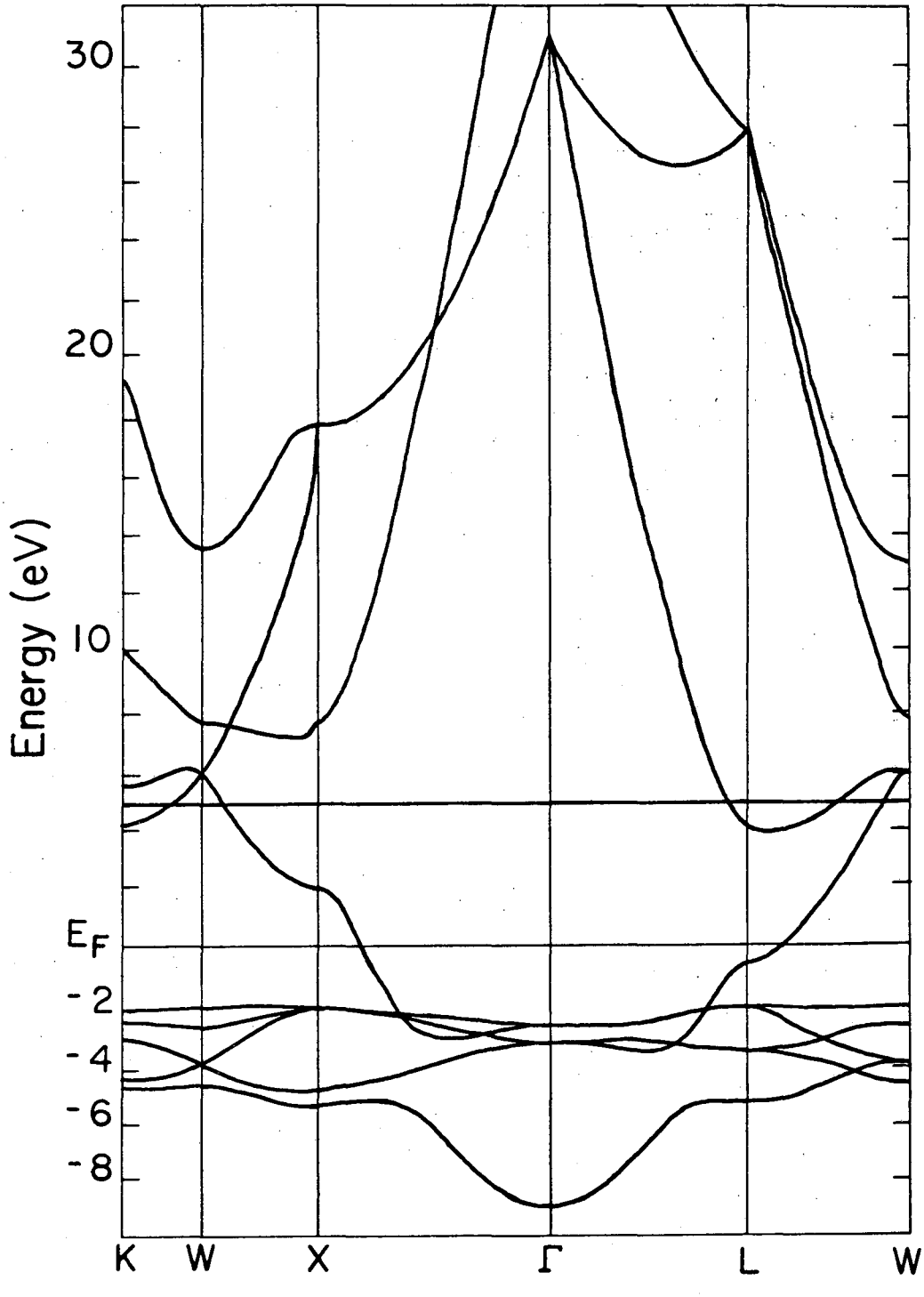

XBL 785-8816

Fig. 2

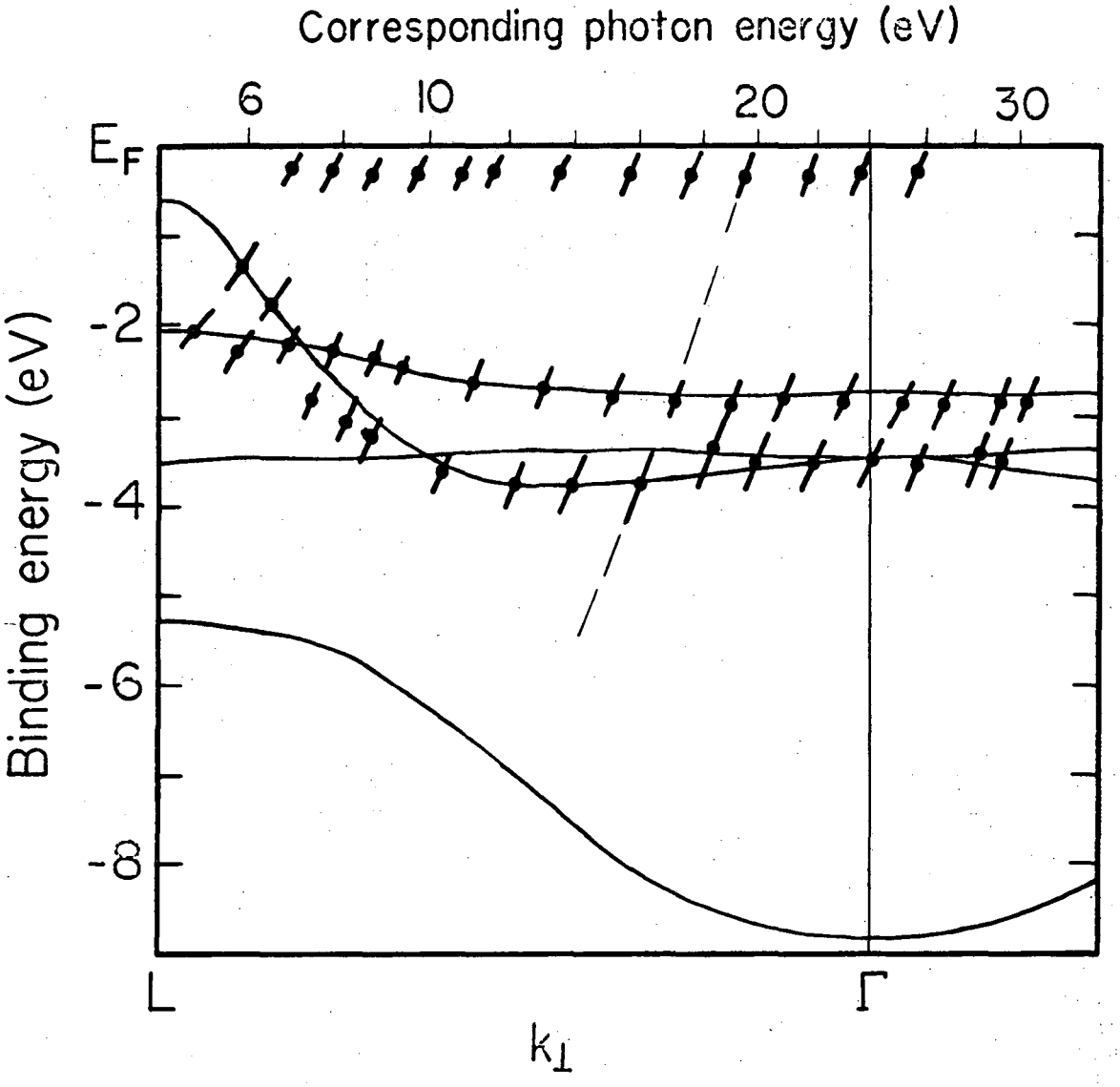

XBL 785-8691

Fig. 3

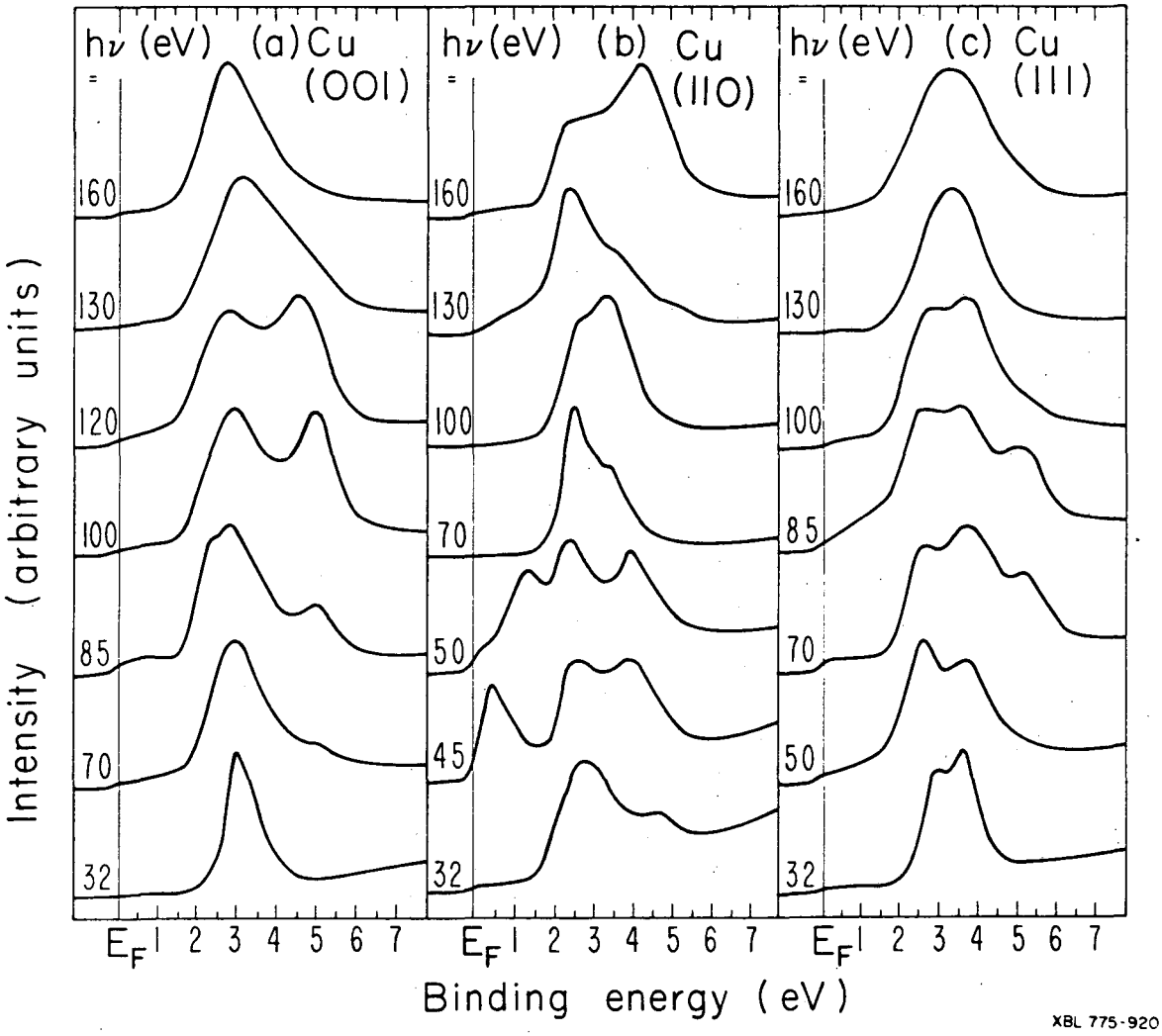
hν (eV) (a) Cu (001)
hν (eV) (b) Cu (110)
hν (eV) (c) Cu (111)
160
130
120
100
85
70
50
45
32
E_F 1 2 3 4 5 6 7
Intensity (arbitrary units)
Binding energy (eV)
XBL 775-920

Fig. 4

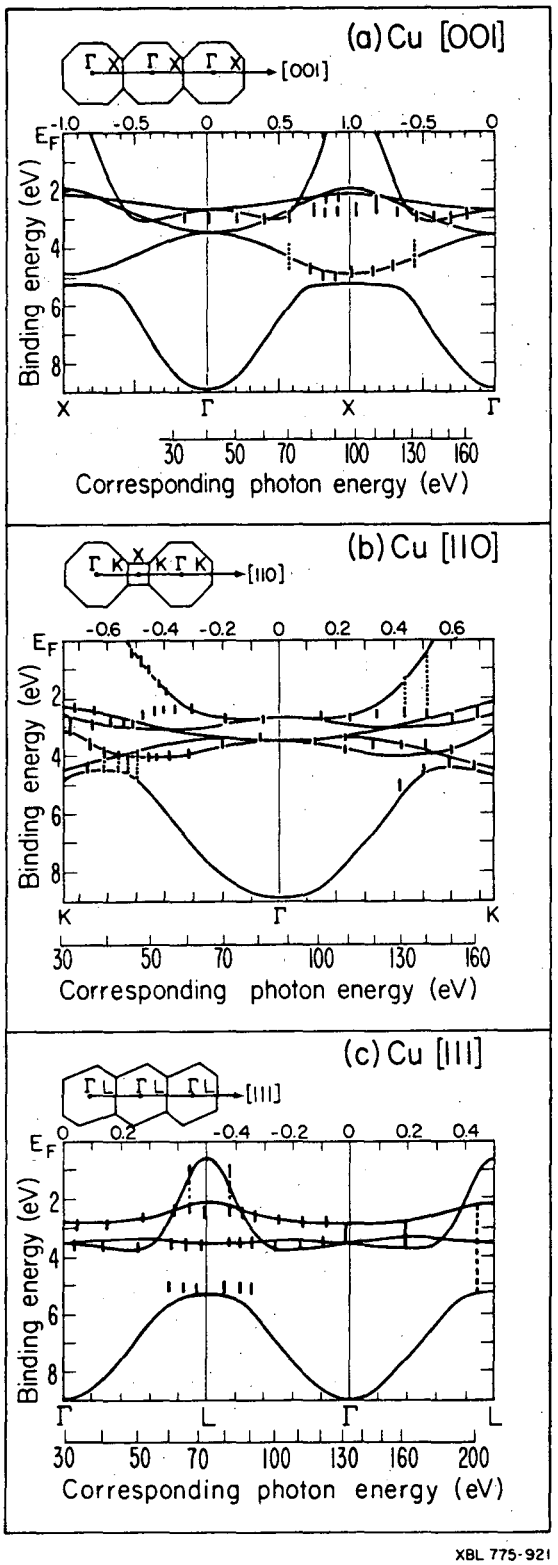
(a) Cu [001]
Γ X Γ X Γ X
[001]
E_F
-1.0 -0.5 0 0.5 1.0 -0.5 0
Binding energy (eV)
2
4
6
8
X Γ X Γ
30 50 70 100 130 160
Corresponding photon energy (eV)
(b) Cu [110]
Γ K X K Γ K
[110]
E_F
-0.6 -0.4 -0.2 0 0.2 0.4 0.6
Binding energy (eV)
2
4
6
8
K Γ K
30 50 70 100 130 160
Corresponding photon energy (eV)
(c) Cu [111]
Γ L Γ L Γ L
[111]
E_F
0 0.2 -0.4 -0.2 0 0.2 0.4
Binding energy (eV)
2
4
6
8
Γ L Γ L
30 50 70 100 130 160 200
Corresponding photon energy (eV)
XBL 775-921

Fig. 5

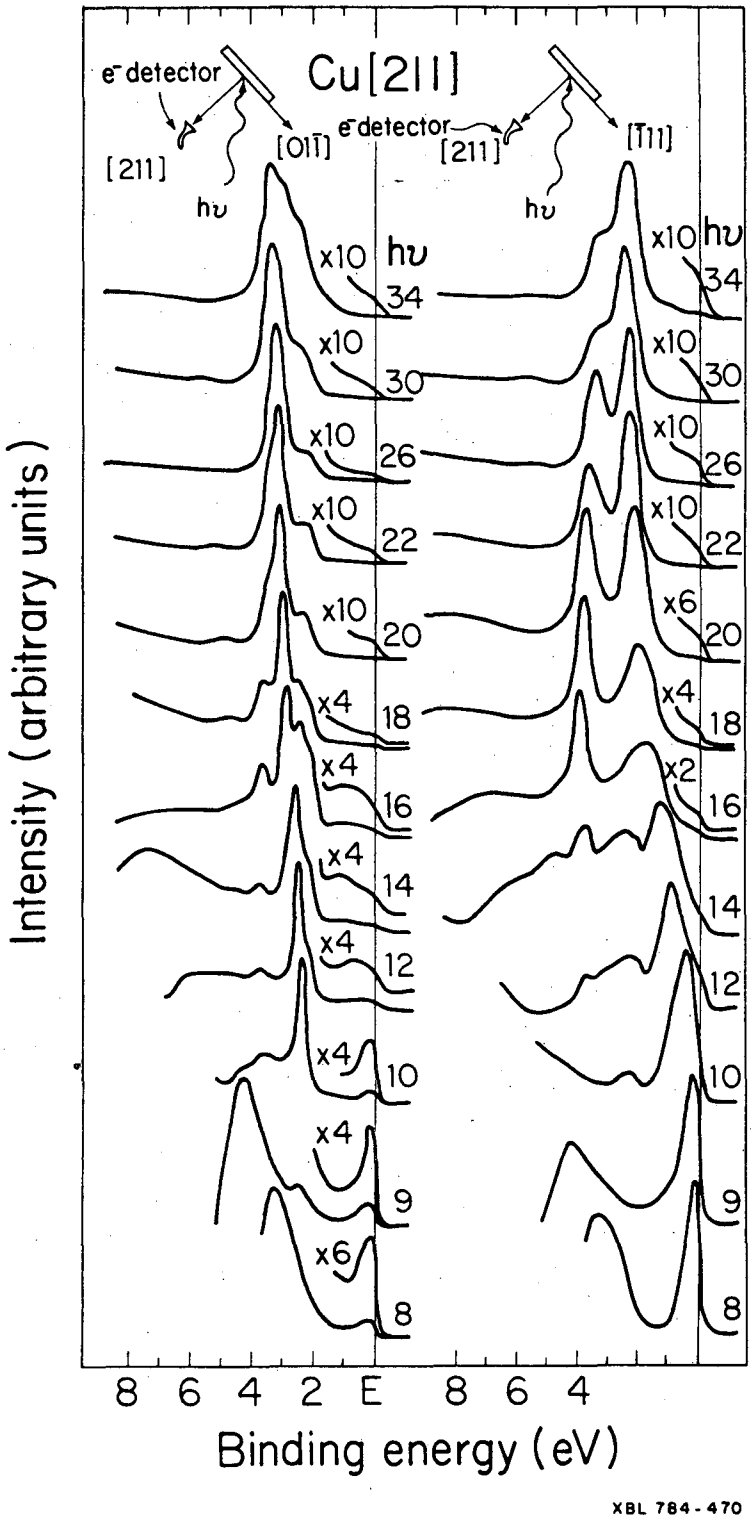
Cu[211]
e⁻ detector
[211]
[01$\bar{1}$]
hυ
e⁻ detector
[211]
[$\bar{1}$11]
hυ
hυ
34
30
26
22
20
18
16
14
12
10
9
8
x10
x6
x4
x2
Intensity (arbitrary units)
8 6 4 2 E 8 6 4
Binding energy (eV)
XBL 784-470

Fig. 6

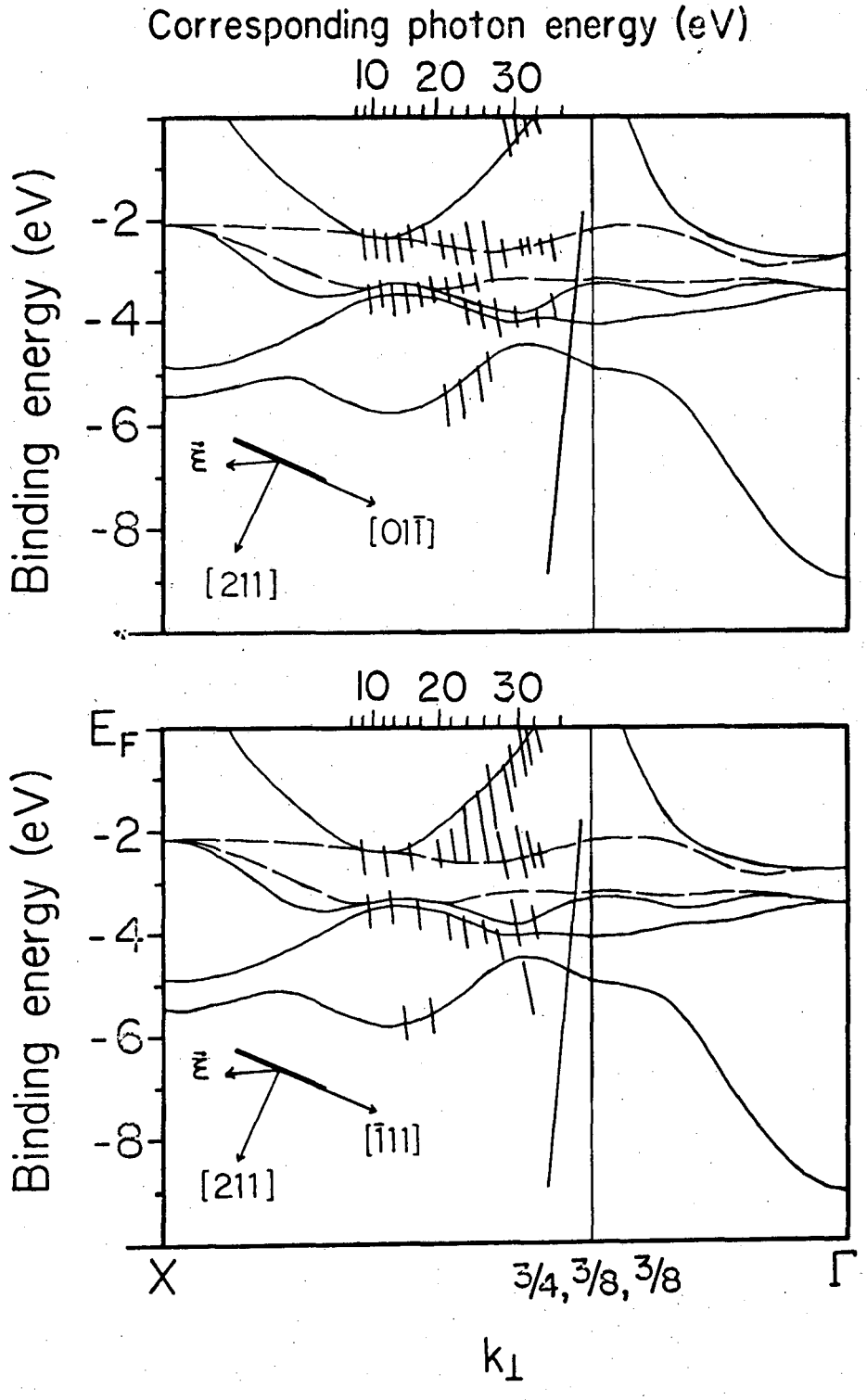

XBL 785-8692

Fig. 7

IV. PHOTOELECTRON INELASTIC MEAN FREE PATHS*

In the past several years photoemission spectroscopy (PES) has become a widely used probe of the electronic structure of solids, with increasing emphasis being placed on the surface capabilities of this and other low-energy electron spectroscopies.[1-6] As previously discussed, the photoemission process in solids may be explained heuristically in terms of the three-step model outlined by Berglund and Spicer.[7] Within the framework of this model, the first step (electron photoexcitation) is responsible for the observed peaks in a photoelectron spectrum. The other two steps (transport through the solid and escape into vacua) contribute the background of electrons scattered out of the main peaks. However, these background effects, such as electron-hole coupling, plasmon excitations, collisionally induced inter-band transitions, etc.[8,9] contribute structure to the photoelectron spectrum which may, as in the case of free-electron-like metals,[10] contain more spectral intensity than the main photoemission peaks.

The study of this background structure, especially plasmon loss peaks, yields important information about the electronic structure of solids and the nature of the photoemission process itself.[11] Surface and bulk plasmon frequencies are easily determined via PES. Recent studies of plasmon satellites have relied on intensity analysis to determine the importance of intrinsic versus extrinsic processes in plasmon excitation.[12-15] This chapter is concerned mainly with the

relation of experimentally observed plasmon loss intensities to the inelastic mean free path (Λ_{ee}) of photoelectrons propagating through a sample, and more generally the effect of Λ_{ee} on observed PES spectra.

In this work, surface and bulk plasmon loss intensities normalized to the main peak intensity were studied in the PES spectra of Al and In. The variations of these relative intensities were studied as functions of electron take-off (for Al only) and electron kinetic energy E_o (which was varied using photons from a synchrotron radiation source). These two parameters determine the effective sampling depth for the photoelectrons which escape into the vacuum. During the course of these studies, possible binding energy differences between bulk and surface atoms and variations in the electronic density of states with surface proximity were investigated utilizing surface sensitivity enhancement techniques.

A. Experimental

The photoemission measurements reported in this paper were performed in two separate experimental chambers. The measurements involving electron take-off angle were conducted in a specially modified Hewlett-Packard Model HP 5950A electron spectrometer[16] which utilizes a monochromotized Al Kα ($\hbar\omega$ = 1486.6 eV) radiation source. The dispersion compensation lens system has an electron angular acceptance cone of approximately 15 msterad,[17] which is sufficiently narrow to allow angle-resolved studies. The details of the angle variation procedure have been previously reported.[18] The measurments dealing with plasmon

intensity variations due to changes in initial electron kinetic energy were performed in an ion-pumped UHV stainless steel bell jar system installed on the 4^{o} station of Beam Line I at the Stanford Synchrotron Radiation Laboratory (SSRL).[19] The photon source was synchrotron radiation from the electron-positron storage ring SPEAR at the Stanford Linear Accelerator Center (SLAC). The radiation was monochromatized and the photon energy was varied by a grazing incidence "grasshopper" monochromator.[20] Photoelectrons were energy analyzed with a double-pass cylindrical mirror analyzer (CMA), Physical Electronics Model PHI 150255G. The experimental geometry is shown in Fig. 1. Note that the experimental geometry was chosen to integrate over electron take-off angles between normal and grazing escape.

A freshly evaporated aluminum film was used in the angle variation studies. Possible carbon and oxygen contaminants were monitored by scanning the photoemission spectral regions near their respective 1s binding energies. Contaminant levels were below the detection sensitivity of XPS, i.e., less than 0.1 monolayer. The Al sample used for the synchrotron radiation studies was an evaporated film from a 99.999% pure foil on a stainless steel substrate. Repeated depositions of Al were required to minimize the intensity of the oxide satellite of the Al 2p peak. The base pressure of the system was $\leq 2 \times 10^{-10}$ torr and the relative intensities of the Al 2p and its oxide satellite did not change during the 26 hour duration of the experiment. The In sample was cut from an ingot of 99.999% pure In. The sample was mechanically polished, then etched in warm aqua regia immediately prior to installation in the experimental

chamber. The base pressure in the chamber was 1×10^{-9} torr, as no bake-out was performed. The sample was Ar^+ ion-bombarded briefly to remove surface impurities. The In spectra revealed no core line shifts due to contamination.

In order to analyze the relative intensities of the core peaks and plasmons, the spectra were least-squares fitted to Gaussian peak shapes plus a background using the program GAMET.[21] The overall spectral background and individual peak tail functions were chosen to yield a best fit to the experimental data, and do not necessarily represent a justifiable separation of physical effects (i.e. electron-hole coupling) from the main peaks. However, processes causing peak asymmetries should be self cancelling when considering relative intensities.

B. Surface Sensitivity Enhancement of Photoemission Measurements

1. Variation of effective escape depth with photoelectron take-off angle.

In 1969 Harris[22] showed that the surface sensitivity in Auger electron emission is enhanced by using low electron take-off angles ϕ. Enhancement of surface sensitivity in XPS by this technique was first demonstrated by Fraser et al.[23] and by Fadley et al.[24] Subsequently Fadley and co-workers have carried out detailed studies of the effects of such parameters as surface roughness on the ϕ-dependence of XPS spectra.[25] This section presents data illustrating the surface enhancement effect for the 2s line of aluminum at XPS energies.

Values of the electron attenuation length Λ_{ee} have been measured for a variety of solids by the use of such methods as overlayer deposition.[26-29] For XPS photoelectrons from loosely-bound orbitals (kinetic energies ~ 1000 eV), the Λ_{ee} values lie in the 15-30 Å range. Thus in normal emission the effective sampling depth Λ_{ee}' is 5-10 atomic layers. Figure 2 illustrates the relation between Λ_{ee}' and ϕ, defined as the angle between the electron propagation direction and the sample plane. Clearly

$$\Lambda_{ee}' = \Lambda_{ee} \sin\phi . \qquad (2)$$

Thus for Λ_{ee} ~ 15-30 Å, observation at practically achievable angles ($\phi \sim 5^{\circ}$-10°) will give very high surface sensitivity.

Figure 3, which shows the Al 2s spectra taken at $\phi = 7.5^{\circ}$ and $\phi = 51.5^{\circ}$ from the same Al film, demonstrates this sensitivity. The Al film was freshly evaporated from an Al charge which was not completely outgassed (the measurement at $\phi = 7.5^{\circ}$ was obtained before that at $\phi = 51.5^{\circ}$). Spectrum (b) shows just one peak with an asymmetry to higher binding energy which is often seen in metals and generally attributed to electron-hole coupling.[39,31] However, spectrum (a) clearly reveals two peaks, one due to the metal and one due to a surface oxide. In the case of Fig. 3, the surface sensitivity of spectrum (b) was increased by approximately a factor of six over that in spectrum (a). Thus Λ_{ee} in XPS can become as low as 2 Å or nearly one atomic layer. Such surface sensitivity enhancement should be of great utility in investigating surface phenomena and in differentiating between surface and bulk contributions to XPS spectra. This is a practical method of depth profiling in a non-

destructive manner, i.e., without having a ion-sputter.

Figure 4 shows the Al 2s spectral region from an evaporated metal film in XPS measurements at three different takeoff angles. The spectra show only the Al 2s core-level peak and the first surface and bulk plasmon peaks. The binding energy of the Al 2s peak was measured to be 117.85 eV with respect to the Fermi level of Al. The surface and bulk plasmon energies, 10.5 eV and 15.2 respectively, agree with previously reported values (Ref. 12) and do not vary with take-off angle.

Inspection of Fig. 4 shows that the surface plasmon loss peak intensity increases greatly relative to both the primary peak and the bulk plasmon peak as the electron take-off angle is decreased. This is to be expected because at low ϕ the escaping photoelectron has a lower component of velocity normal to the surface and thus "spends more time" in the surface layer than an electron with higher ϕ. The bulk plasmon peak intensity relative to the primary peak decreases only slightly at lower ϕ. These observations will be discussed in more detail below.

2. Surface sensitivity variation as a function of photoelectron kinetic energy

The well known "universal curve", Fig. 5, illustrates the variation of electron attenuation length, or mean free path, with kinetic energy for nearly all materials for which these determinations have been made.[32] The strong dependence of Λ_{ee} on E_o suggests that PES experiments could be performed utilizing different photon energies to selectively probe the electronic structure of solid surfaces; i.e., photon energies would be chosen such that the photoelectrons from the peak being studied would

have a kinetic energy corresponding to the minimum possible Λ_{ee}. Unfortunately, there are too few discrete photon sources to carry out extensive measurements of this type (Fig. 5 shows the main laboratory sources now in use in relation to the universal curve). However, synchrotron radiation provides an intense source of continuous radiation throughout the range of interest. With proper monochromatization, it is possible to obtain spectra throughout the universal curve and in particular in the most surface-sensitive region.

Such experiments have been performed for the 130 eV $\leq \hbar\omega \leq$ 280 eV photon energy range using synchrotron radiation to study the Al 2p peak and with 80 eV $\leq \hbar\omega \leq$ 180 eV for the In 4d peak. These experiments were performed in an angle-integrated mode; i.e., utilizing the full acceptance cone of the CMA, due to the low count rates in the plasmon loss peaks. The spectra for the Al 2p region including the bulk (B) and surface (S) plasmons are given in Fig. 6 for several photon energies near the minimum of the universal curve. As can be seen in these spectra, the film is somewhat oxidized. For comparison, the Al 2p spectrum obtained at XPS energies is given in Fig. 7. The surface and bulk plasmon energies were independent of photoelectron kinetic energy. Representative spectra from the In 4d region are shown in Fig. 8. The surface and bulk plasmon energies (8.6 and 11.7 eV respectively) displayed no measurable dispersion. The In 4d XPS spectrum (after Ref. 12) is shown in Fig. 9 for comparison.

3. Binding energies of bulk atoms vs. surface atoms.

Before discussing the plasmon intensity variations, some ancillary results obtained during and in conjunction with the plasmon studies will be presented. The effect of the solid vacuum interfere at the surface layer of a solid is a subject of considerable interest. Changes in both the core binding energies and the valence level density of states from the bulk values may be expected at the surface since each atom no longer has a full complement of neighbor atoms. The surface sensitivity achievable in PES measurements should illuminate these points.

Several XPS spectra were taken of core-levels of Al and Ni films which were freshly evaporated in situ under UHV conditions. These films exhibited no sign of contamination as revealed by in situ chemical analysis of core-level spectra of possible common contaminants. The measurements at low ($\phi = 7.5^{\circ}$) and high ($\phi = 51.5^{\circ}$) take-off angles found no evidence for a difference between surface and bulk binding energies, referenced to the Fermi level, within ±0.15 eV. The low angle spectrum of Al (Fig. 4), did reveal a shoulder due to a minute amount of surface oxide (< .05 monolayer).

In the synchrotron radiation studies, the binding energies of the In 4d peaks with respect to the In Ferni level showed no discernible photon energy dependence. Also, there were no observable satellites attributable to surface atoms in the high resolution spectra taken of the In 4d levels at surface sensitive electron energies. Further evidence against large binding energy shifts of surface atoms came in angle-resolved[33] studies of the 4f levels of a clean platinum (111)

single crystal surface. These studies utilized different photon energies and electron take-off angles to vary the effective photoelectron sampling depth. As in the other experiments, there were no observable satellites or binding energy shifts in the most surface sensitive PES spectra. The lack of a core level binding-energy shift between surface and bulk atoms is surprising if one attempts to understand the condensed-phase core-level binding energies in terms of free-atom values. There are large shifts (5-10 eV) from free atom values for condensed-phase binding energies.[34] These shifts are usually explained as arising from combinations of differences in initial-state charge distribution and extra-atomic relaxation. Apparently these initial and final state effects are either very small or cancel each other to a large extent. Further theoretical developments and experimental results are required to determine the nature of such electronic structure and perhaps isolate cases in which significant binding energy shifts due to atomic location exist.

Even though the calculation of Sohn, et al.,[35] indicate that substantial variations in the density of states occur as a function of depth below a solid surface, experimental evidence for this effect collected at SSRL are negative.[36] In general, PES studies of clean surfaces are studies of bulk electronic properties.

C. Photoelectron Energy Loss Mechanisms

1. Angular dependence of Al plasmon loss intensities.

A general review of plasmon excitations in solids was given by Raether.[37] Comprehensive theoretical treatments of the relation between electron mean free paths (MFP's) and plasmon satellite intensities were given by Feibelman[9] and Šunjić and Šokčević.[11] The latter authors have treated the specific example of plasmon loss structure from the Al 2p level. Reference 11 shall serve as a basis for the interpretation of the above experimental data.

If it is assumed that the bulk plasmon excitation process is predominantly extrinsic and has the form (Ref. 13)

$$I_B^o \propto \lambda_B/(1+\lambda_B/\Lambda_{ee})^2 \qquad (2)$$

where I_B^o is the first bulk plasmon loss to main peak intensity ratio, λ_B is the electron MFP for bulk plasmon creation events, and Λ_{ee} is the MFP for all collision processes, then I_B^o is independent of ϕ. A further simple assumption, that surface plasmon excitation probability is proportional to the amount of time required for a photoelectron to traverse the surface layer, yields a surface plasmon to main peak ratio (I_S^o) proportional to $(\sin\phi)^{-1}$. However, Refs. 9 and 11 have shown that the introduction of a solid-vacuum interface alters the local character of bulk (and surface) plasmon excitations. Thus surface and bulk excitation probabilities (Q_S and Q_B) become functions of the electron excitation depth (L) and takeoff angle (ϕ) as well as electron kinetic energy.

Figure 10 shows I_B^o and I_S^o as functions of Λ_{sr} and ϕ for photoelectrons excited from the Al 2p level with Mg Kα radiation (electron kinetic energy ≈ 1176 eV) where Λ_{sr} is the MFP due only to short-range interactions (i.e. electron-hole creation). The values for I_B^o and I_S^o were generated by fitting plasmon excitation probabilities Q_B and Q_S of Fig. 5 in Ref. 11 to a series of line segments and performing the integration of Eq. 21 in Ref. 11 analytically. Since Šunjić and Šokčević presented plasmon excitation probabilities for only three exit angles (ϕ = 90°, 50°, and 20°), interpolated and extrapolated Q_B and Q_S values were used to compute the plasmon intensity angular dependence from normal to grazing ϕ. Thus Fig. 10 is presented only to indicate trends.

The experimental data, presented in Table 1, represent mainly plasmon loss structure following the Al 2s peak using Al Kα radiation as an excitation source (kinetic energy = 1368 eV). However, it is still justified to compare the experimental data to Fig. 10 since Fig. 6 and 7 in Ref. 11 show that Q_B and Q_S for Al are insensitive to 200 eV differences in electron kinetic energy for energies above 1 keV.

Direct comparison of the experimental results to Fig. 10 indicate that the plasmon loss probabilities Q_B and Q_S have been underestimated in Ref. 11. However, the ratio I_B^o/I_S^o (which is more sensitive to Λ_{ee} and ϕ than either I_B^o or I_S^o) may still be correctly predicted. Figure 11 (I_B^o/I_S^o versus ϕ) was generated from a complete set of I_B^o and I_S^o curves taking Λ_{sr} to be 25 Å.[39] Except for small angles, the resulting I_B^o/I_S^o curve follows the $\sin\phi$ prediction of the simple approximations mentioned at the beginning of this section. It is also seen that surprisingly good agreement exists between the three experimental values and the predicted I_B^o/I_S^o ratios.

The main point of disagreement between the predictions of Fig. 10 and the experimental results is that the observed I_B^o ratio decreases with decreasing ϕ. That the computations predict the opposite behavior is most likely due to the rough parameterization and extrapolation of the results of Ref. 11. Since the $\sin\phi$ behavior of I_B^o/I_S^o is valid over a large angular range, the variation of bulk plasmon excitations from a local process occurs only in a region very near the surface. For XPS spectra with a large effective sampling depth, the observed electron loss spectra can be interpreted mainly in terms of a MFP due to local bulk plasmon excitations and short-range excitations. From the slope of I_B^o ($\phi = 90°$) for large Λ_{sr} one can approximate $\lambda_B = 42$ Å (λ_B is the mean free path for bulk plasmon excitation). Thus, $\Lambda_{ee} \simeq (\Lambda_{sr}^{-1} + \lambda_B^{-1})^{-1}$ or 15.7 Å, which is close to the experimentally observed value of 18 Å from Ref. 24.

2. Kinetic energy dependence of I_B^o and I_S^o for Al and In.

The variations with electron kinetic energy of I_B^o and I_S^o are shown in Fig. 12 for the Al 2p case and in Fig. 13 for In 4d. All spectra were angle-integrated. A detailed interpretation is not feasible because no calculations are available which treat the explicit angle, energy, and Λ_{ee} dependence of I_B^o and I_S^o in the energy range of these experiments.

An Al 2p oxide satellite peak appears in all the spectra in Fig. 6 with ~30% the intensity of the main peak. However, the Al plasmon intensities of this work agree well with the spectra of S. A. Flodstrom, et al.[40] taken on an oxide-free sample at fewer energies (see Fig. 12).

The Al LMM Auger peak (evident at ~ 100 eV "binding energy" in the 170 eV photon energy spectrum of Fig. (6) renders an accurate determination of I_B^o and I_S^o impractical for photon energies 130 eV < $\hbar\omega$ <170 eV. Also, for $\hbar\omega$ < 130 eV both a strongly nonlinear inelastic electron background and rapidly decreasing plasmon intensities preclude accurate tracking of I_B^o and I_S^o to their respective threshold energies.

Figure 12 shows that for electron kinetic energies above 93 eV, I_B^o increases with energy while I_S^o decreases. The calculations of Ref. 11, which were all for initial electron kinetic energies $\geq$ 100 eV, showed that the bulk plasmon excitation probability decreases with increasing electron kinetic energy. This is consistent with the experimental results if Λ_{ee} increases faster with kinetic energy than the bulk plasmon excitation probability decreases. Figure 7 in Ref. 11 also shows that the surface plasmon excitation probability can increase or decrease rapidly in the energy range around 100 eV, depending on the effective escape depth sampled. The observed slight decline in intensity is most likely due to sufficiently large (~ 3 Å) and steadily increasing Λ_{ee} for electron kinetic energies between 93 and 193 eV. From Ref. 39 it is seen that Λ_{ee} in Al is predicted to be a minimum (~ 3 Å) at 50 eV and rise to 6 Å at 200 eV, which is in qualitative agreement with Fig. 5 (the calculations of Kleinman[41] place the minimum of Λ_{ee} near 15 eV and are thus not in accord with experimental observations). At these low electron kinetic energies much of the plasmon loss signal orginates in a region where the bulk plasmon excitation process is non-local, thus requiring very detailed calculations to predict the angle and energy dependence of the plasmon loss peaks.

The observed I_B^o/I_S^o ratio for Al at 53 eV is greater than or equal to that in the range of 93-123 eV. By the considerations of the preceding paragraph and Fig. 10 this would indicate that the minimum in Λ_{ee} occurs somewhere between 53 eV and 93 eV photoelectron kinetic energy. In this case a better determination is not possible due to the Auger interference in the region of interest. Further complications in the interpretation of plasmon intensity data may also arise due to elastic electron scattering from the surface potential considered in Ref. 29.

The predicted Λ_{ee} for In is lower than for Al at all electron kinetic energies,[42] so surface effects should be more enhanced for In over Al. Indeed it is observed (Figs. 6-9) that the ratio I_B^o/I_S^o for In is much lower than for Al, although the bulk plasmon excitation probability is smaller for In. Figure 13 shows that I_B^o and I_S^o for In are nearly equal over the range of electron energies 53-123 eV, and change little with energy. A narrow energy region is obsered over which $I_S^o > I_B^o$ ($\hbar\omega = 160$ eV) and the intensities then invert ($\hbar\omega = 180$ eV). The electron kinetic energy of this very surface sensitive region is around 143 eV, which is near the bottom of the universal curve. However, there may be a resonant process which accounts for the apparent narrow minimum in Λ_{ee} which has not been explored theoretically thus far.

D. The Self Energy Perturbation in Photoemission

This chapter has demonstrated that surface sensitivity in PES can be greatly enhanced by either using low electron take-off angles or by utilizing a photon energy such that the photoelectron kinetic energy is near the minimum of the "universal curve". Further, the surface sensitivity of a particular take-off angle and energy can be monitored by observing surface and bulk plasmon loss intensities. The angular dependence of the bulk to surface plasmon loss feature ratios in photoemission spectra of Al was predicted quite well by Šunjić and Šokčević.[11]

An important auxiliary result that arises in considering plasmon loss phenomena is that the three step model of photoemission is not valid for calculating plasmon excitation phenomena. Intrinsic plasmon creation, i.e., a collective excitation produced by the "sudden" creation of a hole, is associated with the "first step" of photoemission from a solid. Extrinsic excitations are due to the coupling of the photoelectron to the plasma modes, which occurs during the "transport step." The proper computation of the total plasmon creation probability results from squaring the Hamiltonian matrix element which connects the ground state of the system to the excited state which is comprised of a photoelectron and a plasmon. Thus, there are cross terms in the plasmon excitation probability which contain contributions from both the "excitation" and "transport" steps. This argument merely illustrates that fact that photoemission is in essence a one step phenomenon, and that the three steps are in effect virtual phenomena which are not physically separable

The question that must now be addressed is how to formulate a one electron description of photoemission which retains most of the simplicity of the three step model (which has been shown to be nearly valid for no loss photoelectron features) yet recognizes the true one step nature of photoemission. A major improvement in the direct transition theory outlined in Chapter III is the inclusion of a loss term in the Hamiltonian of the system studied. This is achieved by defining an imaginary component of the potential energy which is itself a function of the photoelectron kinetic energy. This term, known as the self energy, accounts for the finite photoelectron inelastic mean free path which is the result of such many body effects as plasmon or pair creation. The inclusion of the self energy into the photoemission model being constructed and its physical consequences are the dominant topics of the next chapter.

REFERENCES

*This chapter appeared in part as "Angle- and Energy-Dependent Core-Level Photoelectron Energy Loss Studies in Al and In," R. S. Williams, S. P. Kowalczak, P. S. Wehner, G. Apai, J. Stöhr, and D. A. Shirley, J. Electron Spectrosc. Relat. Phenom. 12, 477 (1977).

1. D. E. Eastman in Vacuum Ultraviolet Radiation Physics, ed. E. Koch, R. Haensel, and C. Kunz, (Pergamon, Vieweg, 1974), p. 417.
2 W. E. Spicer in Optical Properties of Solids: New Developments, ed. B. O. Seraphin (North-Holland Publishing Co., Amsterdam 1976) p. 633.
3. D. A. Shirley, Adv. Chem. Phys. 23, 85 (1973).
4. R. E. Watson and M. L. Perlman, Structure and Bonding 24, 83 (1975).
5. P. Feibelman and D. E. Eastman, Phys. Rev. B10, 4932 (1974).
6. J. B. Pendry, Surface Sci. 57, 679 (1976).
7. C. N. Berglund and W. E. Spicer, Phys. Rev. 136, A1030 (1964).
8. E. Bauer, J. Vac. Sci., Technol. 7, 3 (1969).
9. P. Feibelman, Phys. Rev. B7, 2305 (1973) and Surface Sci. 36, 558 (1973).
10. S. P. Kowalczyk, L. Ley, F. R. McFeely, R. A. Pollak, and D. A. Shirley, Phys. Rev. B8, 3583 (1973).
11. M. Šunjić and D. Šokčević, J. Electron Spectrosc. Relat. Phenom. 5, 963 (1974) and Sol. St. Comm. 18, 373 (1976).
12. R. A. Pollak, L. Ley, F. R. McFeely, S. P. Kowalczyk, and D. A. Shirley, J. Electron Spectrosc. Relat. Phenom. 3, 381 (1974).

13. W. J. Pardee, G. D. Mahan, D. E. Eastman, R. A. Pollak, L. Ley, F. R. McFeely, S. P. Kowalczyk, and D. A. Shirley, Phys. Rev. B11, 3614 (1975).

14. G. A. Sawatzky, A. Barrie, and G. Jonkers, private communication.

15. J. C. Fuggle, D. J. Fabian, and L. M. Watson, J. Electron Spectrosc. Relat. Phenom. 9, 99 (1976).

16. R. A. Pollak, Ph.D. thesis, University of California, Lawrence Berkeley Laboratory Report, LBL-1299 (1972) unpublished.

17. H. Weaver, private communication and independently computed by Gus Apai using typical lens operating voltages.

18. S. P. Kowalczyk, Ph.D. thesis, University of California, Lawrence Berkeley Laboratory Report, LBL-4319 (1976) unpublished.

19. H. Winick, Ref. 1, p. 776.

20. F. C. Brown, R. Z. Bachrach, S. B. M. Hagstrom, N. Lien, and C. H. Pruett, Ref. 1, p. 785.

21. C. S. Fadley, Ph.D. thesis, University of California, Lawrence Berkeley Laboratory Report, UCRL-19535.

22. L. A. Harris, Surf. Sci. 15, 77 (1969).

23. W. A. Fraser, J. V. Florio, W. N. Delgass, and W. D. Robertson, Surf. Sci. 36, 661 (1973).

24. C. S. Fadley, R. J. Baird, W. Siekhaus, T. Novakov, and S.A.L. Bergström, J. Electron Spectrosc. Relat. Phenom. 4, 93 (1974).

25. C. S. Fadley, Progress in Solid State Chemistry 11, 265 (1976).

26. P. W. Palmberg and T. N. Rhodin, J. App. Phys. 39, 2425 (1968); P. W. Palmberg, Anal. Chem. 45, 549A (1973).

27. I. Lindau and W. E. Spicer, J. Electron Spectrosc. Relat. Phenom. 3, 409 (1974).

28. C. J. Powell, Surf. Sci. 44, 29 (1974).

29. J. C. Tracy, J. Vac. Sci. Technol. 11, 280 (1974); J. C. Tracy and J. M. Burkstrand, CRC Critical Reviews in Solid State Sciences 4, 381 (1974).

30. G. K. Wertheim and S. Hüfner, J. Inorg. Nucl. Chem. 38, 1701 (1976); S. Hüfner, G. K. Wertheim, D. N. E. Buchanan, and K. W. West, Phys. Lett. 46A, 420 (1974); S. Hüfner and G. K. Wertheim, Phys. B11, 678 (1975).

31. Quantitative determinations of photoemission peak broadening must be approached carefully when attempting to relate peak asymmetries to electronic properties of the system studied. Contaminant levels too small to be detected by XPS observation of core lines can be responsible for slight peak broadening (see Fig. 4).

32. C. R. Brundle, Surface Science 48, 99 (1975), and Refs. 26-29.

33. J. Stöhr, G. Apai, P. S. Wehner, F. R. McFeely, R. S. Williams, and D. A. Shirley, Phys. Rev. B14, 5144 (1976).

34. D. A. Shirley, R. L. Martin, S. P. Kowalczyk, F. R. McFeeley, and L. Ley, Phys. Rev. B15, 544 (1977).

35. K. S. Sohn, D. G. Dempsey, L. Kleinman, and E. Caruthers, Phys. Rev. B13, 1515 (1976); Phys. Rev. B14, 3185 (1976); Phys. Rev. B14, 3193 (1976).

36. P. S. Wehner, R. S. Williams, G. Apai, J. Stöhr, and D. A. Shirley, unpublished results.

37. H. Raether, Springer Tracts in Modern Physics 38, 84 (1965).

38. R. J. Baird and C. S. Fadley, to appear in the Proceedings of the International Study Conference on Photoemission from Surfaces, Noordwijk, Holland, 1976.

39. D. R. Penn. Phys. Rev. b 13, 5248 (1976).

40. S. A. Flodstrom, R. Z. Bachrach, R. S. Bauer, J. C. McMenamin, and S. B. M. Hagstrom, J. Vac. Sci. Tech. 14, 303 (1977).

41. L. Kleinman, Phys. Rev. B3, 2982 (1971).

42. D. R. Penn, J. Electron Spectrosc. 9, 29 (1976); and private communications.

Table I

Angular Dependence of Al Plasmons in XPS

Plasmon loss structure	Take-off angle		
	54°	38°	7.5°
Al 2p I_S^O		0.17(1)	
Al 2p I_B^O		0.57(2)	
Al 2s I_S^O	0.11(1)	0.14(1)	0.22(3)
Al 2s I_B^O	0.55(2)	0.58(3)	0.46(6)

FIGURE CAPTIONS

Fig. 1. Experimental geometry for the experiments performed using the storage ring SPEAR as a source of synchrotron radiation is shown. The angle of the sample with the CMA symmetry axis was chosen to maximize the count rate with the angle between the incident photon beam and the CMA symmetry axis fixed. The cross-hatched area illustrates the acceptance cone of the CMA.

Fig. 2. The experimental geometry for the XPS angle resolved experiments is shown, illustrating the concept of effective sampling depth, Λ'_{ee} (Eq. 1). The photon source, monochromatized Al Kα radiation, is fixed with respect to the electron analyzer.

Fig. 3. The XPS spectra of the Al 2s region of an oxidized evaporated film is shown. The oxide peak is greatly enhanced at low take-off angle because of the increased surface sensitivity with smaller effective sampling depth.

Fig. 4. The Al 2s spectral region as a function of take-off angle obtained using Al Kα x-rays. Note that the spectrum taken at $\phi = 7.5^{\circ}$ shows a slight shoulder at higher binding energies due to oxide contamination, even though a scan of the O 1s region revealed no detectable signal.

Fig. 5. This is a representation of the universal curve—the electron attenuation length (Λ_{ee}) as a function of electron kinetic energy. Superimposed on this plot are discrete laboratory photon sources which are commonly used in PES.

Fig. 6. The Al 2p spectral region at various photon energies in the ultra-soft x-ray regime. The in.situ evaporated Al film had an oxide component, seen as a shoulder on the Al 2s peak at higher binding energy. The spectra broaden at higher photon energies due to the degradation of the monochromator resolution.

Fig. 7. The Al 2p spectral region obtained with Al Kα ($\hbar\omega \sim 1486$ eV) radiation is shown for a takeoff angle of 38°.

Fig. 8. The In 4d spectral region obtained at various photon energies in the ultra-soft x-ray regime. Note the change in plasmon loss peak intensities between 160 eV and 180 eV.

Fig. 9. The In 4d spectral region obtained with Al Kα radiation.

Fig. 10. This figure shows the predicted dependence for Mg Kα excitation of the first surface and first bulk Al 2p plasmon loss peak intensities normalized to the main peak (I_S^o and I_B^o) on take-off angle and Λ_{sr}, the mean free path for short range inelastic collisions.

Fig. 11. Variation of the surface to bulk plasmon ratios (I_B^o/I_S^o) as a function of electron take-off angle ϕ is shown. The solid line is the predicted ratio variation from Fig. 10 assuming an electron Λ_{ee} of 25 Å. The dashed continuation of the solid curve is proportional to sin ϕ. Experimental values obtained in this study are shown with error bars to denote the uncertainty in the plasmon peak intensity determination.

Fig. 12. Variation of the normalized Al bulk and surface plasmon loss peak intensities (I_B^o and I_S^o) with energy (bottom). The filled circles and the crosses represent I_B^o and I_S^o respectively from this work; the filled diamonds and squares represent the data of Ref. 40. The top portion shows the ratio I_B^o/I_S^o (filled circles from this work, filled squares from Ref. 40).

Fig. 13. The variation of I_B^o (filled circles) and I_S^o (crosses) for plasmon losses following the In 4d peak as a function of photon energy.

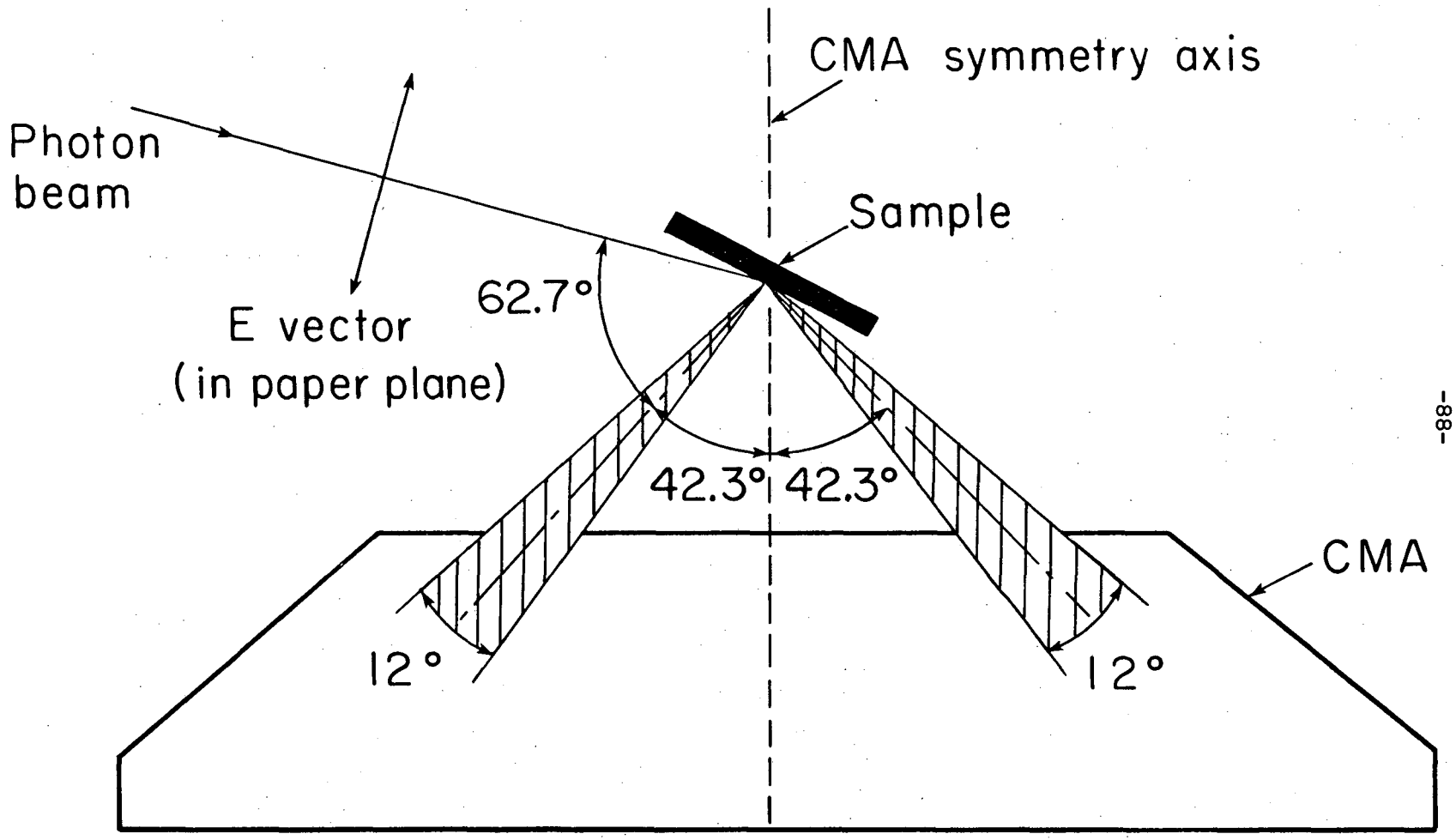

XBL 764-2732

Fig. 1

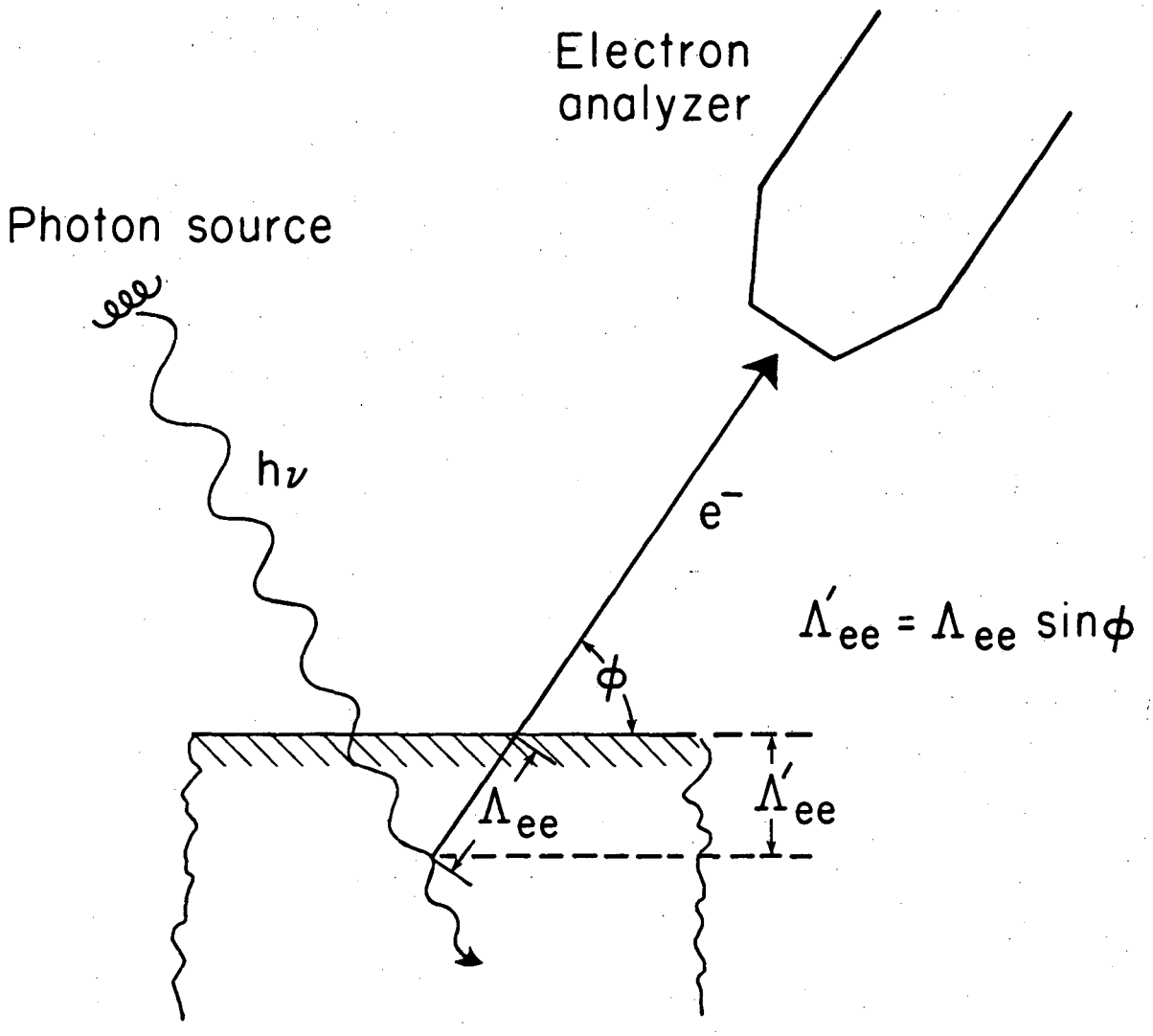
Electron
analyzer
Photon source
hν
e⁻
Λ′ee = Λee sinϕ
ϕ
Λee
Λ′ee
XBL 763-2455

Fig. 2

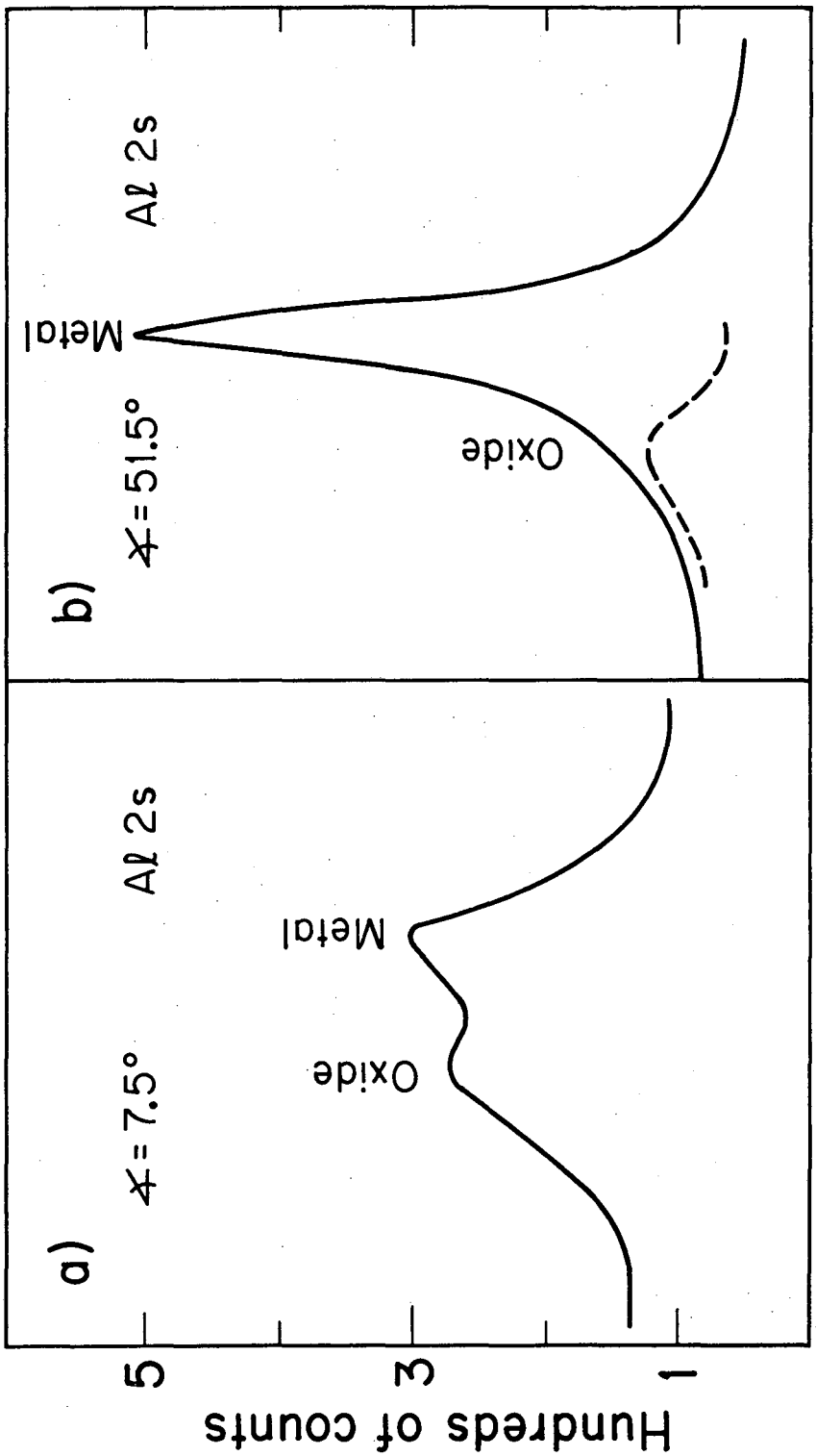

XBL7410-4338

Fig. 3

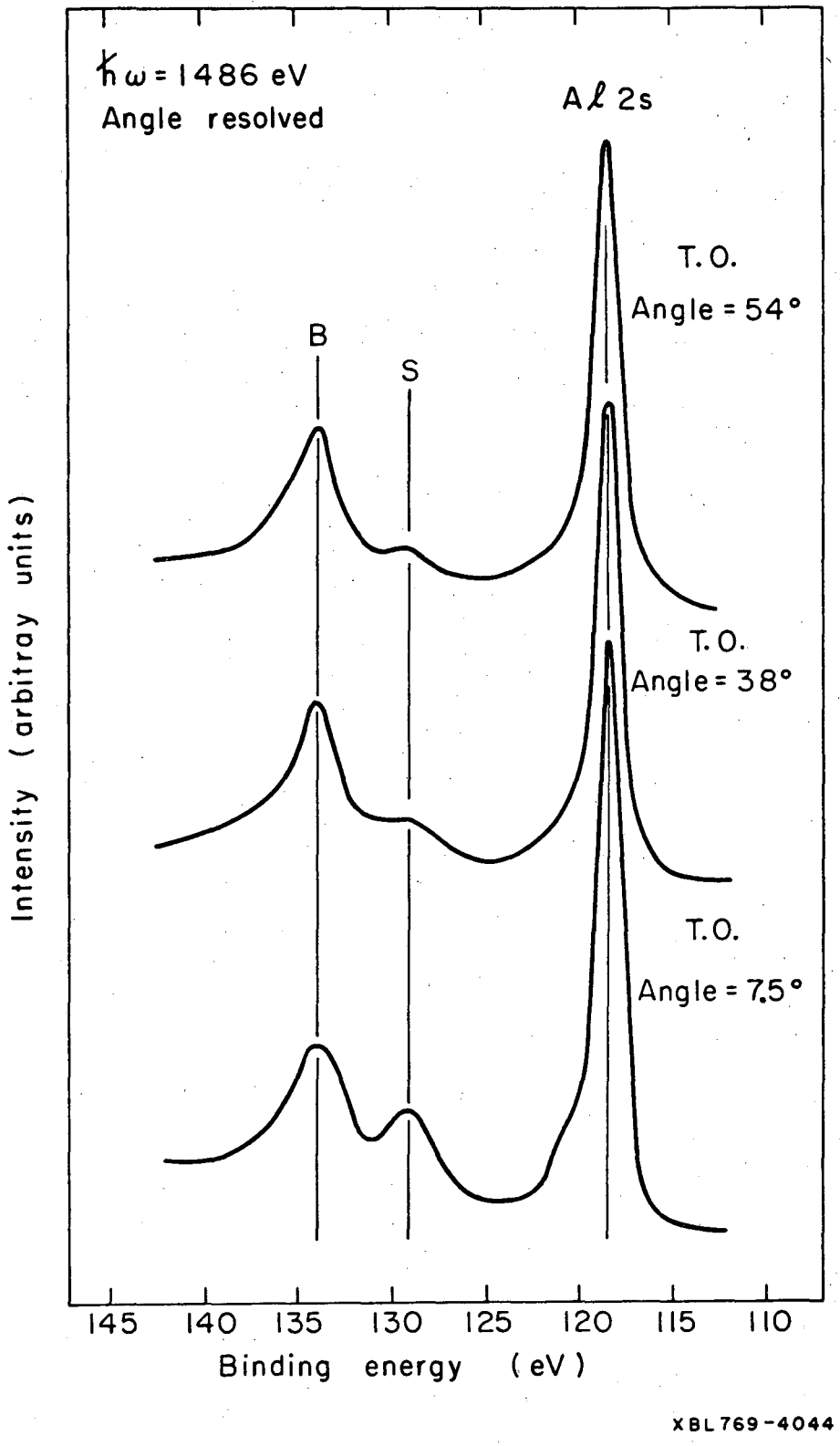
ħω = 1486 eV
Angle resolved
Aℓ 2s
T.O.
Angle = 54°
B
S
T.O.
Angle = 38°
T.O.
Angle = 7.5°
Intensity (arbitray units)
145
140
135
130
125
120
115
110
Binding energy (eV)
XBL769-4044

Fig. 4

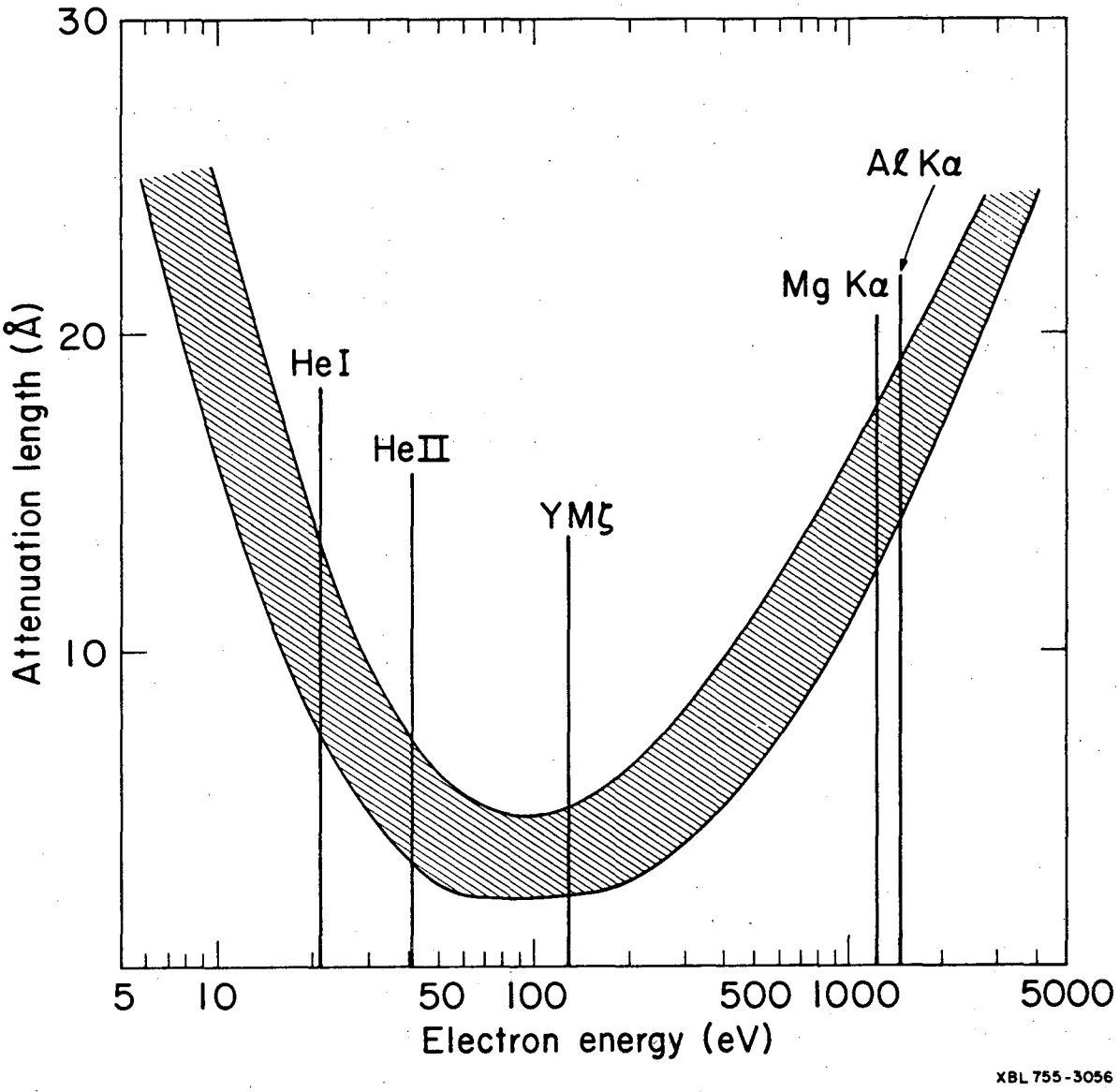
30
20
10
Attenuation length (Å)
HeI
HeII
YMζ
Mg Kα
Aℓ Kα
5
10
50
100
500
1000
5000
Electron energy (eV)
XBL 755-3056

Fig. 5

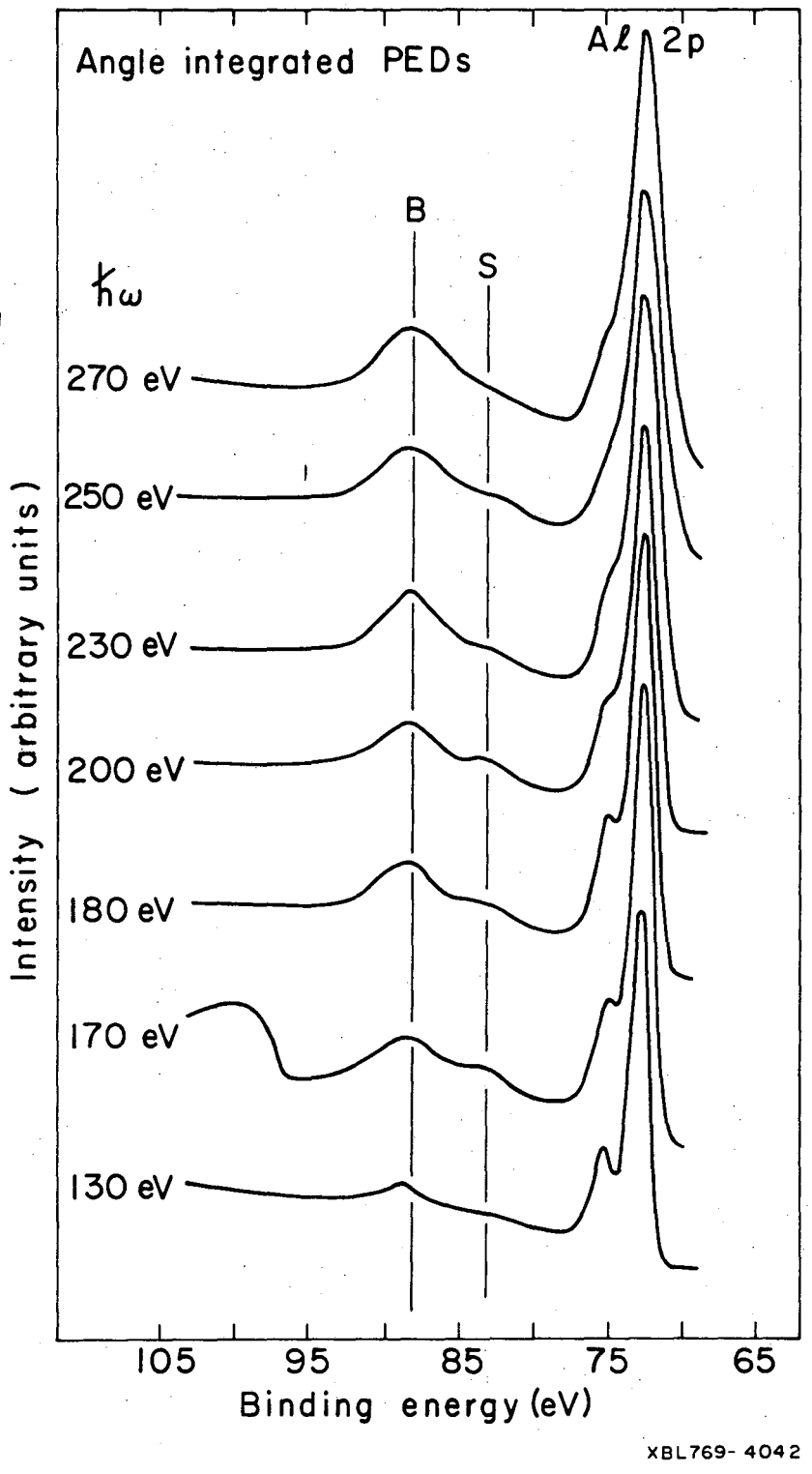
Angle integrated PEDs
Aℓ 2p
B
S
ħω
270 eV
250 eV
230 eV
200 eV
180 eV
170 eV
130 eV
Intensity (arbitrary units)
105
95
85
75
65
Binding energy (eV)
XBL769-4042

Fig. 6

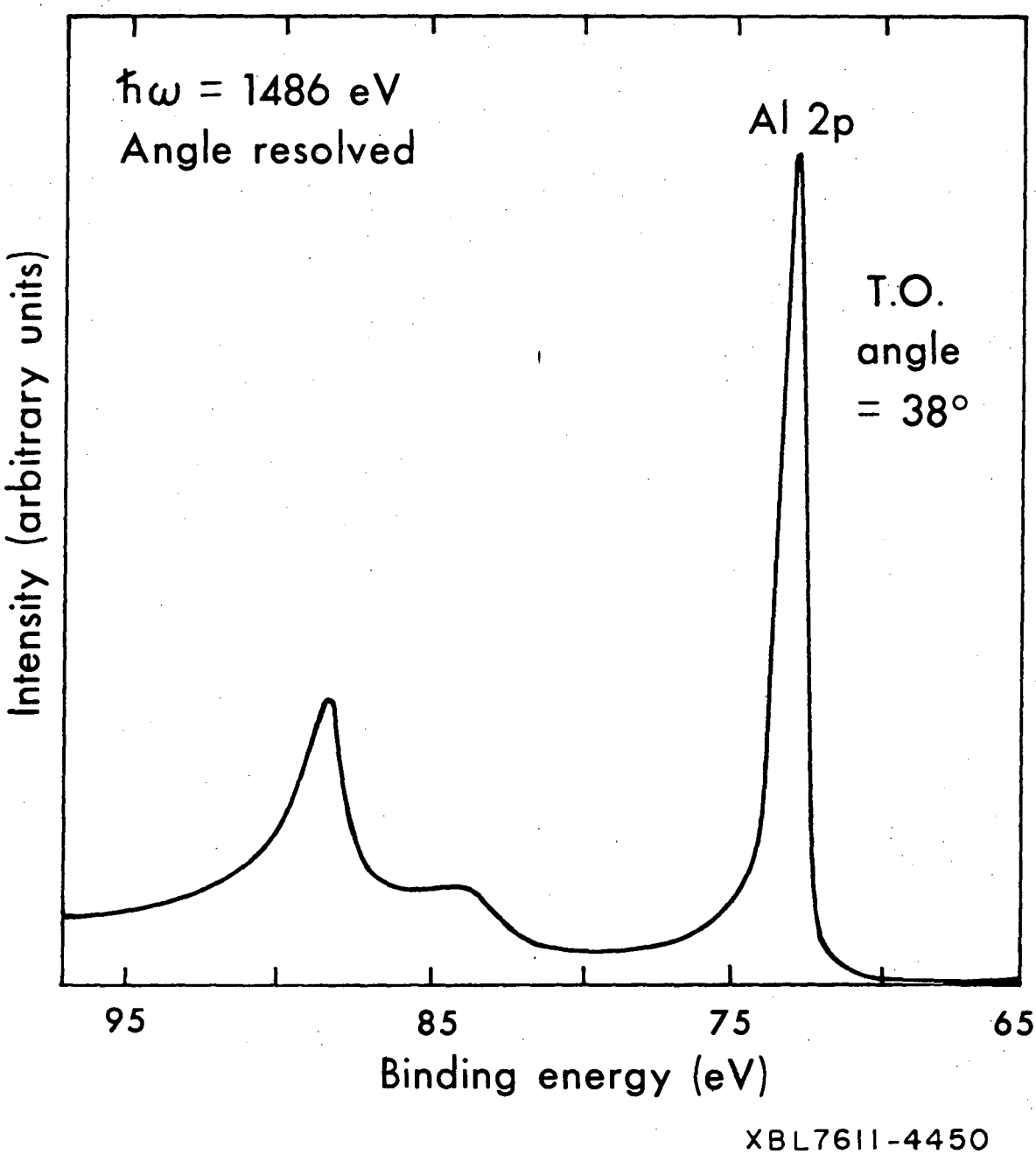
ħω = 1486 eV
Angle resolved
Al 2p
T.O.
angle
= 38°
Intensity (arbitrary units)
95
85
75
65
Binding energy (eV)
XBL7611-4450

Fig. 7

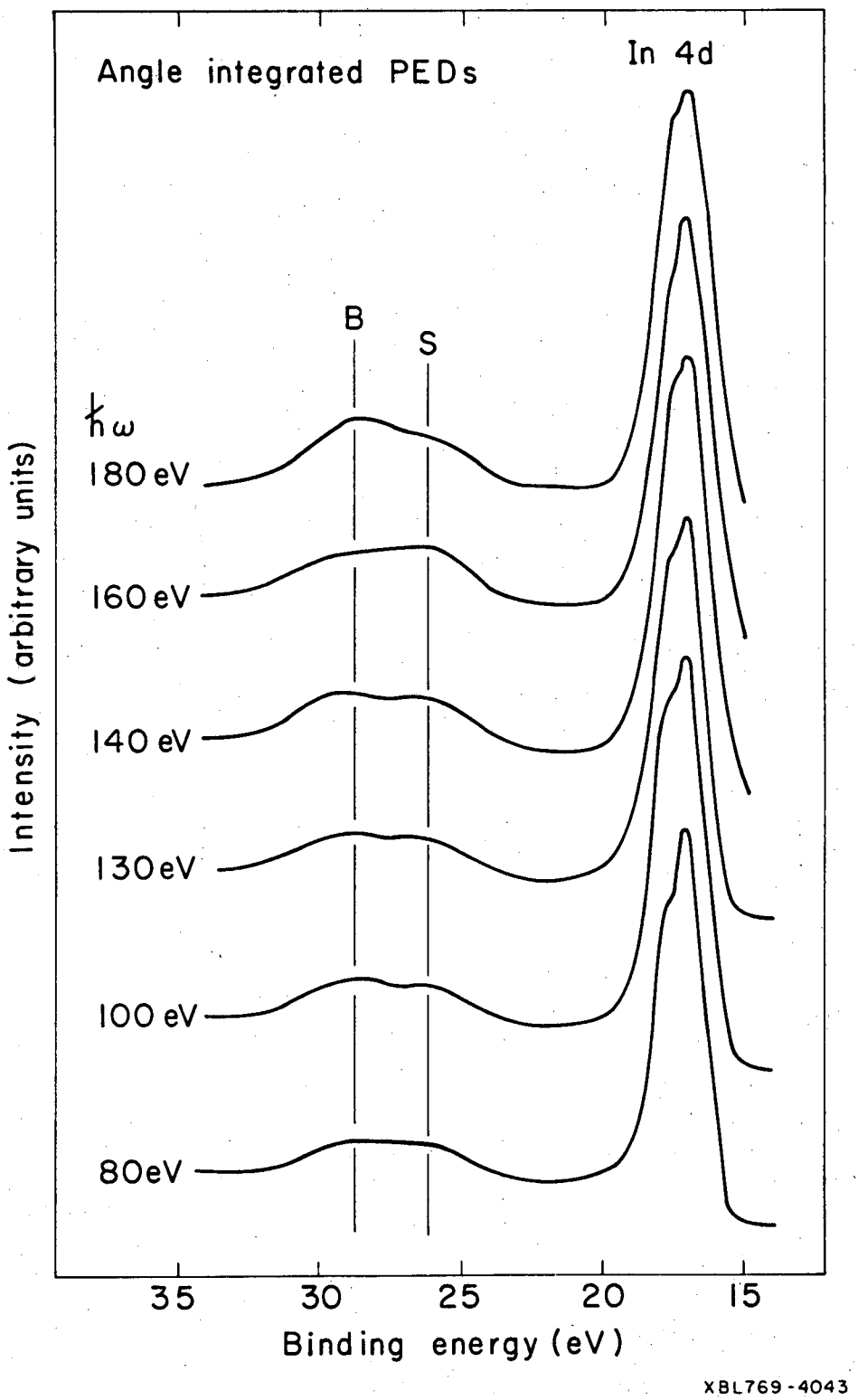
Angle integrated PEDs
In 4d
B
S
ħω
180 eV
160 eV
140 eV
130 eV
100 eV
80eV
Intensity (arbitrary units)
35
30
25
20
15
Binding energy (eV)
XBL769-4043

Fig. 8

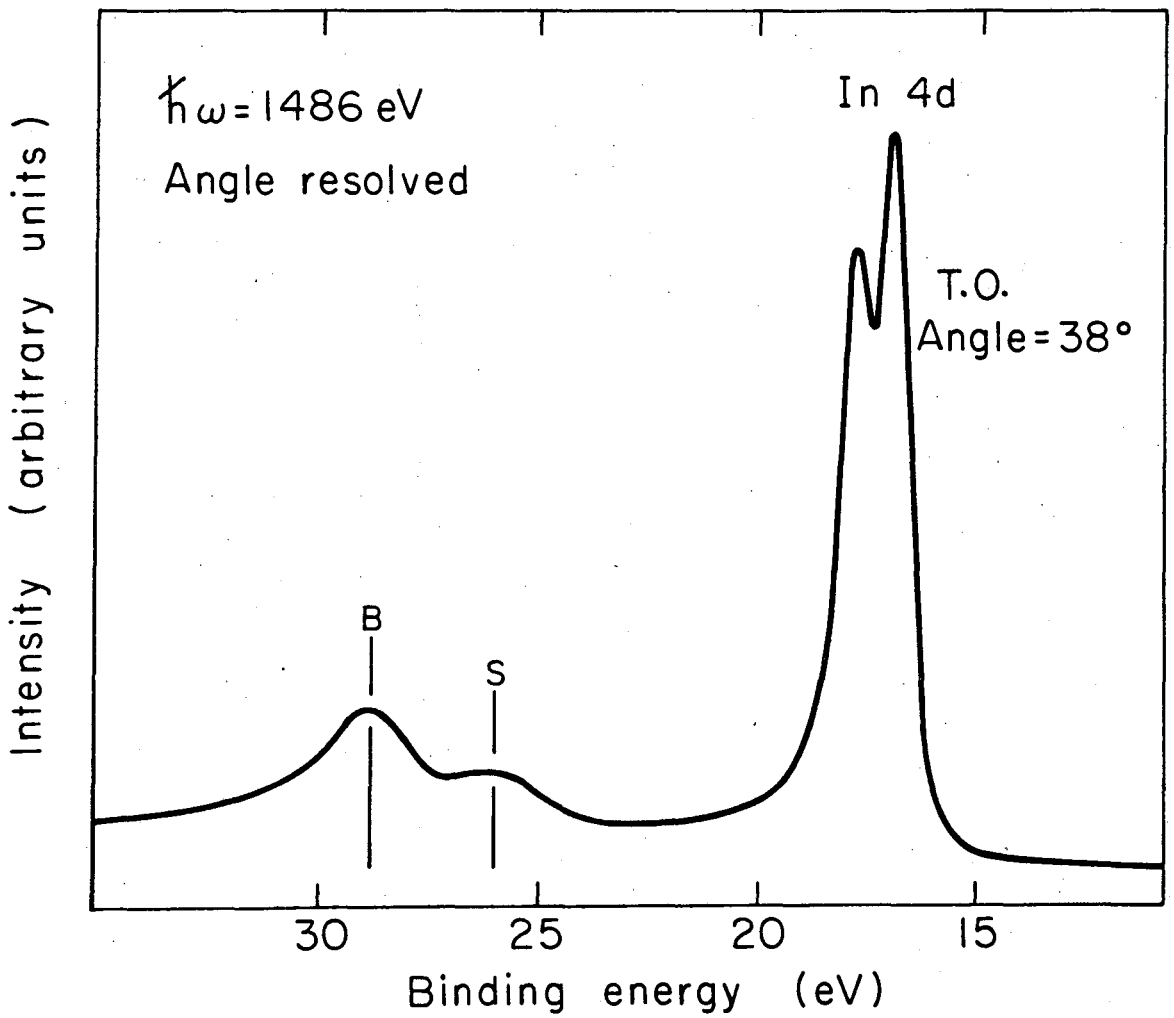

XBL769-4045

Fig. 9

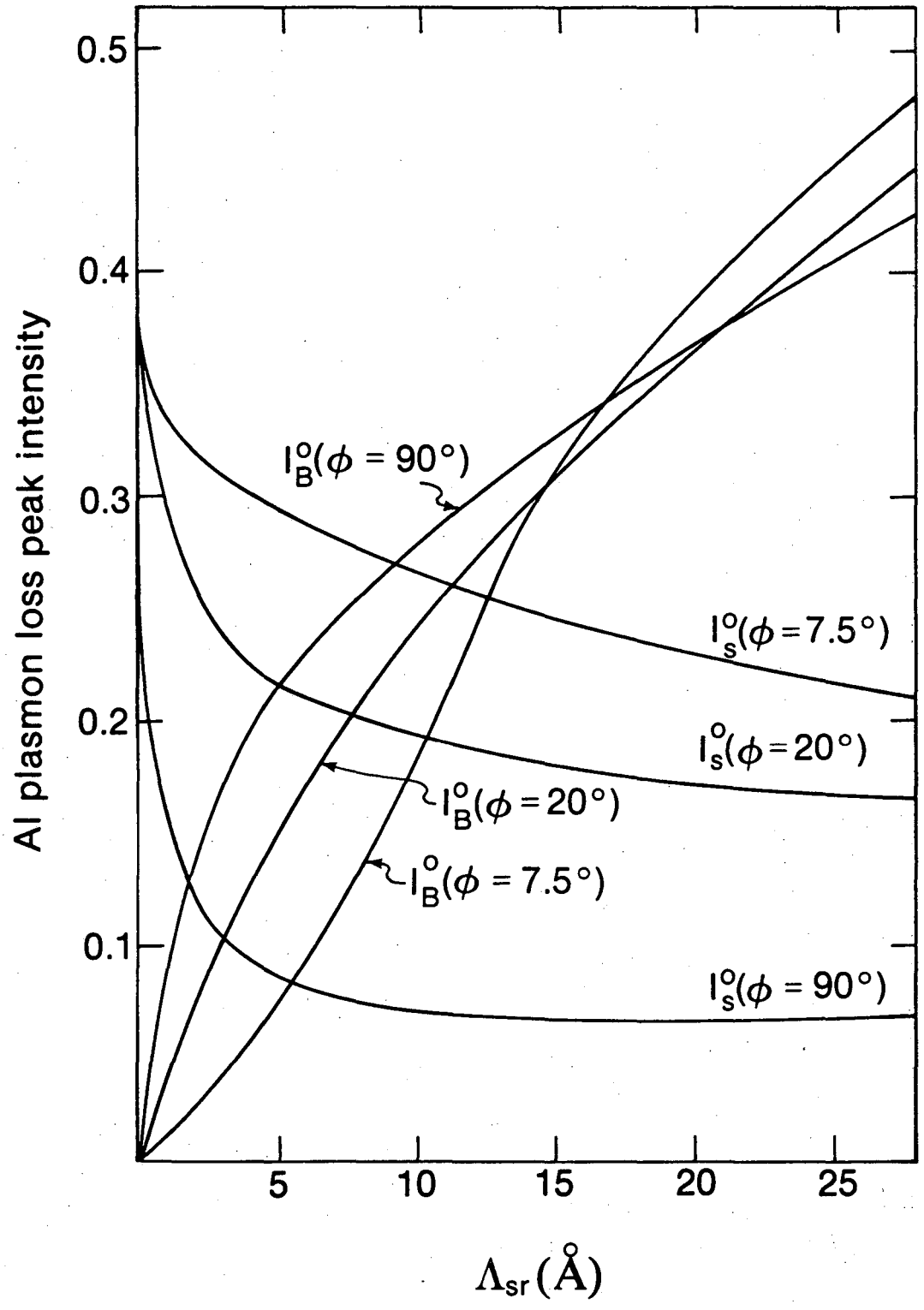

XBL7611-4454

Fig. 10

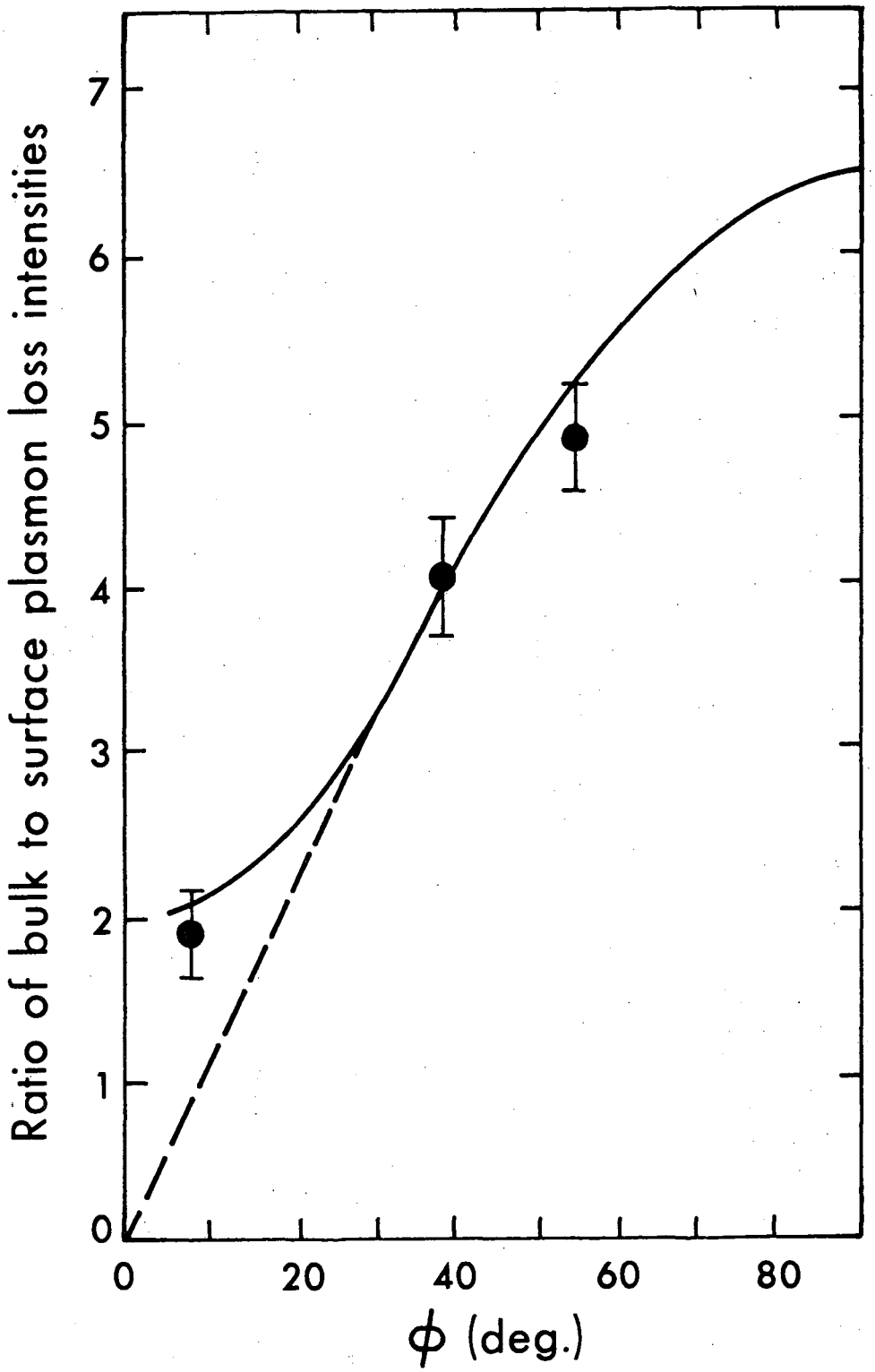
Ratio of bulk to surface plasmon loss intensities
0
1
2
3
4
5
6
7
0
20
40
60
80
φ (deg.)
XBL7611-4452

Fig. 11

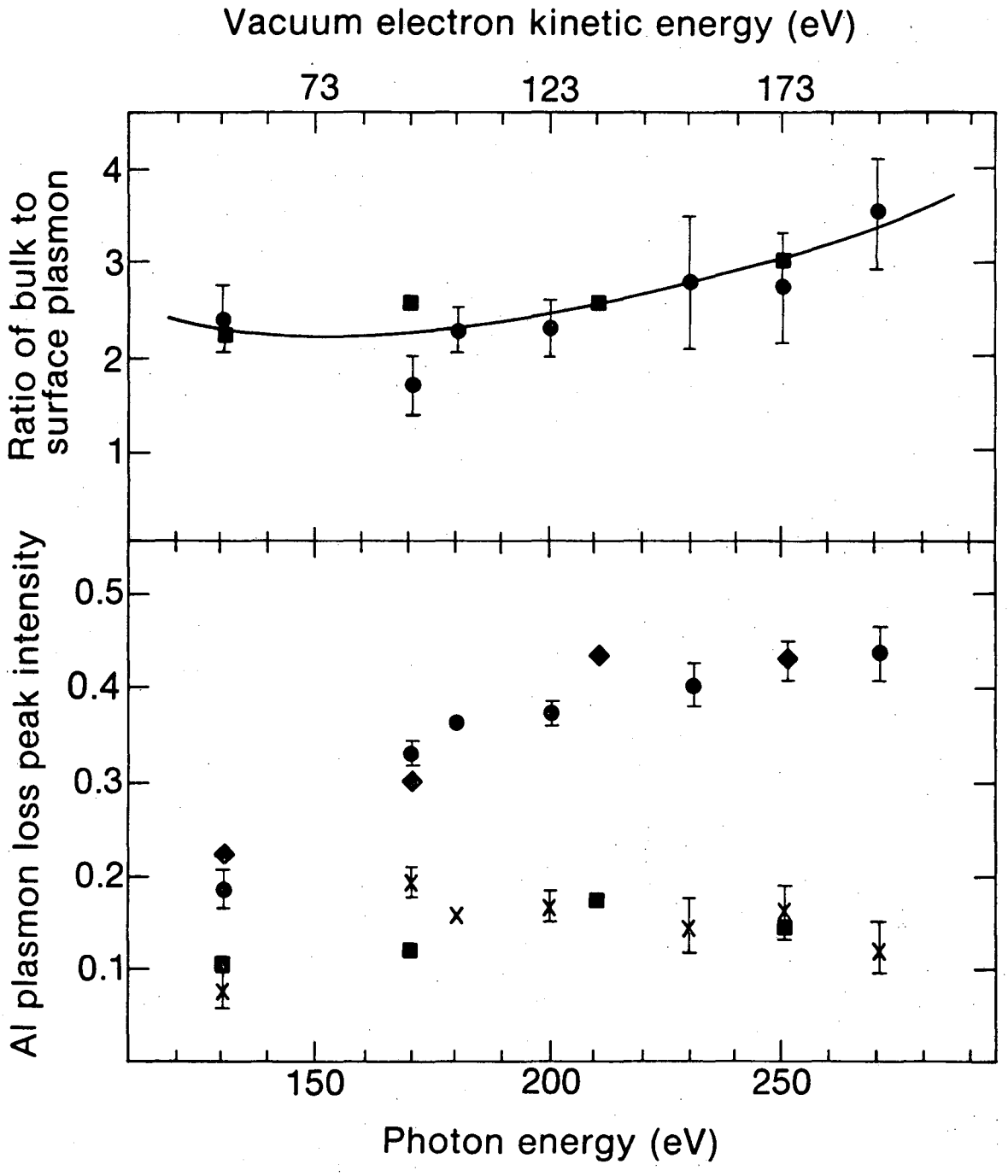
Vacuum electron kinetic energy (eV)
73
123
173
Ratio of bulk to surface plasmon
4
3
2
1
Al plasmon loss peak intensity
0.5
0.4
0.3
0.2
0.1
150
200
250
Photon energy (eV)
XBL7611-4455

Fig. 12

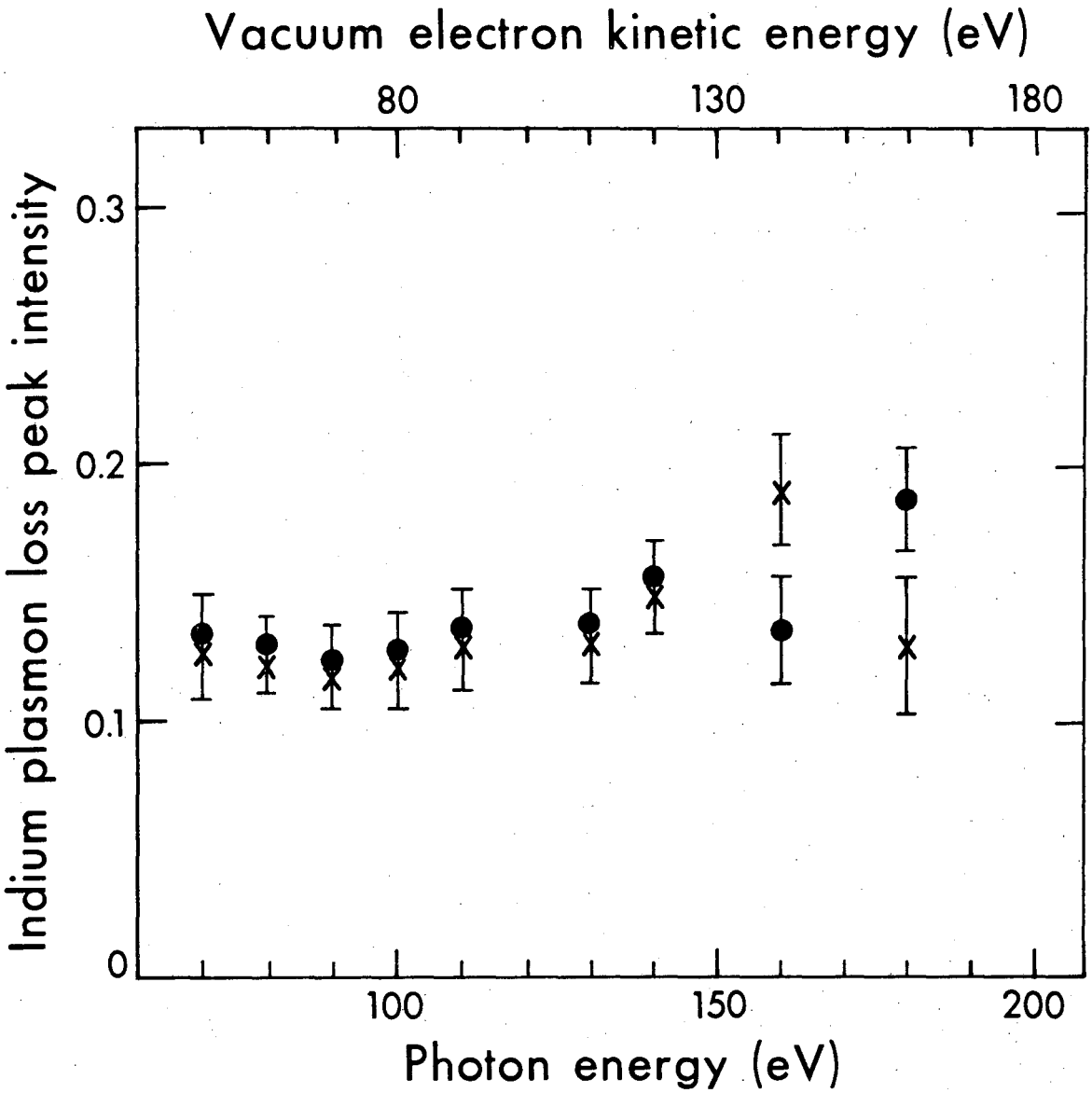

XBL7611-4456

Fig. 13

V. FINAL STATE CRYSTAL MOMENTUM BROADENING

The direct transition model was outlined in chapter III and shown to be generally valid for interpretting ARPES spectra from Cu single crystal faces. The model as presented so far has considered transitions in an infinite crystal lattice; the effects of electron transport to the surface, the interface region itself, and escape of the photoelectron into vacuum on the measured photocurrent have been ignored. However, chapter IV was devoted to the observation of transport effects in photoemission spectra, in particular the existence of a finite inelastic mean free path of hot electrons due to energy loss to plasmon modes and the creation of electron-hole pairs. In this chapter, the Cu ARPES spectra presented earlier will be reexamined to analyze the effect that the solid-vacuum interface and photocurrent damping have on measured photoelectron energy distributions.

A. Electron Transport and Crystal Momentum Broadening

The influence of the surface and inelastic scattering have been considered previously for both LEED[1] and photoemission[2-4] processes. Figure 1 is a representation of a photoemission process which raises an electron from a free electron-like bulk energy band to a continuum state in the crystal. Due to scattering processes, photoelectrons created more deeply within the solid have a smaller probability of reaching the surface, escaping into the vacuum, and being counted by an electron detector. This is the physical basis for the damping of the excited state wavefunction into the solid. Mathematically this damping

arises from an imaginary component of the potential energy, the self-energy term, in the hot electron Hamiltonian.

To see the effect of the self-energy in photoemission, the transition matrix element (Chapter III, Eq. 2) may be evaluated using a damped plane wave for the final state inside the crystal, ie. $|E_f,\vec{k}_f\rangle = \exp(i\vec{k}_f\cdot\vec{r})\exp(\alpha z)$, where the $\hat{z}$ direction is taken to be the outward pointing surface normal. The factor α is most easily related to the photoelectron mean free path ℓ and the angle θ between the momentum vector and $\hat{z}$ by[5]

$$\alpha = \frac{1}{\ell\cos\theta} \quad . \tag{1}$$

Evaluating the transition matrix element in this approximation yields

$$|\langle E_f,\vec{k}_f|\vec{A}\cdot\vec{p}|E_j,\vec{k}_i\rangle|^2 \propto \cos^2\gamma\Phi_j^2(\vec{k}_f)\,|\sum_{\vec{R}}\exp[i(\vec{k}_f-\vec{k}_i)\cdot\vec{R}]\exp(\alpha R_z)|^2 \quad . \tag{2}$$

Since the summation is now only over a half space and each exponential is weighted by a damping term, the strict crystal momentum conservation condition (delta function) is no longer valid. To obtain an idea of how severely the direct transition requirements are violated, the summation in Eq. (2) can be evaluated by considering consecutive layers parallel to the surface. The phase factors are summed within each layer first, then the resulting layer phase factors are summed slab by slab, beginning with the surface, as illustrated by

$$|\langle E_f,\vec{k}_f|\vec{A}\cdot\vec{p}|E_j,\vec{k}_i\rangle|^2 = |\sum_{\vec{a}} \exp[i(\vec{k}_f-\vec{k}_i)\cdot\vec{a}+\alpha a] \sum_{\vec{R}_{\|}^{a}} \exp[i(\vec{k}_f-\vec{k}_i)\cdot\vec{R}_{\|}^{a}]|^2 \quad (3)$$

where $\vec{a}$ is the layer index and $\{\vec{R}_{\|}^{a}\}$ are all the lattice points within the layer $\vec{a}$. The sum over $\vec{R}_{\|}^{a}$ in Eq. (3) yields the condition that the crystal momentum parallel to the surface for a photoemission transition must be conserved modulo a surface parallel reciprocal lattice vector $\vec{G}_{\|}$, in direct analogy with the three dimensional case presented for the infinite solid in Eq. (4) of chapter III.[1,2] The summation over the layer indices may be treated as a sum of a geometrical series and, neglecting cross terms, yields the approximate solution[2,3,6]

$$|\sum_{\vec{a}} \exp[i(\vec{k}_f-\vec{k}_i)\cdot\vec{a}+\alpha a]|^2 \propto \frac{1}{a^2} \frac{1}{\alpha^2+[(\vec{k}_f-\vec{k}_i)_{\perp}-\vec{G}_{\perp}]^2} \quad (4)$$

This Lorentzian constraint, rather than requiring a strict conservation rule for the component of photoelectron momentum normal to the surface $(\vec{k}_f)_{\perp}$ (as a delta function does), allows a finite distribution of momenta about the value of $\vec{G}_{\perp}$ (the surface normal reciprocal lattice vector) that is specified by the vertical transition requirement in an infinite lattice. Thus, the surface perpendicular component of the final state momentum suffers a total broadening $\Delta k_{\perp}$ comparable to 2α, which is the FWHM of the Lorentzian distribution. The momentum constraint approaches a delta function for $a^2\alpha^2 \ll 1$, or in other terms $\vec{k}_{\perp}$ is very nearly a good quantum number (ie. conserved modulo $\vec{G}_{\perp}$) for $\ell\cos\theta \gg 4a$,[6] which is nearly always the case for photoelectrons emitted normal to a Cu surface.

This modified direct transition model explains trends observed in the ARPES spectra of Chap. III quite well. Figure 2 concentrates on spectra collected from 32 to 160 eV photon energy normal to the (110) surface of a copper single crystal. In Chap. III (Fig. 4) the peak positions of these spectra are well correlated by considering direct transitions from Burdick's[7] initial state bands to an empty lattice final state.[8,9] Inspection of the experimental band structure generated by the ARPES spectra reveals that photon energies of 45 eV and 130 eV probe very similar areas of the initial state band structure. Yet the prominent band 6 feature observed at 0.5 eV E_B in the 45 eV spectrum[8] is completely missing from that at 130 eV. This large difference in the photoelectron energy distribution curves is due to the volume of the BZ (number of initial states) sampled at the two different photon (photoelectron) energies.

Momentum broadening due to finite inelastic mean free path effects certainly plays a major part in the form of the spectra studied above. Figure 3 shows a plot of the inelastic mean free path of hot electrons in Cu[10] as a function of electron kinetic energy. From the considerations of Eq. (4) above, $k_\perp$ momentum broadening should be much more severe for the $h\nu$ = 130 eV transition. Since the layer spacing in the [110] direction of Cu is 1.81 Å, the a/ℓ ratio predicted from Fig. 3 for the 45 eV (130 eV) transition is ~0.22 (~0.60), which corresponds to a final state FWHM momentum broadening of ~6% (~20%) of the BZ dimensions. These final state broadenings are represented schematically in Fig. 4. Also represented in this figure is the angular acceptance of the electron

energy analyzer in terms of $\vec{k}_{||}$ projected back into the first BZ. From this projection it is seen that for a fixed angular resolution, the number of initial states sampled increases with increasing photoelectron kinetic energy. The total effect for the two cases considered here is that the volume of the first BZ sampled by the ARPES spectra at 130 eV is roughly twenty times that accessed at 45 eV photon energy.

Some important general considerations arise from this observation. Due to the dispersion of the initial state bands, changes in the momentum space region sampled in ARPES can cause very large changes in the observed photoelectron energy distribution curves. Slight momentum broadenings can cause large spectral energy broadenings. Also, even near the minimum of the inelastic mean free path versus photoelectron kinetic energy curve (where broadening in $k_{\perp}$ is maximized) the momentum broadening for Cu is still small with respect to the BZ dimensions, which shows that a one dimensional density of states model is invalid even for this case. However, even though the broadening is relatively small, it can drastically smear out features in the initial state bands. Thus, the enhancement of surface sensitivity is realized at the cost of broadening of the final momentum states and the resultant loss of initial state specificity. One final point is that the width of features observed in ARPES spectra depends upon both the final momentum state width and the energy dispersion of the initial state bands. Thus, in order to obtain information about inelastic mean free paths from peak widths[3,8] in angle resolved EDC's of valence bands, initial state dispersion information is necessary; in cases where the initial state bands are flat, no such correlation is possible.

B. Band Gap Photoemission

A topic closely related to inelastic collisional damping of photoelectron states is the excitation of electrons into band gaps. In a band gap region the electronic states are not propagating, thus the complex wavevector has a significant imaginary part. Figure 5 illustrates the nature of the wavefunctions involved. Even though the wavefunction is strongly damped inside the crystal, it can couple at the surface to a plane wave state which can carry electron flux away from the crystal.

A simplified physical explanation for this pheomenon is that due to the spacing and orientation of the crystalline planes electrons initially traveling in a certain direction with a specified energy suffer strong elastic scattering (viz. Bragg scattering) into other directions. This short elastic mean free path accounts for the peaks observed in LEED spot intensity versus beam voltage measurements.[1] Conversely, band gap photoelectrons originating inside a solid are very likely to be scattered into a new direction before reaching the crystal surface. However, the possibility of photoelectrons elastically scattering into this direction and consequently escaping into the vacuum is also present.

Band gap photoemission potentially has extreme surface sensitivity, but at the cost of retaining practically no momentum specificity (perhaps a true one dimensional density of states regime).[3,4] Most observations of band gap photoemission[11,12] have been for transitions into the gap between the vacuum level and the bottom of the lowest unbound conduction band for emission normal to several single crystal

faces. Emission directly into these gaps is not yet completely understood. They are usually evident in the low kinetic energy portions of photoelectron EDC's as an attenuation in the "inelastic tail."

However, a rather interesting band gap occurs in the band structure of copper for the [211] momentum space direction in the range 12-16 eV above the Fermi level. Figure 6 shows the Cu energy bands for this direction up to 25 eV above E_F. This figure was derived from an interpolation scheme[13] fit to Burdick's ground state bands, so the precise location and size of the band gap are uncertain. Normal emission ARPES spectra obtained using two different photon polarizations (Chap. III) are compared for several photon energies in Fig. 7. Only the spectra obtained using $h\nu$ = 14 and 16 eV are not interpretable from direct transition theory, and these are the two spectra for which the final states are predicted to fall in the band gap shown in Fig. 6. The spectra at these two photon energies show considerable polarization dependence. Also, they do not appear to be manifesting a one dimensional density of states behavior, although the number of peaks evident and their width suggests considerable final state momentum broadening. The amount of surface layer specific information these spectra contains is potentially high, but at present the nature of this particular surface and final state band are not well enough understood to allow a detailed interpretation. Extending band structure calculations to higher energies and LEED calculations to lower energies to cover this electron energy region so important to photoemission should help greatly in understanding band gap photoemission as well as aid the interpretation of other photoemission results.

REFERENCES

1. J. B. Pendry, Low Energy Electron Diffraction (Academic Press, New York, 1974).

2. G. D. Mahan, Phys. Rev. B2, 4334 (1970).

3. P. J. Feibelman and D. E. Eastman, Phys. Rev. B10, 4932 (1974).

4. B. Feuerbacher and R. F. Willis, J. Phys. C 9, 169 (1976).

5. P. J. Feibelman, Surf. Sci. 46, 558 (1974).

6. D. J. Spanjaard, D. W. Jepsen, and P. M. Marcus, Phys. Rev. B15, 1728 (1977).

7. G. A. Burdick, Phys. Rev. 129, 138 (1963).

8. J. Stöhr, P. S. Wehner, R. S. Williams, G. Apai, D. A. Shirley, Phys. Rev. B17, 587 (1978).

9. D. A. Shirley, J. Stöhr, P. S. Wehner, R. S. Williams, G. Apai, Physica Scripta 16, 398 (1977).

10. I. Lindau and W. E. Spicer, J. Electron Spectrosc. Relat. Phenom. 3, 409 (1974); C. R. Brundle, Surf. Sci. 48, 99 (1975).

11. B. Feuerbacher and N. E. Christensen, Phys. Rev. B10, 2373 (1974); N. E. Christensen and B. Feuerbacher, Phys. Rev. B10, 2349 (1974).

12. D. T. Ling, J. N. Miller, I. Lindau, D. L. Weissman, P. A. Pianetta, and W. E. Spicer, private communication.

13. L. Hodges, H. Ehrenreich and N. D. Lang, Phys. Rev. 152, 505 (1966); N. V. Smith, Phys. Rev. B3, 1862 (1971).

FIGURE CAPTIONS

Fig. 1. A schematic representation of the wavefunctions and energy levels involved in a photoemission transition from a bulk, free-electron-like initial state $|E_j,\vec{k}_i\rangle$ to a damped final state $|E_f,\vec{k}_f\rangle$ which is matched to a free electronic state propagating in the $\hat{z}$ direction outside the solid. The inner potential of the solid is a step function of magnitude V_o, with the step chosen at some distance outside the first atomic layer of the solid. The measured electron kinetic energy E_{kin} is related to the initial state binding energy E_B by the modified Einstein relation $E_B = E_{kin} + \phi - h\nu$, where ϕ is the work function.

Fig. 2. ARPES spectra collected normal to the (110) face of a Cu single crystal for photon energies between 32 and 160 eV.

Fig. 3. Photoelectron mean free path in Cu as a function of kinetic energy obtained from Ref. 9. No data are available for the dashed region of the curve.

Fig. 4. Illustration of the number of initial states sampled in ARPES spectra due to momentum broadening and finite acceptance angle measurements. The top portion of the figure shows the broadening in $k_{||}$ of the final (and initial) states detected as a function of photon energy for a fixed angular acceptance of 24 msterad. (5° half angle cone). Within the extended zone scheme plot of the Cu bands along K-Γ-K (ie. Cu (110) face normal ARPES) are superimposed the final state bands (showing

the FWHM broadening due to inelastic effects) accessed by Photon energies of 45 and 130 eV. The total increase in the initial states sampled at $h\nu$ = 130 eV accounts for most of the differences observed in the ARPES spectra.

Fig. 5. A schematic representation of the wavefunctions and energy levels involved in a photoemission transition from a bulk, free-electron-like initial state $|E_j,\vec{k}_i\rangle$ to a final state $|E_f,\vec{k}_f\rangle$ that lies in a band gap and is thus severely damped.

Fig. 6. The band structure for Cu corresponding to electron momentum in the [211] direction of the crystal extending to 30 eV above E_F. The bands were generated by an interpolation scheme fit to Burdick's bands, and illustrate the band gap in the final states sampled in photoemission for electron energies 10-13 eV above E_F.

Fig. 7. Comparison of normal emission ARPES spectra collected from a Cu (211) crystal face for two different polarizations (inset). The spectra collected at photon energies of 14 and 16 eV are those for which emission from the Cu d-bands should fall in the final-state band gap. The spectra at these photon energies display considerable polarization dependence, but do not appear to be related to the initial state band structure in any simple manner as all the other spectra collected from this face do.

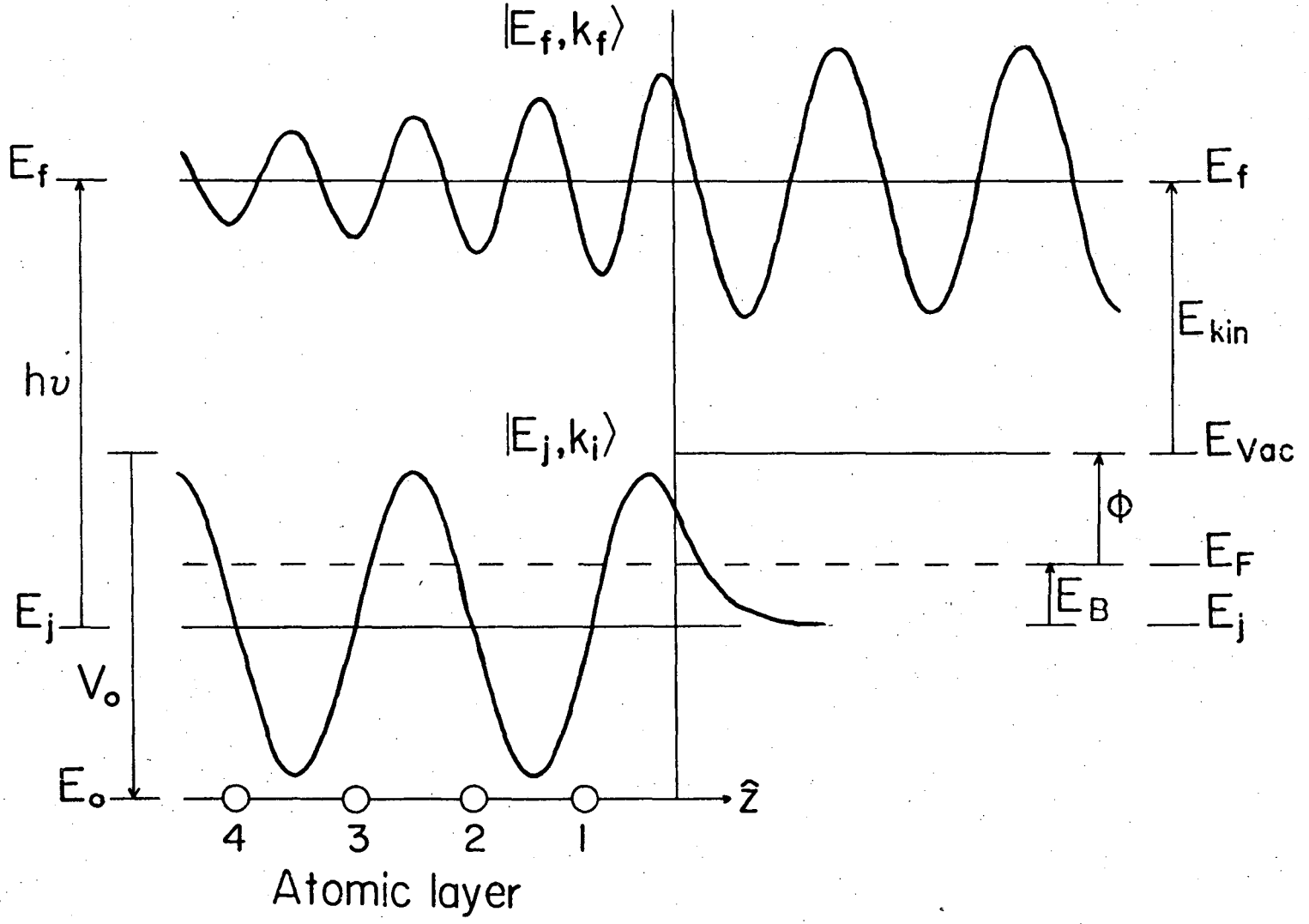

XBL 785-8772

Fig. 1

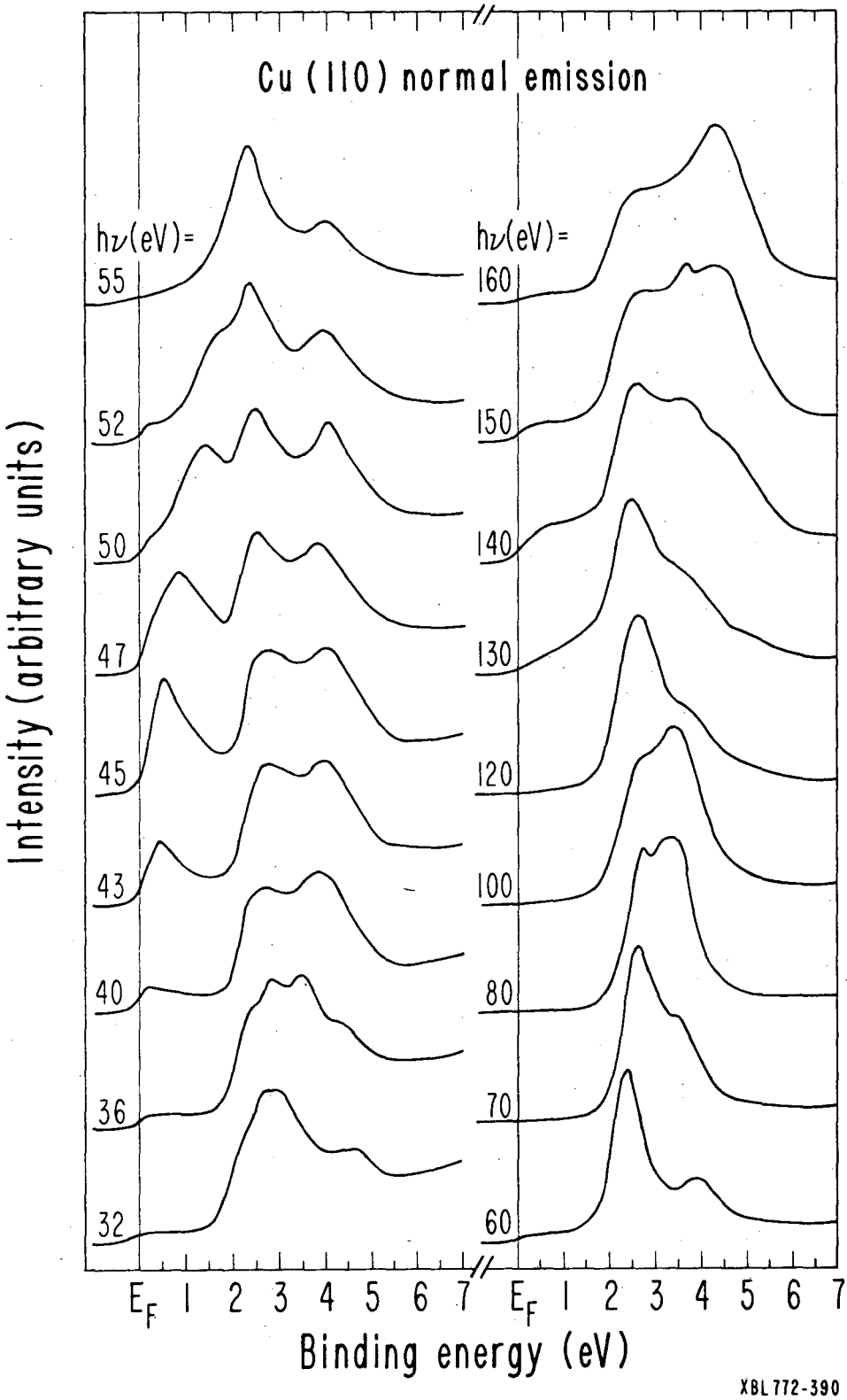
Cu (110) normal emission
hν(eV)=
55
52
50
47
45
43
40
36
32
hν(eV)=
160
150
140
130
120
100
80
70
60
Intensity (arbitrary units)
E_F 1 2 3 4 5 6 7
E_F 1 2 3 4 5 6 7
Binding energy (eV)
XBL 772-390

Fig. 2

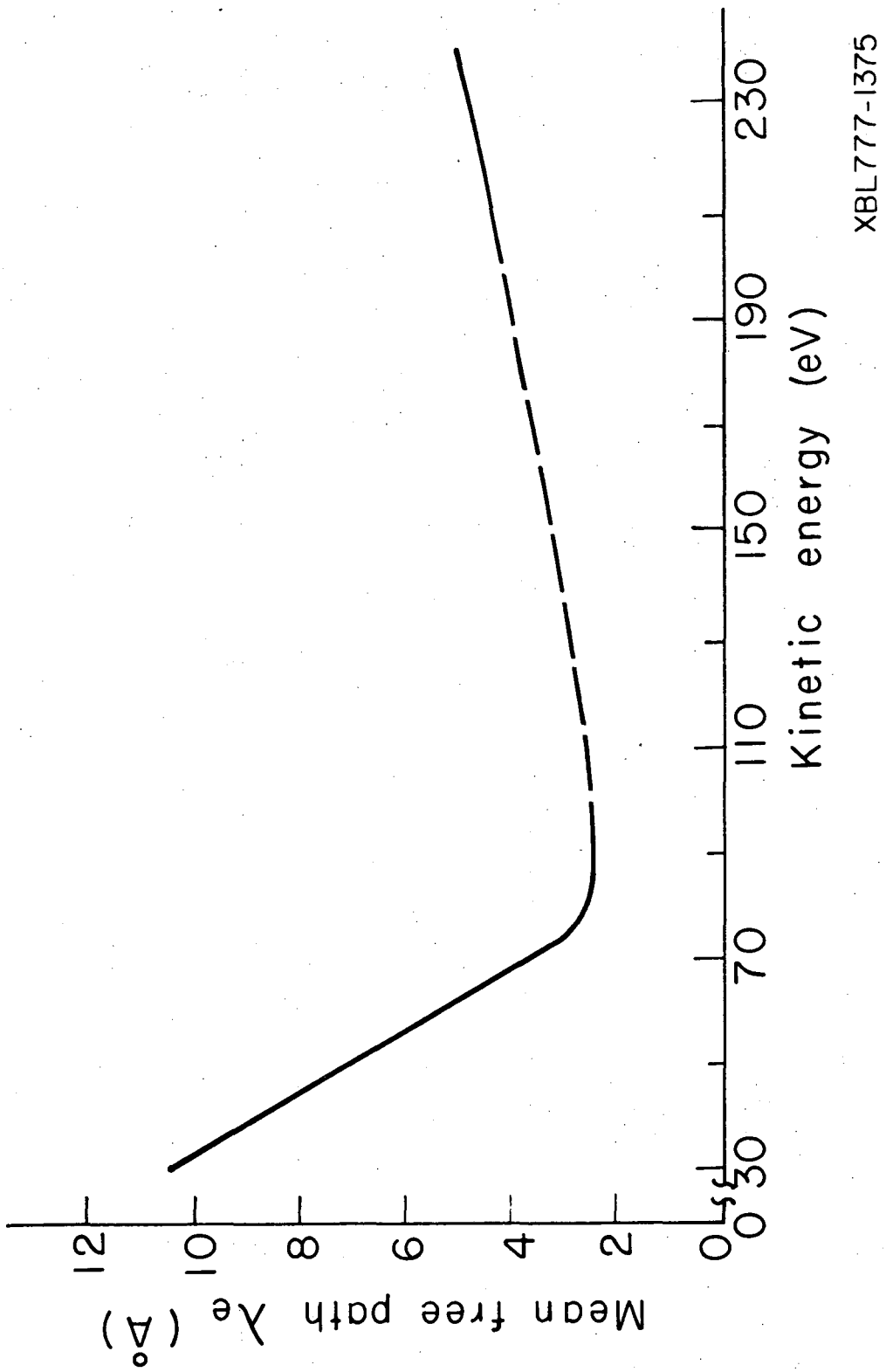
Mean free path λ_e (Å)
0
2
4
6
8
10
12
30
70
110
150
190
230
Kinetic energy (eV)
XBL777-1375

Fig. 3

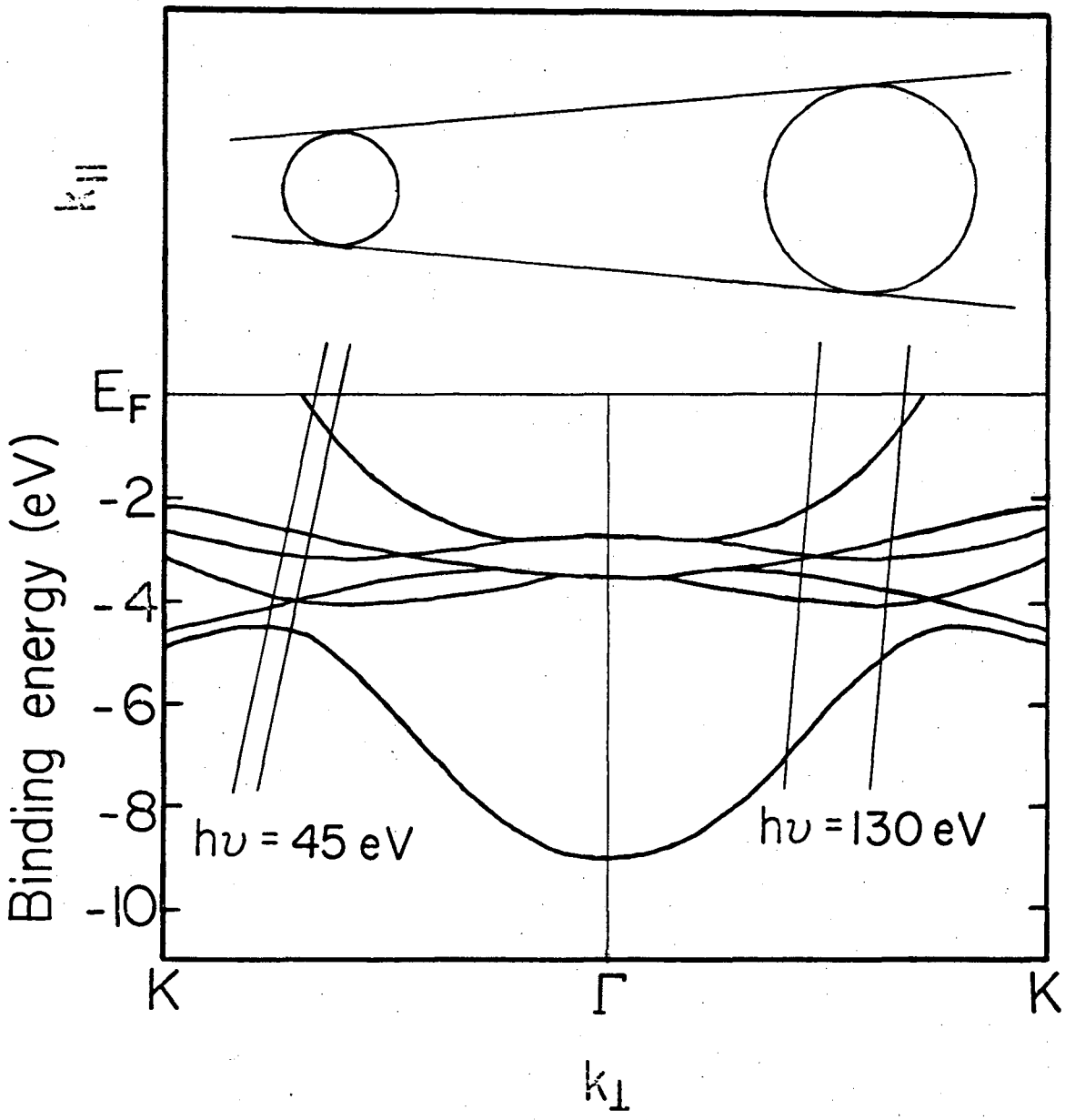

XBL 785-8693

Fig. 4

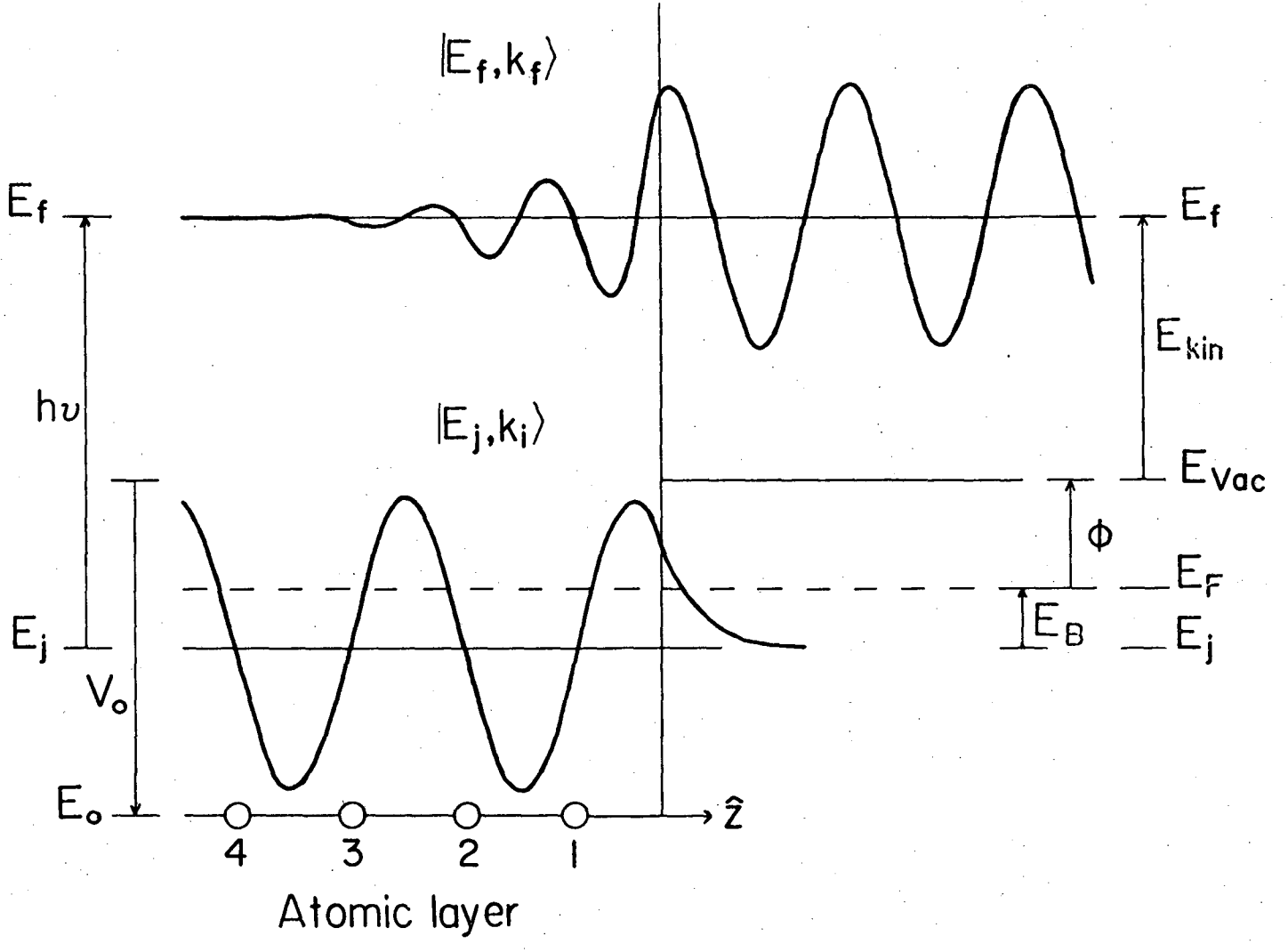

XBL 785-8774

Fig. 5

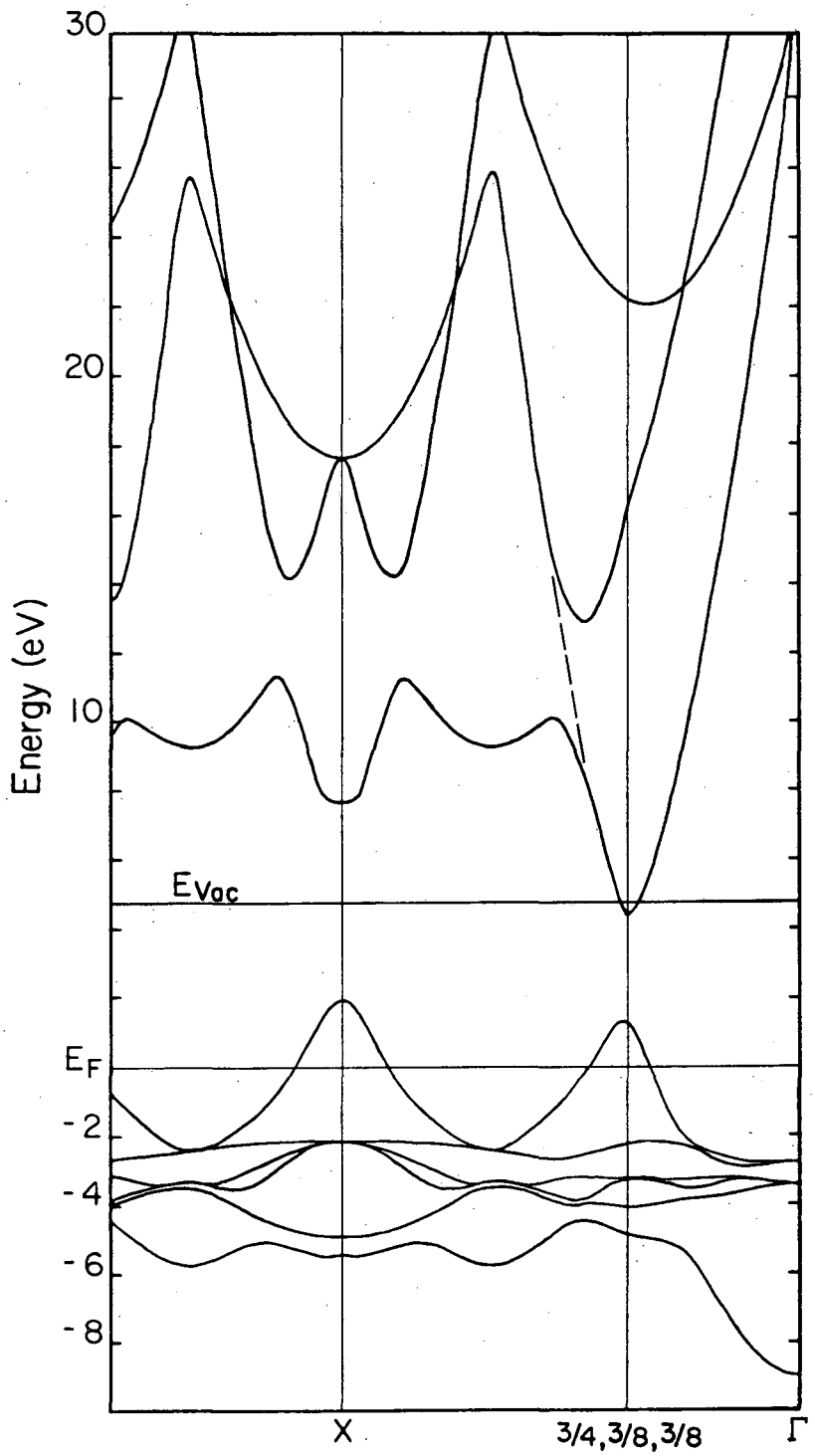

XBL 785-8814

Fig. 6

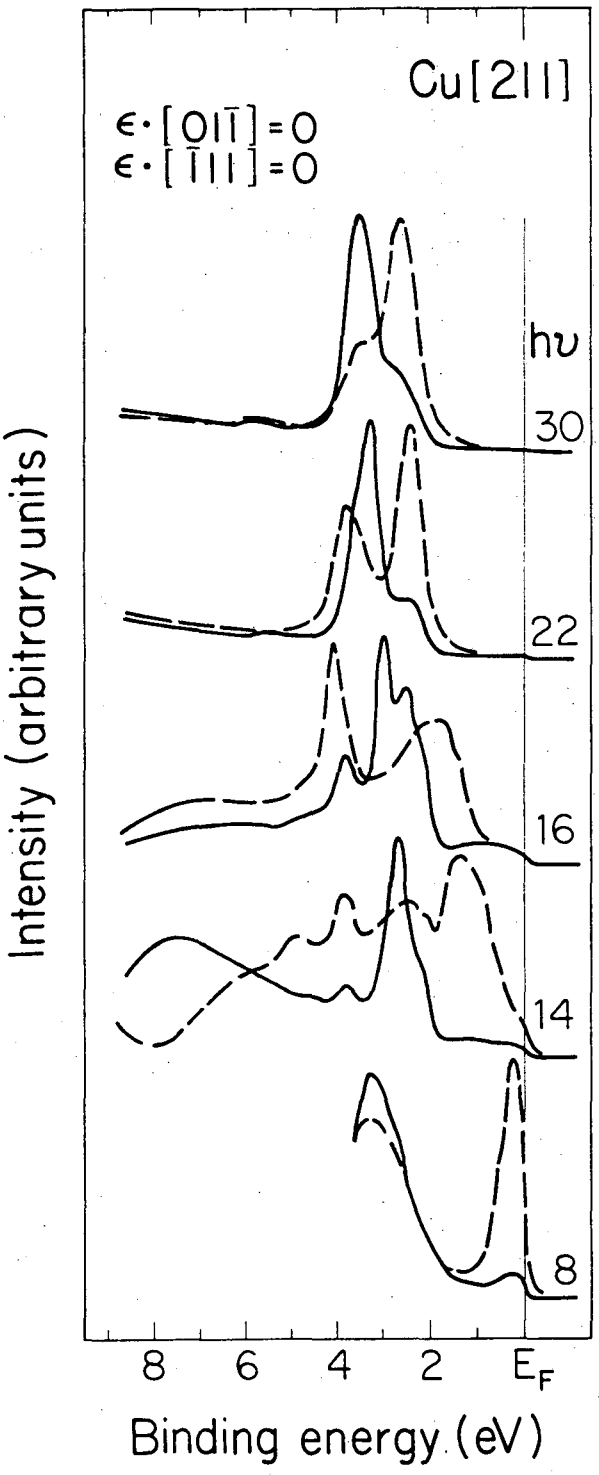

XBL 784-471

Fig. 7

VI. THE SOLID-VACUUM INTERFACE*

This chapter is concerned with the influence of the solid-vacuum interface on ARPES spectra obtained from Cu single crystals. In particular, the first direct measurement of the refraction of a photoelectron as it crosses the solid-vacuum interface is presented. It is also shown that copper exhibits a small amount of surface photoemission, relative to direct transition processes, for large angles of incidence of p-polarized light. Finally, the utilization off-normal photoemission orientations is shown to be a useful technique to suppress surface contributions to ARP spectra, allowing bulk direct transition features to be more clearly resolved.

For this study, the "band six" peak which has been observed for $h\nu$ = 45 eV in normal photoemission from Cu(110) was chosen. As discussed previously, this resonance arises from a direct transition involving the VB closest to the Fermi level (E_F) at k = (-0.5, -0.5, 0), in units of $2\pi/a$ (where a is the lattice constant of Cu), as shown in Fig. 1. Photoelectrons created by this transition travel along the [110] direction inside the crystal and thus provide a sensitive indicator for directional effects in ARP.

A. Experimental

The experiment was performed utilizing the variable photon energy source available at the 4° port of Beam Line I at the Stanford Synchrotron Radiation Laboratory (SSRL).[1] The experimental chamber and sample

preparation have been described in detail elsewhere.[2] Variation of the polar photoelectron emission angle θ (measured with respect to the surface normal) was achieved by rotating the crystal about an axis (hereafter called the crystal-rocking axis) perpendicular to the Poynting vector $\vec{S}$ of the source light and to the axis of the photoelectron detection cone defined by the final-state momentum $\vec{k}_f$ (for a fixed angle between $\vec{S}$ and $\vec{k}_f$).

Two different orientations of the crystal-rocking axis with respect to the polarization direction $\vec{\mu}_o$ (for $\vec{\mu}(t) = \vec{\mu}_o \cos(\omega t)$) of the light were investigated. In the first mode (utilized in previous studies of ARP from Cu surfaces)[2] the radiation was p-polarized with $\vec{\mu}$ in the plane containing $\vec{S}$ and $\vec{k}_f$, at an angle of 27.3° from $\vec{k}_f$. In the second mode, $\vec{\mu}_o$ was parallel to the crystal-rocking axis, with $\vec{k}_f$ 132° from $\vec{S}$. Thus, the incident light was s-polarized with respect to the sample surface, and $(\vec{k}_f \cdot \vec{\mu}_o)$ for all choices of θ was equal to zero. This second configuration yielded no useful spectra, as discussed in Section IV.

The samples were single crystals of Cu cut along the (100), (110), and (111) planes. Sample preparation included azimuthal orientation of the crystal on the sample holder. The crystals were mounted on a PHI model 10-504 precision manipulator with which the relative sample positions could be measured to within ±0.5°. The absolute orientations of the crystal on the manipulator were checked using Laue back-reflection photography and found to be within ±2° for all axis. Short cycles of Ar^+ bombardment and annealing with an electron gun produced crystal

surfaces free of detectable contaminants, as determined by in situ chemical analysis (photoemission spectra taken at different photon energies to enhance possible contaminant peaks with respect to the Cu substrate). Contaminants remained undetectable for the c.a. 10 hour duration of the experiments, which were performed at pressures less than 5×10^{-10} Torr. Spectra taken at the beginning and end of each run were essentially identical.

Spectra collected in the first crystal-rocking geometry discussed above are shown in Figs. 2-5. Each figure displays VB spectra as a function of θ near the [110] axis for four different crystal orientations, shown in the inset of each figure. Common to all figures is the trend observed for the band six resonance. This feature exhibits extreme angular sensitivity; it appears with appreciable intensity only for $\vec{k}_f$ within $\pm 10^\circ$ of the [110] axis in Figs. 3 and 5.

The most interesting information, however, is contained in the striking differences observed in the corresponding spectra of the different figures. Comparing the spectra for equivalent crystal-rocking axis orientation with respect to the crystalline axes (i.e., Figs. 2 and 4 with Figs. 3 and 5, respectively) reveals that the band six peak does not appear along the external projection of the [110] axis for off-normal photoemission (Figs. 2 and 4), but is shifted significantly toward the sample surface. Further differences among these spectra are noted in the "d-band" region; spectra with similar band six intensities exhibit features at equivalent binding energies, but the relative intensities of the features often differ drastically. An important difference

between spectra with similar crystalline orientations is that the peaks observed in off-normal photoemission are generally sharper and more pronounced than their near-normal emission (Figs. 3 and 5) counterparts.

Large differences are also observed between the corresponding spectra of Figs. 3 and 5, for which the azimuthal crystal orientation differed by 90°. The relative height of the band six peak with respect to the main d-bands is different for the two orientations. Equally remarkable is the valence region just above the peak at 2.5 eV E_B; the spectra of Fig. 5 exhibit a strong peak between 3 and 4 eV E_B for $\theta = 0°$, whereas those of Fig. 3 reveal only a weak shoulder. Also, the spectra within each figure do not display symmetry about the [110] axis.

Finally, an important experimental observation arose from the second crystal-rocking axis orientation described in Chapter III.B. In this geometry, the photoemission intensity was c.a. two orders of magnitude lower than in the first mode in the photon energy range available (40-200 eV). Unfortunately, such low intensity precluded collecting useful spectra in the amount of beam time available, even in the region of maximum transmission of the monochromator (150 eV).[1]

B. Influence of the Surface in Photoemission

1. Initial states sampled

According to the theories outlined earlier, the constraints of energy and momentum conservation greatly restricts the portion of the initial states in the Brillouin Zone (BZ) sampled in ARP.[1,3] For normal emission measurements, the region of $\vec{k}$-space sampled may be approximated

by a cylinder of radius $|\Delta k_{\parallel}|$, determined by the finite angular resolution of the analyzer, and height $|\Delta k_{\perp}|$, the consequence of momentum broadening in the final state due to the short inelastic mean-free-path of the photoelectron in the solid.[4,5] In terms of the spectra taken in normal emission geometries, the $\vec{k}$-space cylinder sampled had a radius of 0.19 (5° half-angle aperture) and a height of 0.07 (8 Å mean free path)[2] in units of $2\pi/a$, for a total volume of 0.2% that of the BZ. We note that in this case $k_{\perp}$ is nearly conserved.[4]

The sampling cylinder becomes distorted for off-normal photoemission geometries. This distortion, however, is small for all the spectra reported here and does not significantly alter the shape of the $\vec{k}$-space sampling region. Observation of equivalent symmetry directions for different emission angles is also complicated by different evolution of the sampling volume through $\vec{k}$-space with the energy of the final state, but again this effect is small for the orientations reported here. Although refraction of the radiation at the metal surface can be appreciable (2°-6° for our geometries), the photon momentum $\vec{k}_{h\nu}$ for $h\nu = 45$ eV is so small that this has a negligible effect on the momentum selection rules. Thus, to a good approximation, the only effect of varying θ is to change the portion of the initial state BZ sampled. Observation of ARP spectra in equivalent crystalline orientations (corrected for refraction outside the crystal) should differ only due to surface effects.

2. Electron refraction

One of the most important surface effects and the least studied experimentally is the refraction of the escaping photoelectron as it transverses the potential barrier at the surface. This particular effect has received some theoretical consideration,[6] but has been deemed to be unimportant experimentally for electrons with kinetic energy greater than about 20 eV.[5] This subchapter considers this effect and the information that the above data provides concerning it.

The conservation laws determining the behavior of an off-normal photoemitted electron as it transverses the solid-vacuum interface enroute to the analyzer have been discussed in detail by Mahan.[6] If $\vec{q}$ is the wavevector of the photoelectron inside the crystal, it is related to the free electron wavevector $\vec{p}$ outside the crystal by the following relationships:

$$\vec{p}_{\parallel} = q_{\parallel} \tag{1}$$

$$\hbar^2/2m^* \left(|p_{\perp}|^2 - |q_{\perp}|^2\right) = E\left(m/m^* - 1\right) - V_o . \tag{2}$$

Here $p_{\perp}$ and $q_{\perp}$ are the surface normal components of $\vec{p}$ and $\vec{q}$, while $\vec{p}_{\parallel}$ and $\vec{q}_{\parallel}$ are the parallel components. V_o denotes the inner potential; the energy difference between the zero of energy inside the crystal and the vacuum level. As seen from Eq. (2), electron refraction in this simple model depends on both the ratio of the effective mass of the electron (m*) inside the crystal to that outside (m-the free electron value) and the magnitude of the inner potential. The angle θ between the emerging photoelectron and the surface normal $\vec{n}$ becomes

$$\theta = \arcsin[(m^*(E + V_o)/mE)^{1/2}\sin\theta'], \qquad (3)$$

where θ' is the angle between the photoelectron and $\vec{n}$ inside the crystal and E is the measured kinetic energy of the detected photoelectron. The validity of Eq. (4) in photoemission has been assumed in the past for $m^* = m$. To the best of our knowledge, however, no previous experimental test of the relation between θ and θ' exits. It is easy to understand why, however. In order to know θ' accurately, a distinctive ARP feature in the bulk photoemission spectrum (that is a feature narrowly restricted in angle) is necessary. The band six resonance provides such a feature and was discovered only recently.[7]

The inner potential V_o is usually taken as the sum of the work function for the particular surface in question and the separation between the zero of energy for the free electron bands and the Fermi level (8.9 eV in copper), which yields a V_o of ~ 13.8 eV. We may thus predict the surface refraction for photoelectrons with a particular $\vec{k}_f$ inside the sample. In particular, for electrons originating from the band six peak in copper in the [110] direction at 45 eV (using V_o = 13.8 eV and $m^* = m$) Eq. (1) predicts refraction angles ($\theta - \theta'$) of 10° and 7° for photoemission from (100) and (111) surfaces, respectively.

Inspection of Fig. 6 (parts a and c) indicates that the observed refraction angles are both ~5° larger than predicted above, a difference considerably greater than the estimated 2° uncertainty associated with the measurements. Using the measured values of θ to determine V_o from Eq. (4) ($m^* = m$) yields an inner potential of 18-20 eV. However, the inner potential for hot electrons should be less than that for valence

electrons, due to the decrease in magnitude of the exchange-correlation potential[8] with increasing electron energy. Thus, another effect must be important in determining electron refraction. To ascertain if the calculated electron refraction is sensitive to the form of the potential, as noted by Gartland and Slagsvold[9] for 5 eV photoelectrons, the step potential was replaced by a softer potential of the form $V(z) = a/(c+z)$, where a and c are constants and $z > 0$ measures the distance of the photoelectron from the surface, to account roughly for the image charge induced in the metal by the photoelectron.[10,11] The recalculated refraction angles as functions of the parameters a and c revealed that for a final state electron energy of 40 eV, there is no significant difference in refraction angle caused by the two potentials (i.e., $\Delta\theta < .2^\circ$).

If the position is taken that V_o is fixed at near 14 eV for copper (this is certainly an upper limit for hot electrons), two possible causes remain for the unexpectedly large refraction angles. Since $\hbar^2k^2/2m$ is effectively a measured quantity, and V_o is taken to be fixed, the data can be fit by Eqs. (2) and (3) only by increasing m*. An effective mass of $m^* = 1.15$ m (and $V_o = 13.8$ eV) yields $\theta = 45.5^\circ$ and 61.7° for the (111) and (100) faces, respectively. That m* may assume a value other than the free electron value for the final atate photoelectron is shown to be plausible in Fig. 1. The nominally observed final state for $\vec{q} = (-0.5, -0.5, 0)$ and $\vec{G} = (2, 2, o)$ is degenerate with another band of the same symmetry (Σ_1) arising from G = (0, 0, 2). The perturbation of the levels should be small, as they mix through a Fourier potential component U_G for G = (2, 2, 2). However, the interaction may be large enough to affect the hot electron group velocity,

i.e., induce an effective mass different from the free electron value. Furthermore, Moruzzi, et al. find that a value of $m^* = 1.08\ m$ for hot electrons 20 eV above the Fermi level allows a good fit of their calculated Cu band structure to photoemission data.[12]

The other possible cause of large refraction angles is surface roughness. It is not clear, however, exactly how surface roughness would affect the observed values of θ. In fact the effects on θ for all the geometries studied in this work are expected to be model-dependent and quite small for plausible models.[13] It seems very unlikely that an increase in θ by as much as 5° could arise from surface roughness. A more probable result of surface roughness is a spread in θ, and in this connection, it is noted that the band six resonance persists over a larger range of angles for the off-normal geometries than would be expected from the normal-geometry photoemission experiments on the (110) face.

3. Light polarization effects

In addition to the conservation laws discussed above, photoelectron transitions must satisfy dipole selection rules. For ARPES from single crystals, the location of the analyzer specifies the symmetry of the final states detected. Specifically, for emission in the [110] direction the axis of the sampling cylinder will coincide with the Γ - K - X line in $\vec{k}$-space, and the final state must have Σ_1 symmetry.[14] The selection rules governing transitions into the final Σ_1 state are that, for components of the light polarization vector $\vec{\mu}_o$ parallel to the [110], [100], and $[1\bar{1}0]$ axes, emission will be allowed from Σ_1, Σ_3, Σ_4 initial states, respectively.[14] Due to the dipole nature of the

excitation process, Σ_2 bands should not be seen. For all the spectra in Figs. 2-5 there is a very large component of the photon polarization vector in the [110] crystalline direction, accounting in part for the high intensity of the band six peak, which has Σ_1 symmetry and a large amount of d-character in an LCAO tight-binding sense.[7] An important observation is that Σ_1 symmetry bands that are predominantly s-derived do not have a large cross-section.

Comparison of the normal emission spectra for the two azimuthal orientations (Fig. 7) reveals a considerable polarization dependence in the spectra. Table I presents the direction cosines for the polarization vector relative to the [110], [100], and [1$\bar{1}$0] crystal axes. Results are presented based on the angle of incidence of the light beam and also for the estimated orientation of the polarization vector inside the metal. The refraction of the light at the surface was estimated from Snell's Law using a refractive index $n = 0.949$ determined experimentally[15] for $h\nu = 45$ eV.

The spectra in Fig. 7 indicate qualitative agreement with the differences in the selection rules for the two azimuthal orientations. In Fig. 7a and 7b the lower binding energy portion is enhanced with respect to the rest of the valence band due to the allowed transitions from the Σ_4 state at 2.8 eV E_B. The large intensity of the higher binding energy portion of the "d-band" region in Fig. 7c and 7d can be understood in terms of the allowed transition from the Σ_3 initial state at 3.7 eV E_B. However, polarization selection rules do not account for the strong intensity observed in all spectra at 2.5 eV E_B. For a primary cone direct transition process, the band corresponding to this binding energy has Σ_2

symmetry and should not contribute to the photocurrent in the [110] direction. Secondary cone emission for these final state energies is probably very small. Thus, the intensity in this spectral region is most likely due to indirect transitions. This is supported by the fact that the high temperature ARP spectrum of the band six resonance region, which emphasizes indirect transitions due to thermal disorder, is peaked strongly at 2.8 eV E_B.[16]

Another important polarization effect in photoemission arises from the interaction of the photon electric field vector $\vec{E}$ (parallel to $\vec{\mu}_o$) with the metal surface. As discussed by Kleiwer,[17] p-polarized light can cause a significant surface photoeffect, i.e., indirect transitions caused by the interaction of the time-varying electric field with the metal surface. These interactions are weighted by a factor of $1/|\vec{q}|^2$, where $\vec{q}$ is the difference in wavevector between the normal direct transition channel and the indirect transition channel. Thus, most indirect transitions will occur in an area of $\vec{k}$-space localized near the direct transition channel.

Surface photoemission is expected to contribute most heavily to ARP spectra for near grazing incidence p-polarized radiation and normal electron emission directions.[17] Thus, the enhanced peak structure in the off-normal spectra (compare especially Fig. 7a to Fig. 7b and Fig. 7c to Fig. 7d) may be explained by the reduced yield of indirect transitions due to the surface effect. The off-normal spectra of Figs. 2 and 4 have generally sharper and narrower features than their near normal emission counterparts in Figs. 3 and 5. This is actually contrary to the expectations of peak broadening by an increase in the number of momentum states

allowed when the effective photoelectron sampling depth is reduced by the lower emission angles. Thus, some broadening mechanism must be present for the normal emission case, and that broadening is apparently quite severe. Nevertheless, the photoemission spectra from Cu(110) are dominated by direct transition processes for the range of photon energies 4s eV $\leqslant h\nu \leqslant$ 160 eV. "Surface emission" accounts for relatively little of the observed intensity for $h\nu$ = 45 eV even if the differences between Figs. 7a and 7b and Figs. 7c and 7d are totally due to the surface effect.

The effect of the polarization vector in determining the magnitude of the transition matrix elements should also be mentioned. In the simple free-electron final-state picture[18] the intensity of a photoelectron transition is weighted by a $\cos^2\alpha$ term, where α is the angle between $\vec{\mu}_o$ and $\vec{k}_f$. Smith, et al.[11] routinely collect ARP spectra in the photon energy region below 20 eV for $\alpha = 90^\circ$. They explain the photoemission final state as a Bloch sum of plane waves,

$$|\vec{k}_f\rangle = \sum_{\vec{G}} C_{\vec{G}}(\vec{k}_f)\exp(-i(\vec{k}_f + \vec{G})\cdot\vec{r}) \qquad (4)$$

that can allow emission into any direction with respect to $\vec{\mu}_o$ because of the sum over the reciprocal lattice vectors $\vec{G}$. However, the coefficients $C_{\vec{G}}(\vec{k}_f)$ for $|\vec{G}| > 0$ are expected to decrease with increasing final-state energy, leading to a more plane wave-like final-state. This is in fact observed experimentally; the photoemission yield for an orientation with $\vec{k}_f \cdot \vec{\mu}_o = 0$ for photon energies $\geqslant$ 40 eV is considerably lower (about two orders of magnitude) than that for the orientation utilized

to collect the spectra presented here. This would indicate that in this energy range initial states allowed by the component of the polarization vector in the detector direction will be strongly enhanced over the other possible transitions.

C. Summary

Finally, possible spectral effects due to deviations from the bulk band structure as the final-state becomes more surface sensitive should be mentioned. The most spectacular surface specific effect is the appearance of photoemission from surface states. None of the features in the spectra presented here can be assigned to such initial states. However, bulk bands are predicted to change upon approaching a solid surface. Sohn, et al.[19] have performed several calculations for the low index faces of Cu which indicate that the total d-band width narrows for states near the surface. Indeed, a slight narrowing of the x-ray photoelectron VB spectra of copper for near grazing electron emission angles confirms this expectation.[20] Thus, direct-transition features in ARP spectra are not expected to correspond exactly to bulk band positions. The fact that they do correspond so closely confirms that photoemission is indeed a technique capable of band structure determination, and that the surface electronic structure is almost (surprisingly) unchanged from that of the bulk.

In summary, it is shown that refraction of photoelectrons at the solid-vacuum interface does occur and that the refraction angle is somewhat larger than expected in a simple plane wave picture for the case studied. This latter result cannot be uniquely explained, although the

inner potential of the hot electron and its group velocity (or effective mass) are the most important factors in determining surface refraction. In addition, considerable polarization dependence has been observed in the features of the ARP spectrum of Cu and are in qualitative agreement with direct transitions obeying dipole selection rules. However, additional intensity is found in the spectra that cannot be due to direct transition processes. Near grazing incidence p-polarized light is shown to contribute a small amount of surface emission to the spectra which can obscure direct transition features. It is concluded that a successful theoretical description of ARP spectra will have to include indirect as well as direct transition processes; the calculation of the relative magnitudes being the most important, and probably most difficult, theoretical parameter in the interpretation of experimental spectra. Experimentally, utilizing off-normal emission geometries with the light polarization in the electron detection direction may be the best method for obtaining spectra free from indirect transitions due to surface emission.

REFERENCES

*This chapter is to appear in part as "Electron Refraction and Light Polarization Effects in Angle-Resolved Photoemission Spectra of Cu Surfaces Using 45 eV Radiation," R. S. Williams, P. S. Wehner, J. Stöhr, and D. A. Shirley, Surface Science XX, XXX (1978).

1. D. A. Shirley, J. Stöhr, P. S. Wehner, R. S. Williams, and G. Apai, Physica Scripta 16, 398 (1977).
2. J. Stöhr, G. Apai, P. S. Wehner, F. R. McFeely, R. S. Williams, and D. A. Shirley, Phys. Rev. 14, 5144 (1976).
3. L. F. Wagner, Z. Hussain, and C. S. Fadley, Solid State Commun. 21, 257 (1977).
4. D. J. Spanjaard, D. W. Jepsen, and P. M. Marcus, Phys. Rev. B15, 1728 (1977).
5. R. McLean and R. Haydock, J. Phys. C 10, 1929 (1977).
6. G. D. Mahan, Phys. Rev. B2, 4334 (1970).
7. J. Stöhr, P. S. Wehner, R. S. Williams, G. Apai, and D. A. Shirley, Phys. Rev. B17, 587 (1978).
8. L. Hedin and B. I. Lundqvist, J. Phys. C 4, 2064 (1971).
9. P. O. Gartland and B. J. Slagsvold, Phys. Rev. B12, 4047 (1975).
10. R. Ray and G. D. Mahan, Phys. Lett. 42A, 301 (1972).
11. M. Sunjić and G. Toulouse, Solid State Commun. 11, 1629 (1972).
12. V. L. Moruzzi, P. M. Marcus, and J. A. Knapp, to be published.

13. C. S. Fadley, Progress in Solid State Chemistry 11, 265 (1976).

14. J. Hermanson, Solid State Commun. 22, 9 (1977).

15. H.-J. Hagemann, W. Gudat, and C. Kunz, DESY SR-7417 (Hamburg) 1974.

16. R. S. Williams, P. S. Wehner, J. Stöhr, and D. A. Shirley, Phys. Rev. Lett. 39, 302 (1977).

17. K. L. Kliewer, Phys. Rev. Lett. 33, 900 (1974); Phys. Rev. B14, 1412 (1976); Phys. Rev. B15, 3759 (1977).

18. J. W. Gadzuk, Phys. Rev. B10, 5030 (1974).

19. K. S. Sohn, D. G. Dempsey, L. Kleinman, and E. Caruthers, Phys. Rev. B13, 1515 (1976); Phys. Rev. B14, 3185 (1976); Phys. Rev. B14, 3193 (1976).

20. M. Mehta and C. S. Fadley, Phys. Rev. Lett. 39, 1569 (1977).

21. G. A. Burdick, Phys. Rev. 129, 138 (1963).

Table I. Direction Cosines of $\vec{\mu}_o$ wrt the Bulk Crystalline Axes

Allowed Initial State	Crystal Axis	Plane of [110] and [100][a]		Plane of [110] and [111][b]	
		Incident[c]	Refracted[d]	Incident[c]	Refracted[d]
Σ_1	[110]	0.889	0.875	0.889	0.875
Σ_3	[001]	0.0	0.0	0.459	0.483
Σ_4	$[1\bar{1}0]$	0.459	0.483	0.0	0.0

a) Orientation of Fig. 7b.
b) Orientation of Fig. 7d.
c) Incident angle between $\vec{\mu}_o$ and [110] of 27.3°.
d) Refracted angle between $\vec{\mu}_o$ and [110] of 28.9°.

FIGURE CAPTIONS

Fig. 1. Burdick's band structure of Cu^{21} along the ΓK direction. The dashed curves are empty-lattice energy bands (referenced to the zero of the crystal potential) shifted down in energy by 45 eV, the photon energy employed in this study. The empty-lattice band with positive slope nominally carries electrons in the [110] crystalline direction. The negative slope final state band is doubly degenerate, consisting of Σ_1 and Σ_4 bands which would be split by a crystal potential.

Fig. 2. Experimental results obtained as a function of θ from a Cu(100) crystal surface. The experimental geometry is shown in the inset. The angular acceptance was a cone of 5° half angle.

Fig. 3. Experimental spectra obtained from a Cu(110) surface. The crystal orientation is illustrated in the inset.

Fig. 4. Spectra obtained from a Cu(111) crystal face.

Fig. 5. Spectra obtained from a Cu(110) crystal face. The azimuthal orientation of this crystal differs by 90° from that in Fig. 3, as illustrated in the inset.

Fig. 6. This figure summarizes the intensity variations of the band six peak as a function of θ for the spectra presented in Figs. 2-5. The area under the band six peak relative to the total valence band intensity is plotted as a function of θ for the

four sets of data collected. The [110] axis for each of the crystals is shown. The azimuthal orientations of the crystalline axes with respect to the plane defined by $\vec{S}$ and $\vec{k}_f$ were equivalent for parts a and b and for parts c and d of this figure. The refraction angles can be determined by the maxima of the plots in parts a and c.

Fig. 7. Here are presented the spectra collected nearest the [110] internal emission direction for each of the crystal orientations of Figs. 2-5. The dashed lines are the initial state lattice band from Fig. 1, and are labeled by the symmetry of the initial state band.

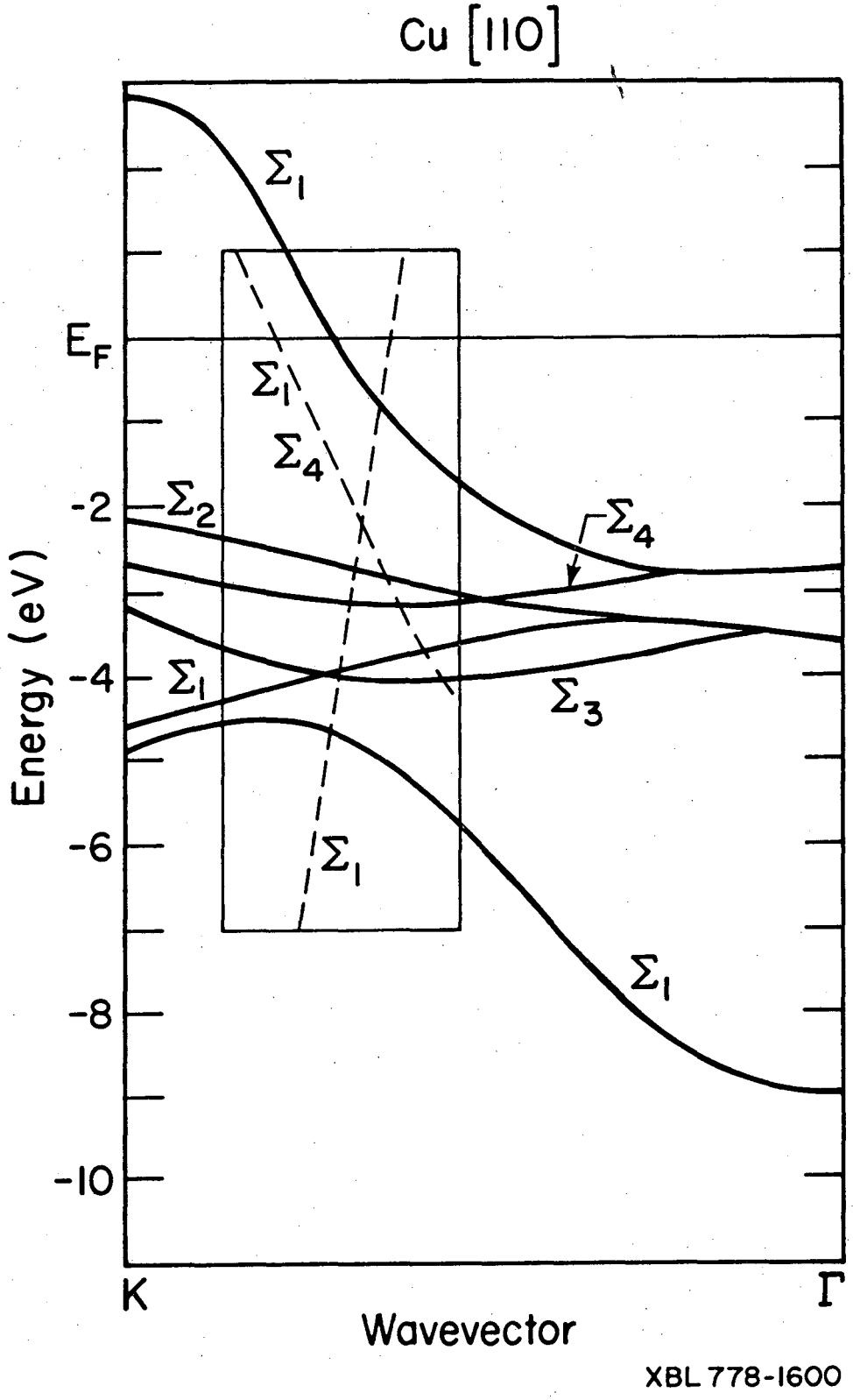
Cu [110]
Σ_1
E_F
Σ_1
Σ_4
Σ_2
Σ_4
Σ_1
Σ_3
Σ_1
Σ_1
Energy (eV)
-2
-4
-6
-8
-10
K
Γ
Wavevector
XBL 778-1600

Fig. 1

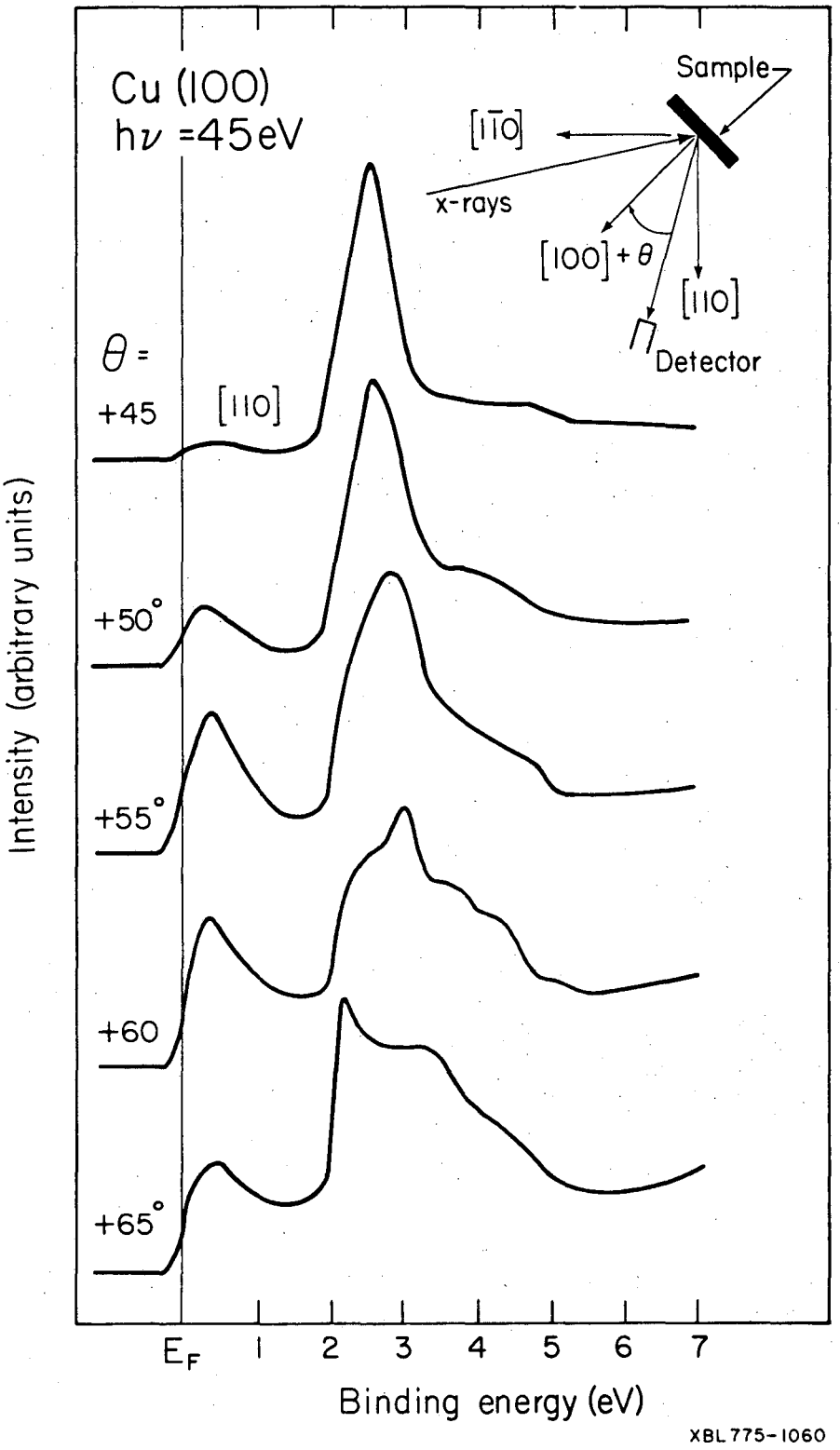
Cu (100)
hν =45eV
Sample
[1$\bar{1}$0]
x-rays
[100] + θ
[110]
Detector
θ =
+45
[110]
+50°
+55°
+60
+65°
Intensity (arbitrary units)
E$_F$
1
2
3
4
5
6
7
Binding energy (eV)
XBL775-1060

Fig. 2

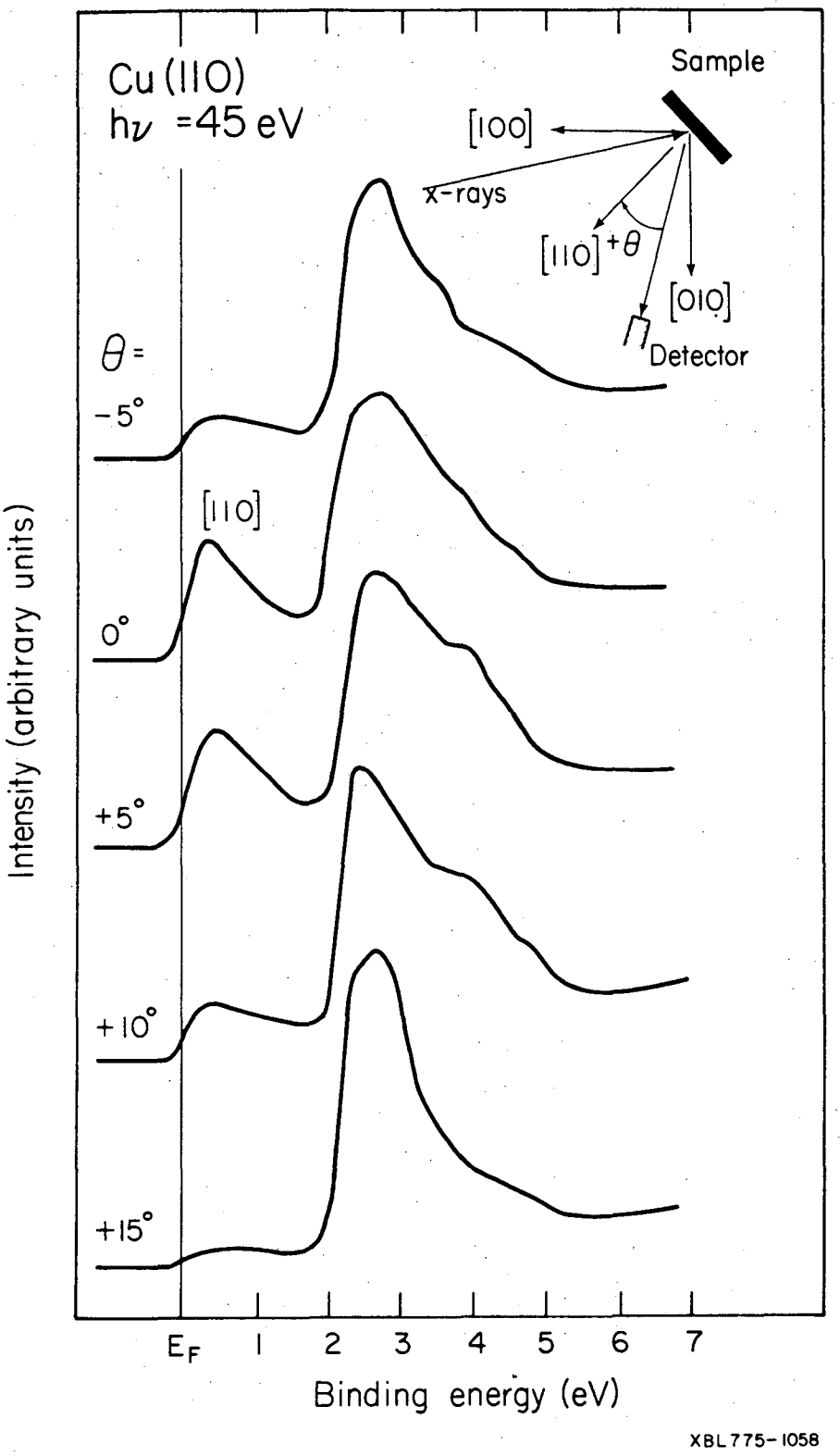
Cu (110)
hν =45 eV
Sample
[100]
x-rays
[110] +θ
[010]
Detector
θ =
-5°
[110]
0°
+5°
+10°
+15°
Intensity (arbitrary units)
E_F
1
2
3
4
5
6
7
Binding energy (eV)
XBL775-1058

Fig. 3

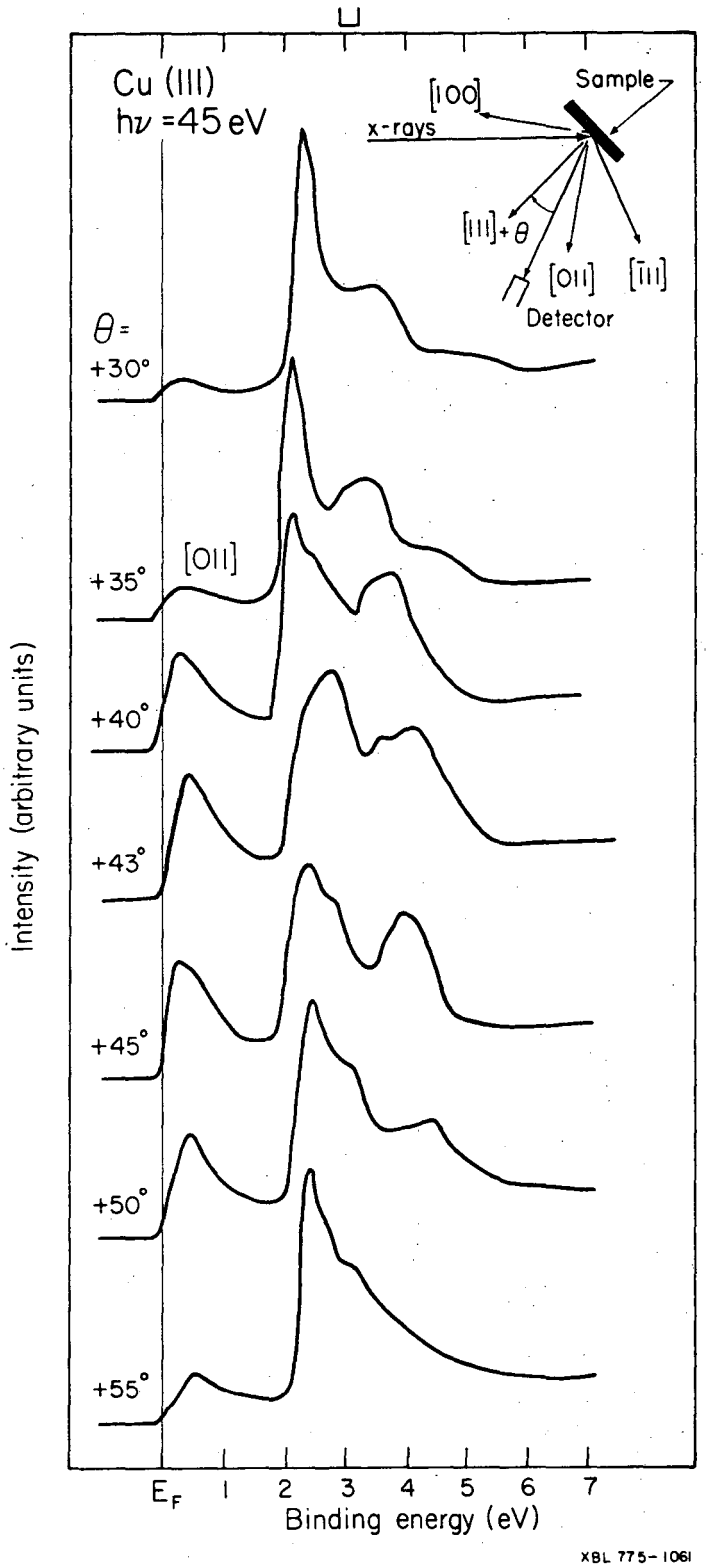
Cu (111)
hν =45 eV
[100]
Sample
x-rays
[111]+θ
[011]
[$\bar{1}$11]
Detector
θ=
+30°
+35°
[011]
+40°
+43°
+45°
+50°
+55°
Intensity (arbitrary units)
E$_F$
1
2
3
4
5
6
7
Binding energy (eV)
XBL 775-1061

Fig. 4

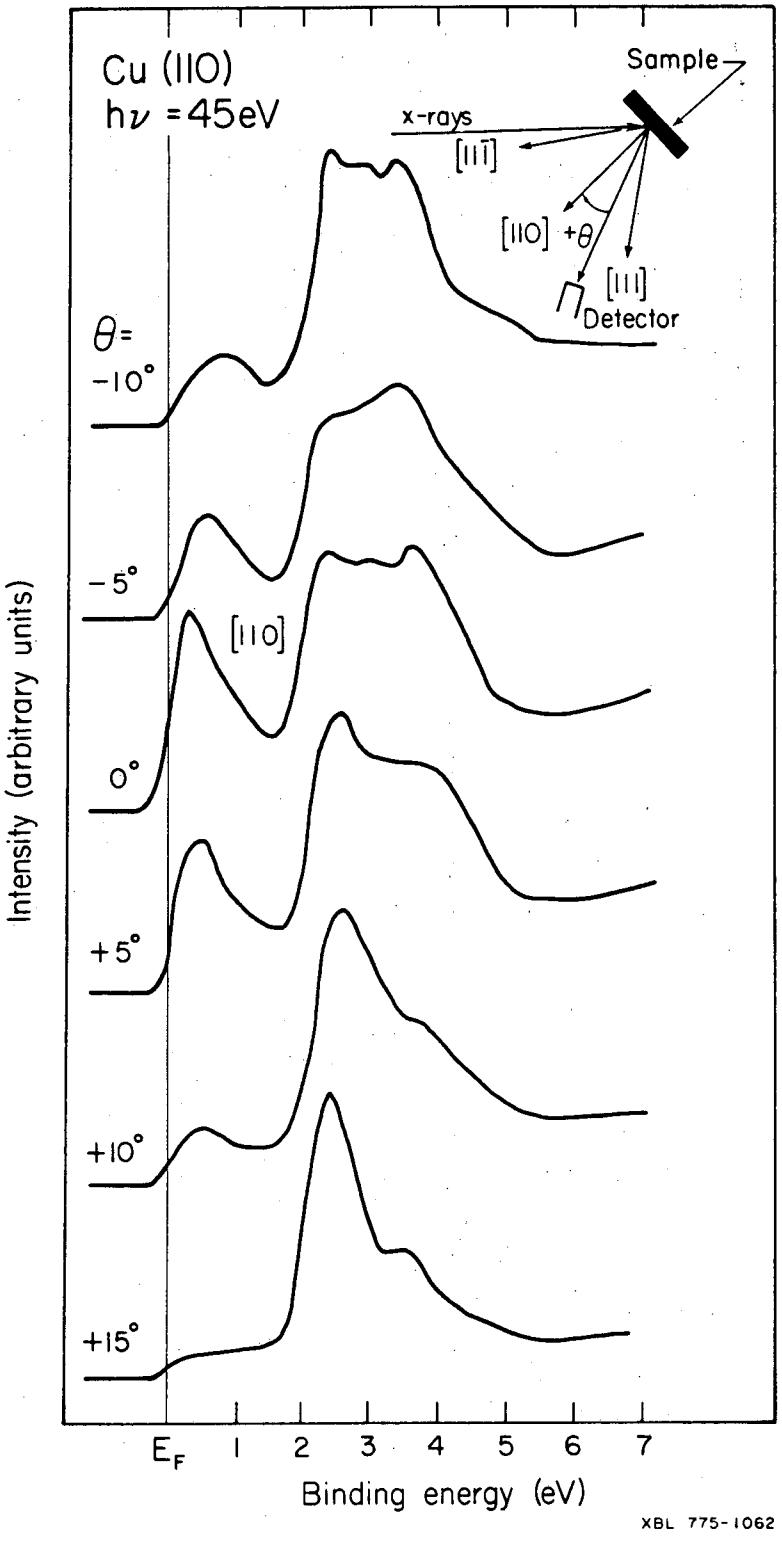
Cu (110)
hν =45eV
Sample
x-rays
[11$\bar{1}$]
[110] +θ
[111]
Detector
θ=
-10°
-5°
[110]
0°
+5°
+10°
+15°
Intensity (arbitrary units)
E$_F$
1
2
3
4
5
6
7
Binding energy (eV)
XBL 775-1062

Fig. 5

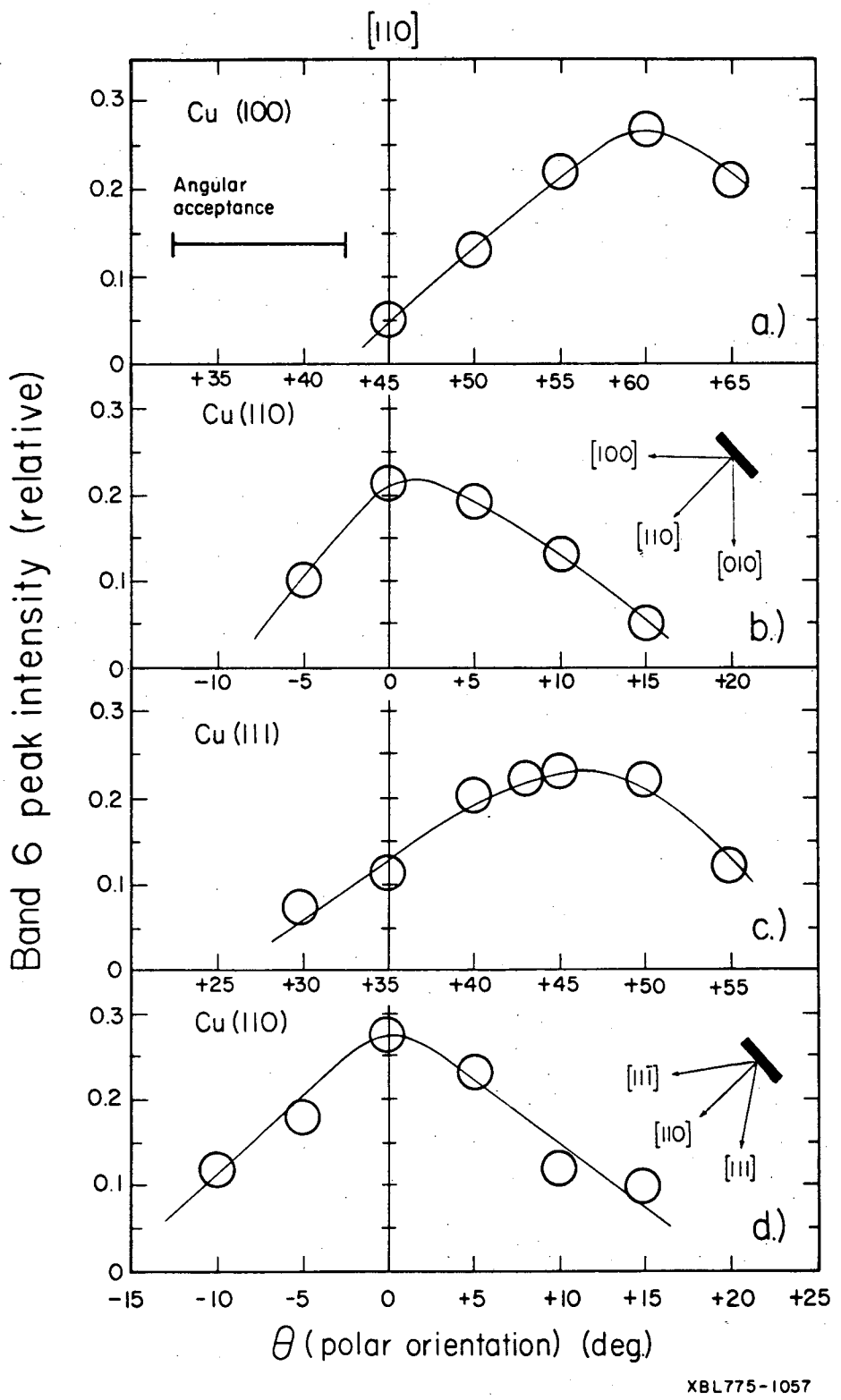
[110]
Cu (100)
Angular acceptance
a.)
Cu (110)
[100]
[110]
[010]
b.)
Cu (111)
c.)
Cu (110)
[11$\bar{1}$]
[110]
[111]
d.)
Band 6 peak intensity (relative)
θ (polar orientation) (deg.)
XBL775-1057

Fig. 6

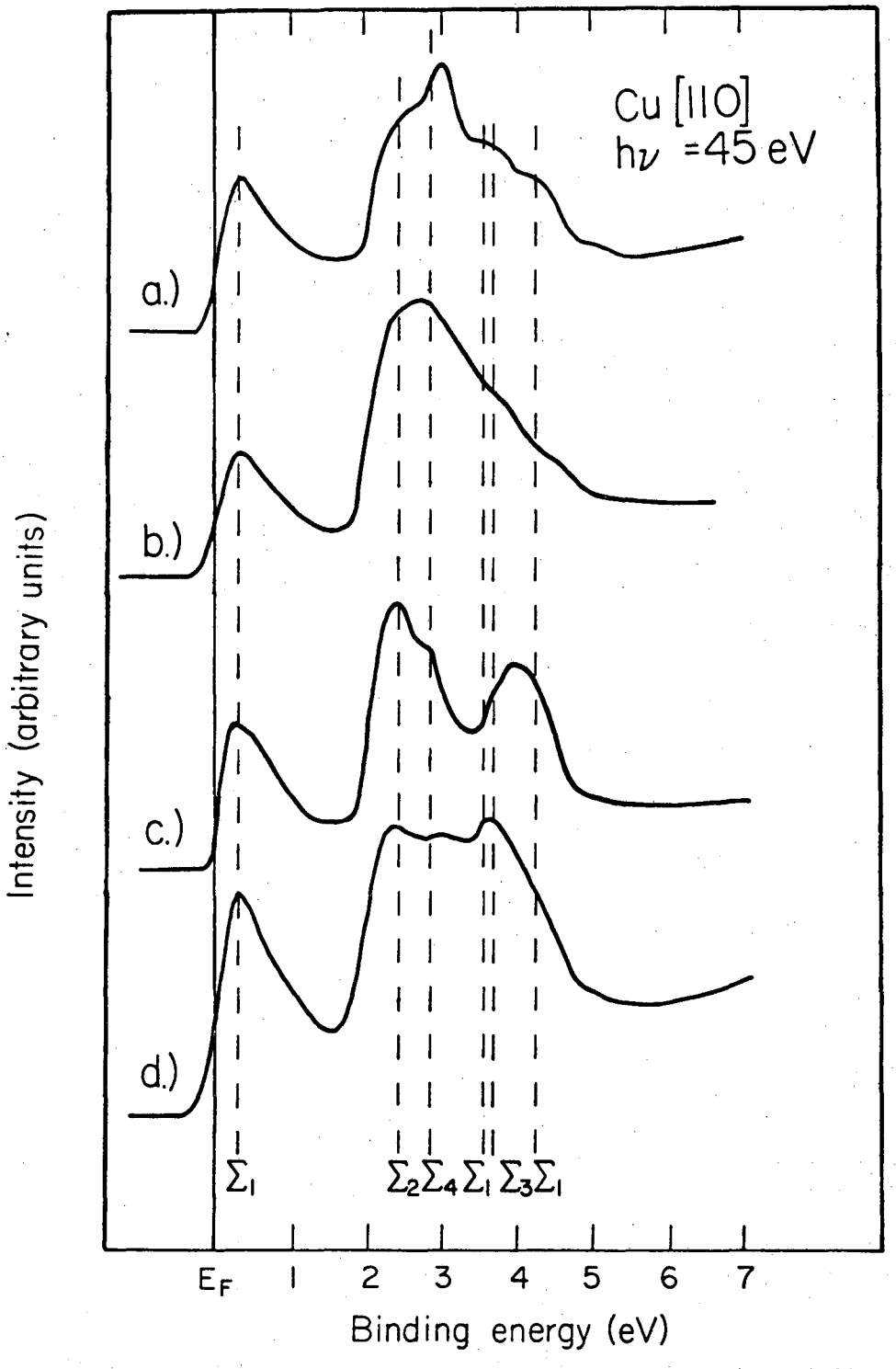
Cu [110]
hν =45 eV
a.)
b.)
c.)
d.)
Intensity (arbitrary units)
Σ1
Σ2Σ4 Σ1 Σ3Σ1
EF
1
2
3
4
5
6
7
Binding energy (eV)
XBL 778-9850

Fig. 7

VII. PHOTOEMISSION FROM SURFACE STATES

Surface electronic states on low-index planar metal surfaces have received considerable theoretical attention, and experimental examples are known for Mo and W(100)[1] and Cu(111).[2] Until now, however, the detailed surface electronic structure of stepped crystals has received much less attention, in spite of its obvious importance, and no detailed theoretical predictions of surface states on stepped crystals are available. This chapter reports angle-resolved photoemission studies of the Cu(111) surface state and a recently discovered surface state on a stepped Cu(211) crystal, for which the (211) face is known to have a stable surface configuration consisting of three-atom (111) terraces and single-atom (100) steps.[3] The surface state was found at 0.20 ± 0.07 eV below the Fermi energy. This state — the first surface state to be observed on a stepped crystal — was characterized by the angle- and energy-dependence of its photoemission spectra, and particularly by comparison with the surface state at 0.29 ± 0.07 eV below E_F on Cu(111). It is further demonstrated that the (211) surface state is associated with the Cu(111) terraces. Implications about the nature of the stepped-crystal surface potential are noted below, and further experiments that demonstrate the increased reactivity of a (211) stepped crystal relative to a (111) crystal are also reported.

A. Surface State Emission

Photoemission from a surface localized initial state is represented in Fig. 1. The surface state wavefunction is strongly damped into the solid and is thus very sensitive to the conditions at

the interface region due to its highly localized nature.

Figure 2 depicts a segment of an ideal (S)-[3(111) × (100)] surface;[3] monatomic (100) steps are separated by three-atom (111) terraces. Only one-third of the surface atoms (in "C" rows) have the complete coordination geometry of a (111) surface. Surface electronic structure effects associated with excess charge at step sites[4] should therefore be substantial, if indeed they are present.[5] Angle-resolved photoemission is the technique of choice for studying these effects.

Single crystals of copper were cut to within ±0.5 degrees of the (211) and (111) planes. The crystals were cleaned and annealed in vacuum. Sharp LEED patterns were obtained for each crystal, with the characteristic (S)-[3(111) × (100)] surface geometry evident on the Cu(211) surfaces. In situ Auger analysis showed no surface contaminants present within the limits of detectability (approximately 0.03 monolayer).

Photoemission spectra were run on the 8° branch line of Beam Line I at the Stanford Synchrotron Radiation Laboratory, using a photoemission chamber described previously:[6] photon energies in the range $h\nu$ = 8-35 eV were available. The incident beam was highly (> 97%) polarized in the horizontal plane, and the electron analyzer was fixed in this plane, accepting electrons emitted at 145° relative to the photon beam direction. The acceptance angle of the analyzer was 24 msterad (5° half angle). The electron take-off angle was varied relative to the crystal by rotation of the sample about the vertical axis. The total experimental resolution increased from ca. 0.17 eV at $h\nu$ = 8 eV to ca. 0.26 eV at $h\nu$ = 35 eV.

Figures 3 and 4 show photoemission spectra taken at several electron take-off angles Θ, with a photon energy of 11 eV from the Cu(111) and (211) surfaces, respectively. The (211) surface state appears as a peak at a binding energy of 0.20 ± 0.07 eV at $\Theta = 20°$, the [111] bulk direction (Fig. 4). As Θ is increased or decreased from this value, the peak decreases in intensity and shows some dispersion, disappearing at $\Theta = 10°$ and 30°. These are the same characteristics exhibited by the surface state on Cu(111)[2] (Fig. 3), for rotations about the normal to the surface. It is inferred that the Cu(111) surface state, which shows a maximum in both binding energy and intensity in normal photoemission, is present in slightly modified form on the (111) terraces of stepped Cu(211), with maxima in these properties normal to the terraces; i.e., also along the [111] direction. This is the first observation of a surface state on a stepped crystal. A puzzling feature about the emission from this state is that it appears to show very little or no photoelectron refraction, despite the conservation of parallel crystal momentum implied by the dispersion of the feature with take-off angle.

While the Cu(211) and Cu(111) surface states are very similar, they are not identical. Certain differences are evident in Fig. 5, which compares photoemission spectra in the [111] direction from Cu(211) and Cu(111) crystal for selected photon energies. The (211) surface state binding energy is apparently slightly lower than that of the (111) surface state, as noted above. The intensity of the (211) surface state also appears to be lower relative to bulk band-structure

features. It is tempting to attribute this reduced intensity to a smaller relative "area" of unperturbed (111) face on the stepped crystal. This interpretation can only be tentative pending further study, however, because of the extremely high sensitivity of surface states to surface quality and the difference in the radiation polarization at the two faces.

Turning to the bulk-derived features of the photoemission spectra, the Cu(211) results are similar to those from Cu(111). The Cu(211) bulk features do show refraction, and they can be interpreted within the direct transition model (Chap. III). Evidence for refraction is provided by comparing the angle-dependent spectra in Figs. 3 and 4. The two data sets are nearly brought into register by a shift $\Delta\theta \sim -10°$ in the angle from the surface normal for the Cu(211) data; i.e., bulk spectral features from the Cu(211) face that would be observed along the [111] direction in the absence of refraction appear instead at a larger angle from the (211) surface normal.

Further evidence for refraction of bulk features is presented in Fig. 5, in which photoemission spectra in the [111] direction are compared for Cu(211) and Cu(111) surfaces. At the lowest photon energies ($h\nu$ = 9 eV) the bulk feature in the two spectra are relatively shifted both because the refraction angle is larger for low-energy electrons and because the initial-state bands sampled at these energies happen to have a steeper dispersion. Observed positions of bulk band features, interpreted on the direct-transition model, agree well with the bulk copper theoretical band structure (Chap. III). The surface

state is conspicuous in its separation from the bulk bands and in its dispersion behavior.

B. Chemisorption on the Cu(211) Surface

As a final observation preliminary studies of the enhanced surface reactivity of Cu(211) are reported. On simultaneous exposure of a Cu(111) and a Cu(211) surface to 10^3L of O_2, the Cu(111) surface revealed no detectable oxygen, while the Cu(211) surface showed ca. 0.8 monolayer of oxygen, as measured by the Auger signal. Angle-resolved photoemission spectra in the [111] direction (Fig. 6) showed that the (211) surface state had essentially disappeared (see the $h\nu$ = 9 eV spectrum) while a feature appeared at a binding energy of ca. 1.6 eV that has been attributed to a Cu-O antibonding orbital.[7] For emission normal to the (211) face at 18 eV photon energy, another oxygen induced feature may be observed at 2.5 eV E_B which has not been reported previously (Fig. 6).

The greater oxygen sticking coefficient at room temperature for Cu(211) surfaces as opposed to the (111) face demonstrates the enhanced chemical reactivity of steps (viz. defects) as compared with more planar or regular surfaces. The study of chemisorption on irregular surfaces is difficult, but valence band ARPES using a synchrotron radiation source can allow a very thorough search of the valence band region to detect small changes in the substrate valence features due to adsorbate bonding at the surface. However, additional work is required before photoemission intensity modulations in valence band spectra can be interpretted in terms of bonding between adsorbate and substrate.

In summary, it is concluded that the surface potential on (111) terraces of stepped Cu(211) is sufficiently similar to that of Cu(111) to support a similar, but not identical, surface state. Otherwise the electronic structure of the (211) surface resembles that of bulk copper, or of a (111) surface even at an fair level of detail. This suggests that the enhanced reactivity of the stepped surface — observed in this case for O_2 — may well arise more from steric effects due to step-adsorbate geometry than from any particular electronic-structural property of these steps.

REFERENCES

1. B. Feuerbacher and B. Fitton, Phys. Rev. Lett. 29, 786 (1972); B. Feuerbacher and N. E. Christensen, Phys. Rev. B10, 2373 (1974); R. C. Cinti, E. Al Khoury, B. K. Chakraverty, and N. E. Christensen, Phys. Rev. B14, 3296 (1976).

2. P. O. Gartland and B. J. Slagsvold, Phys. Rev. B12, 4047 (1975); D. R. Lloyd, C. M. Quinn, and N. V. Richardson, J. Chem. Soc. Faraday Trans. II (G.B.) 72, pt. 6, 1036 (1976).

3. B. Land, R. W. Joyner, and G. A. Somorjai, J. Catalysis 27, 405 (1972).

4. K. S. Sohn, D. G. Dempsey, and L. Kleinman, private communication.

5. G. S. Painter, P. J. Jennings, and R. O. Jones, J. Phys. C 8, L199 (1975).

6. D. A. Shirley, J. Stöhr, P. S. Wehner, R. S. Williams, and G. Apai, Physica Scripta 17, 398 (1977).

7. D. T. Ling, J. N. Miller, I. Lindau, D. L. Weissman, P. Pianetta, and W. E. Spicer, private communication.

FIGURE CAPTIONS

Fig. 1. A schematic representation of the wavefunctions and energy levels involved in a photoemission transition from a surface state $|E_i,\vec{k}_i\rangle$ to a damped final state $|E_f,\vec{k}_f\rangle$.

Fig. 2. An illustration of a segment of a 3(111) × (100) stepped surface (an ideal termination of the fcc bulk crystal lattice at a (211) plane). The step terraces are three atoms (in a (111) plane) broad with step heights one atom high (along a (100) plane). The surface periodicity is composed of three adjacent inequivalent atomic rows (labeled A, B, and C). Only the C atoms have the Cu(111) surface nearest neighbor structure.

Fig. 3. ARPES spectra collected from a Cu(111) surface at a photon energy of 11 eV as a function of the angle Θ from the surface normal. The angle between the photon beam and the e^- detector is fixed at 37° and the polarization vector lies in the plane of the inset. The surface state emission is the spectral feature observed at 0.3 eV E_B in the $\Theta = 0°$ spectrum.

Fig. 4. ARPES spectra collected from a Cu(211) surface at a photon energy of 11 eV as a function of the angle Θ from the surface normal. Surface state emission is observed at 0.23 eV E_B in the spectrum collected at $\Theta = 20°$, which corresponds to the [111] direction of the bulk crystal.

Fig. 5. Comparison of spectra collected in normal emission from the Cu(111) surface (dashed lines) to spectra collected at $\Theta = 20°$ from the Cu(211) surface (solid lines) for selected photon

energies. At $h\nu$ = 9 eV, the peaks arising from bulk features (ie. $E_B > 1$ eV) have significantly different binding energies in the two spectra due to strong electron refraction at low kinetic energies and the large E vs $\vec{k}$ dispersion of the initial states sampled.

Fig. 6. ARPES spectra collected from clean (dashed lines) and 0.8 monolayer oxygen coverage (solid lines) Cu(211) surfaces. The surface state seen in the (111) bulk crystalline direction is seen to be much more sensitive to surface contamination than other features. Oxygen induced peaks are seen at ~ 3 eV E_B in the normal emission spectrum and ~ 1.5 eV E_B in the [111] direction spectrum at 18 eV E_B.

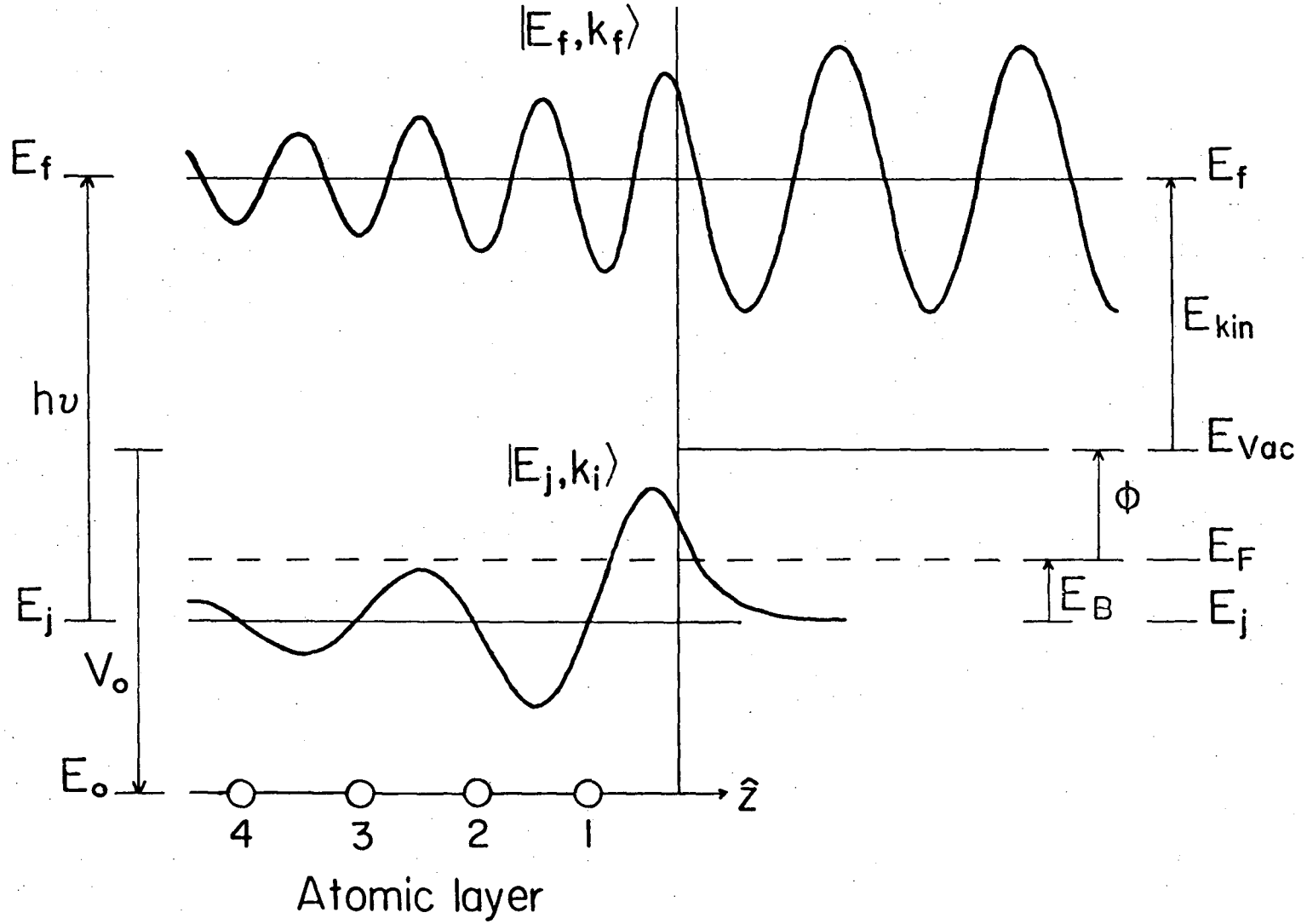

XBL 785-8773

Fig. 1

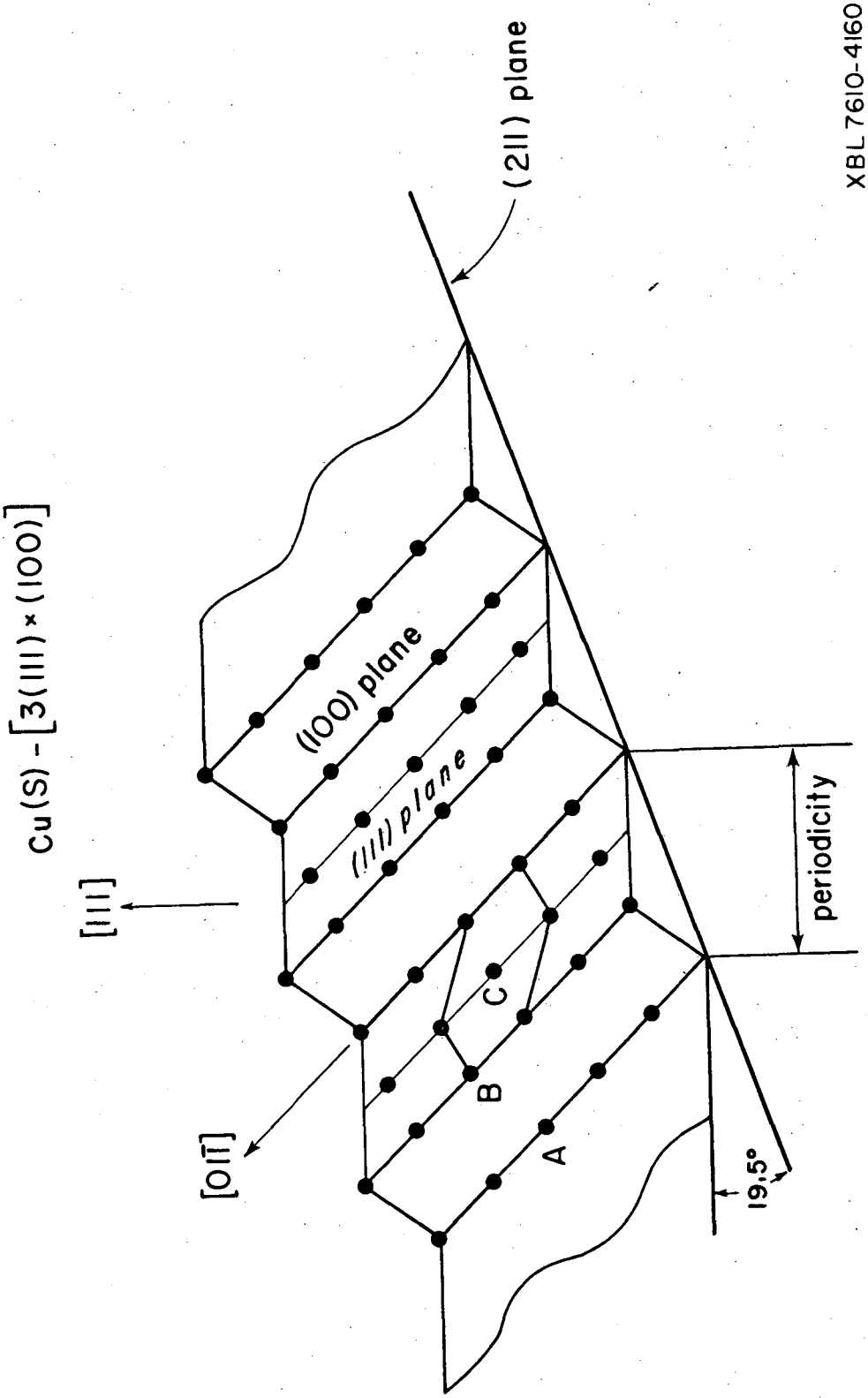

XBL 7610-4160

Fig. 2

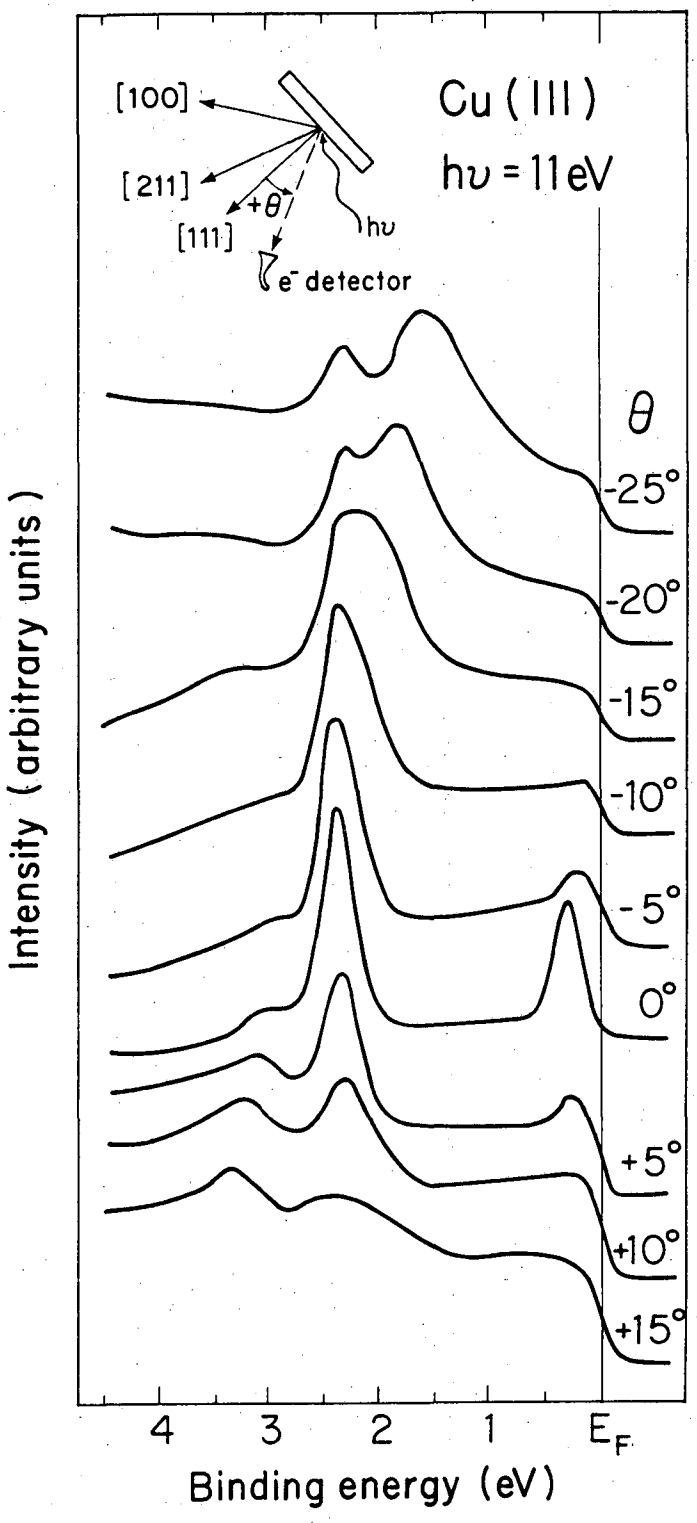

XBL 783-463

Fig. 3

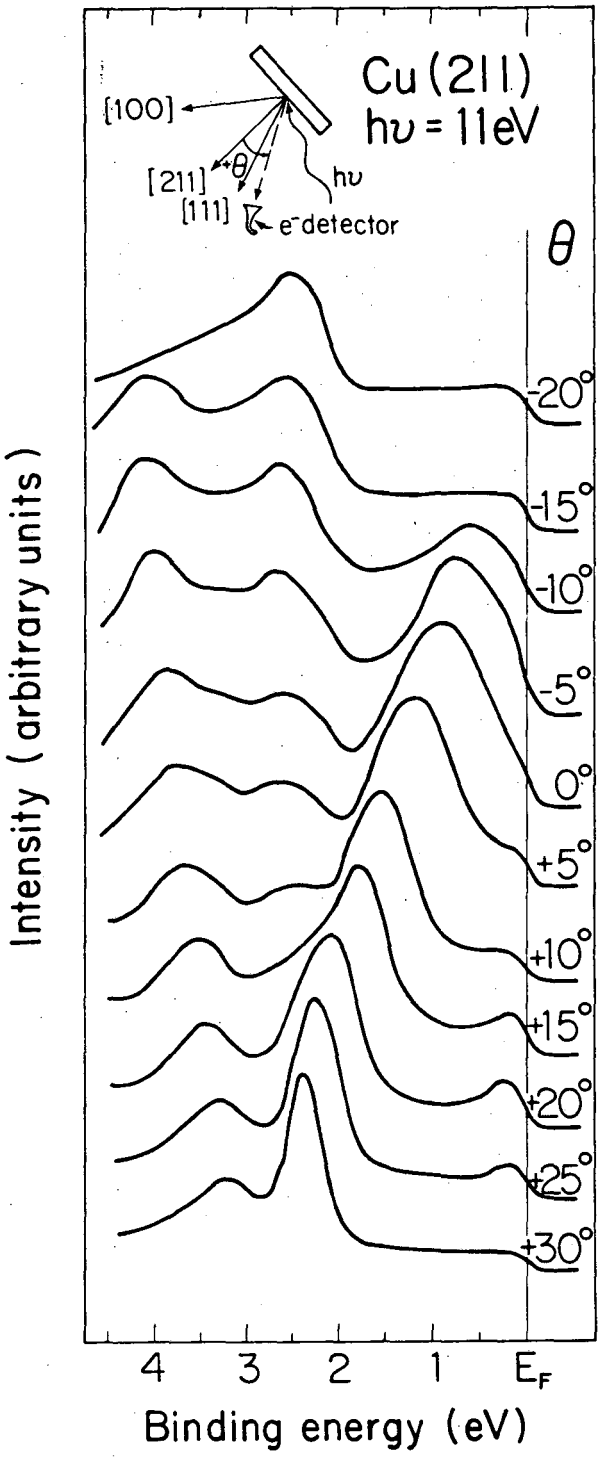

XBL 784-466

Fig. 4

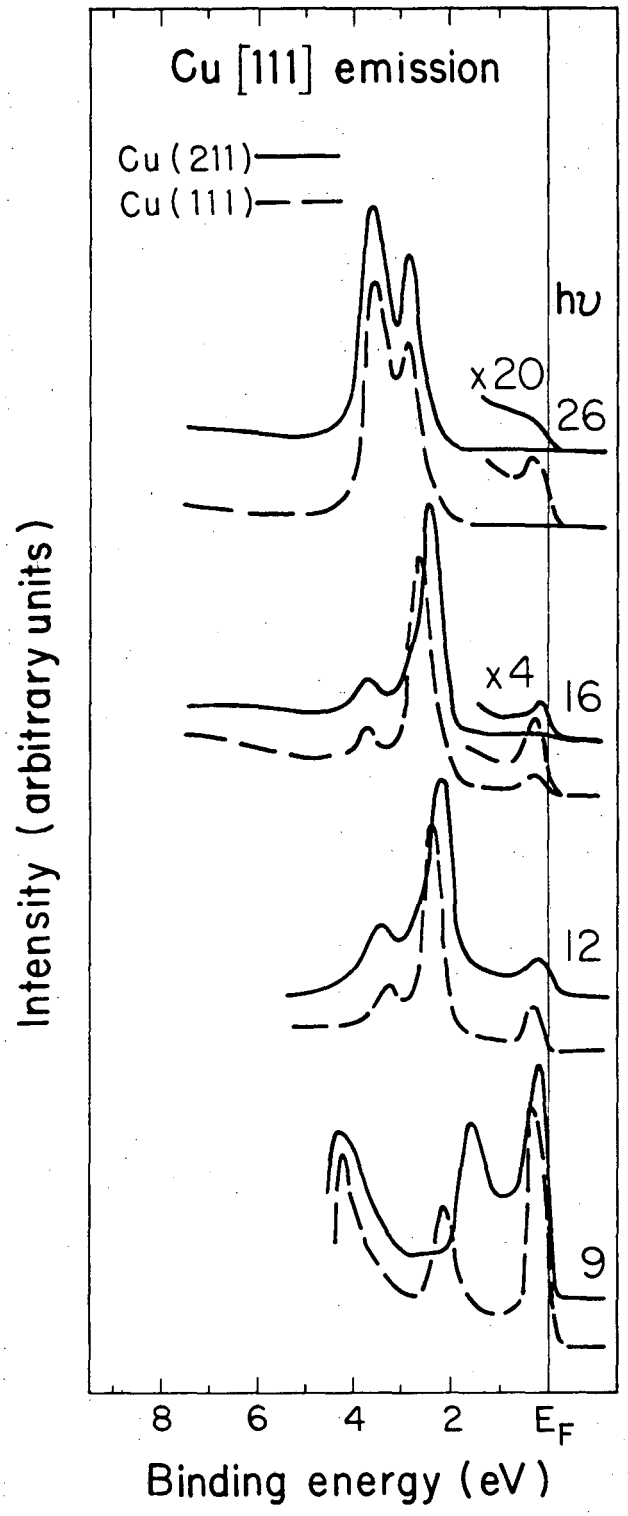

XBL 784-465

Fig. 5

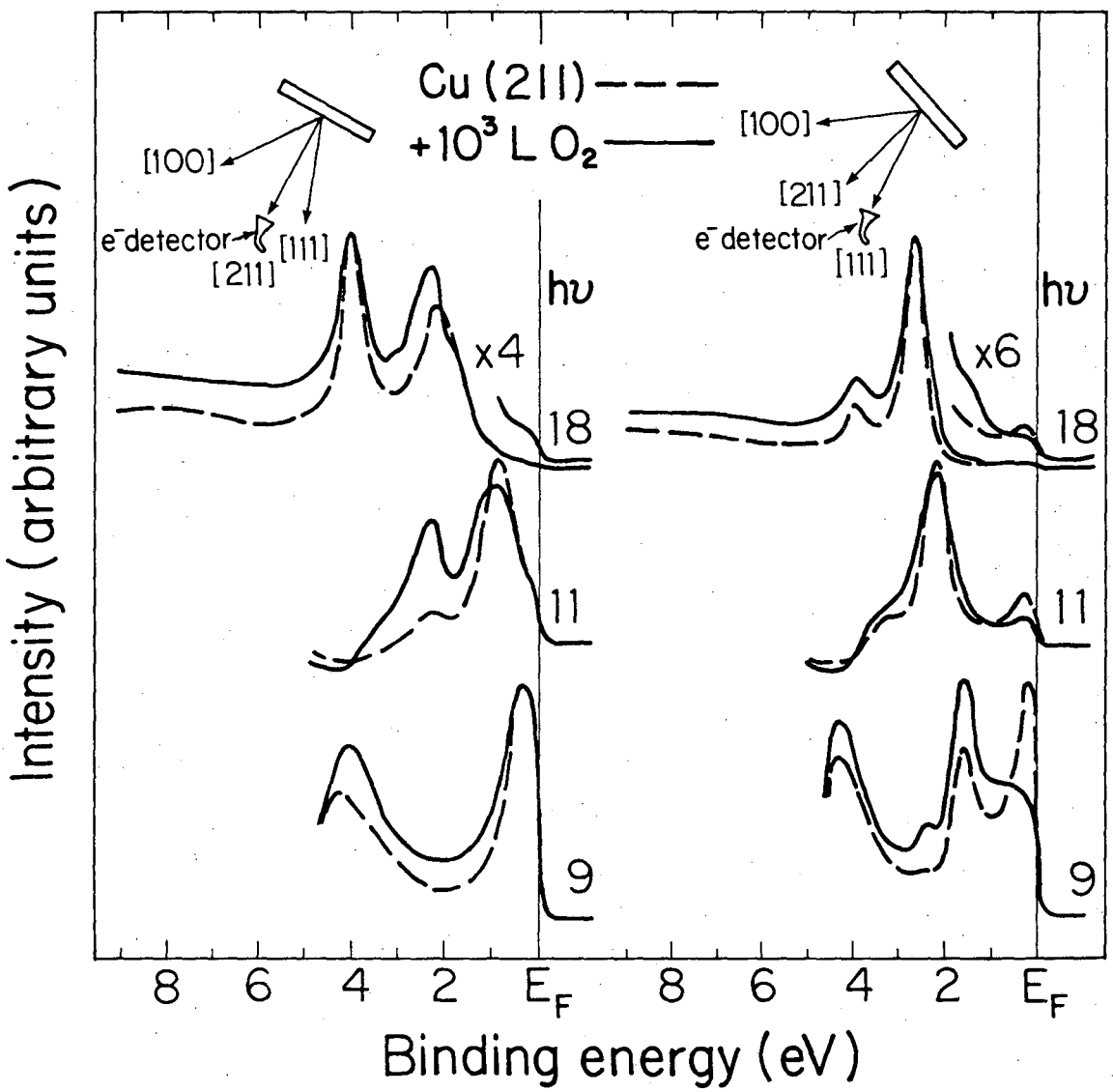
Cu (211) ---
+10³ L O₂ ——
[100]
e⁻ detector
[211]
[111]
hυ
x4
18
11
9
[100]
[211]
e⁻ detector
[111]
hυ
x6
18
11
9
Intensity (arbitrary units)
8 6 4 2 E_F
8 6 4 2 E_F
Binding energy (eV)
XBL 784 - 468

Fig. 6

VIII. THERMALLY INDUCED BREAKDOWN OF THE DIRECT TRANSITION MODEL*

Shevchik has suggested[1] that thermal broadening leads to a more complete sampling of the first Brillouin Zone (BZ) in angle-resolved x-ray photoemission than would be expected from a rigorous direct-transition model. He expressed the angle-resolved photoemission cross-section as the sum of a k-conserving direct transition term and an atomic term, with the relative contributions of the two being governed by the Debye-Waller factor, which may be written as

$$f = \exp\left[-\left\langle (\vec{q}\cdot\Delta\vec{r}_T)^2 \right\rangle\right] \quad , \tag{1}$$

where $\vec{q} = \vec{k}_f - \vec{k}_i - \vec{k}_{h\nu}$ ($\vec{k}_f$ and $\vec{k}_i$ are the final and initial electron momentum and $k_{h\nu}$ is the photon momentum) and $\Delta\vec{r}_T$ is the instantaneous thermal displacement of an atom in the lattice.

The energy distribution function for photoelectrons <u>inside</u> a crystal is given by[2]

$$J(E_f,\vec{k}_f,h\nu) \propto \sum_{\vec{k}_i}^{\vec{k}_i \supset BZ} \sum_{E_j(\vec{k}_i)}^{E_j < E_F} \left| \left\langle E_f(\vec{k}_f) \left| \vec{A}\cdot\vec{p} \right| E_j(\vec{k}_i) \right\rangle \right|^2 \times$$

$$\delta\left(E_f(\vec{k}_f) - E_j(\vec{k}_i) - h\nu\right) \quad , \tag{2}$$

where the summations are over the initial momentum states ($\vec{k}_i$) in the first BZ and all occupied energy levels. If electron transport and surface transmission do not alter N in some unknown way, an experimental

energy distribution curve (EDC) can be obtained by summing Eq. (2) over the final energy and momentum states (E_f and $\vec{k}_f$) allowed by the finite angular resolution of a measurement. If a tight-binding initial-state and plane-wave final-state are assumed[3], the matrix element of Eq. (2) demonstrates a temperature dependence similar to diffuse scattering theory;[4] i.e.,

$$|\langle e^{i\vec{k}_f\cdot\vec{r}}|\vec{A}\cdot\vec{p}|E_j(\vec{k}_i)\rangle|^2 \propto \cos^2\gamma \; f \; \sigma_{ij}(\vec{k}_f) \left\{\delta(\vec{q}-\vec{G}) + \left(1-\delta(\vec{q}-\vec{G})\right)\left[(k_BT)\frac{|\vec{q}|^2}{|\vec{q}-\vec{G}|^2}\,\phi_1 + (k_BT)^2|\vec{q}|^4\,\phi_2(\vec{q}) + \ldots\right]\right\}. \qquad (3)$$

Here γ is the angle between the electric field polarization vector and $\vec{k}_f$, $\sigma_{ij}(\vec{k}_f)$ is the atomic cross section,[5] $\vec{G}$ is a reciprocal lattice vector, k_B is the Boltzmann constant, and ϕ_1 and $\phi_2(\vec{q})$ involve sums over phonon modes familiar from first- and second-order temperature diffuse scattering.[4] In Eq. (3) it is assumed that the temperature is high enough that equipartition holds for the phonon modes.

According to Eq. (3) there are two contributions to the photoemission spectrum; one from direct transitions ($\vec{q}-\vec{G}=0$) and one from a phonon-assisted indirect transitions process. With increasing temperature or phonon energy this latter process will increase in importance relative to the former. For room-temperature photoemission studies the direct transition process should dominate in most metals at ultraviolet photoemission (UPS) energies, while the phonon-assisted process is

expected to contribute most of the spectral intensity at x-ray photoemission (XPS) energies.[1] This can explain why the direct transition model fits experiment at low energies[6,7] while a model based on the atomic cross section $\sigma_{ij}(\vec{k}_f)$ in Eq. (3) works better at high energy.[5,8] Shevchik noted that either of these limiting cases might be altered by varying the temperature, i.e., cooling in the XPS case to remove thermal disorder and emphasize direct transitions or heating in UPS to decrease f and emphasize phonon assisted transitions. The latter approach is used here to test the predicitons of Eq. (3). The recently-discovered "s-p band" resonance[7] in normal photoemission from Cu(110) at $h\nu = 45$ eV was employed because of its very high sensitivity to the exact portion of the BZ being sampled. This resonance actually arises as the 6th valence band approaches E_F between Γ and K, where Band 6 has mostly d-character. Accordingly it is called the Band 6 resonance.

A single crystal of copper was cut with a (110) surface orientation and cleaned as described previously.[7] It was heated with a button heater mounted on a two-axis manipulator. Spectra taken in the experimental geometry of Ref. 7 at 25°C, 200°C, 400°C, 600°C, and 800°C are shown in Fig. 1. A total of three heating cycles were carried out, with two different heaters and manipulators. The spectral variations with temperature were reversible and reproducible. Several possible sources of systematic error were tested and eliminated. Of most concern was the angular sensitivity of the resonance. The button heater was non-inductivity wound: magnetic fields induced by the heater and leads were calculated to deflect the electrons by less than 1°. Spectra taken at

high temperatures but with the heater off proved to be independent of the heater current. That the observed effect was not due simply to dimensional variations with temperature (i.e., rotation of the sample) was confirmed both by visual inspection and by varying the sample orientation at high temperatures.

Experiments were also performed on the same crystal in a separate LEED chamber. The current through the button heater did not visibly deflect the LEED pattern observed at low beam voltages, nor did increasing temperature alter the LEED pattern (i.e., no faceting occurred). The spots merely lost intensity until they blended into the background at the higher temperatures ($\sim 800^{\circ}$C), in accord with LEED theory.[9] Figure 2 shows the intensity variation of the (00) LEED spot for a 26 volt incident beam as a function of temperature. Thus, it is seen that the scattering of low energy electrons is also strongly perturbed by the thermal effect.

The Band 6 resonance at 0.5 eV binding energy is an extremely sensitive indicator of the direct transition channel, because this peak arises only through transitions from a band that goes through E_F steeply between Γ and K. As phonon-assisted processes become more important with increasing temperature, this peak decreases dramatically in intensity, as expected. In Fig. 3a the Band 6 intensity is plotted versus sample temperature. Also shown are plots of f^n (n = 1,2,3), where the values of $\langle \Delta r_x^2 \rangle$ used were bulk mean-square deviations for copper measured by temperature diffuse scattering.[10] Calculations for a (110) surface layer are three times the bulk value, and decay exponentially to the

bulk value by the fifth layer. The inelastic mean free path for 45 eV electrons at room temperature is ≈ 5 Å.[12] Since fcc (110) planes are separated by half the nearest-neighbor distance; i.e., 1.3 Å for Cu, the effective mean-square displacement seen in the photoelectron spectrum should be larger than the bulk value. Our data are consistent with this expectation: they agree best with $n > 1$.

Another noteworthy change with temperature occurs in the main d-band peak itself. At room temperature this peak shows at least three components, corresponding to the band energy positions at $k_x = k_y \cong -0.5$ in the BZ.[7] At high temperatures the d-band peak becomes asymmetric, with more intensity at the top if the bands, until, at 800° C, the spectrum resembles that of polycrystalline copper for $h\nu$ = 40-50 eV.[13] For copper, an electron-phonon interaction can change the electron wave vector from the Γ point to anywhere within the BZ with no more than a 30 meV[14] change in the electron energy, thus allowing more of the k states in the BZ to be sampled without greatly disrupting their energy distribution. In Fig. 3b the ratio of indirect to direct transitions is plotted as a function of temperature, assuming two different values for the ratio at room temperature. This plot bears out the <u>temperature</u> dependence predicted by Eq. (3). It is noteworthy that the total integrated valence-band intensity in the spectra in Fig. 1 is nearly (within 5%) constant with temperature, indicating that f and the power series governing the indirect transition intensity balance each other.

Additional spectra at two other photon energies (Fig. 4) are completely consistent with this interpretation. At $h\nu$ = 80 eV, at room

temperature the bands are being sampled near Γ.[7] There is thus no intensity in the "s-p band" region, $0 < E_B < 2$ eV. At high temperatures, however, thermal broadening facilities sampling over more of the BZ and the familiar "s-p band" plateau appears. At $h\nu = 140$ eV the reverse occurs. The "s-p band" region is initially unusually intense, mainly because Band 6, which gives rise to the resonance at $h\nu = 45$ eV, is being sampled on the other side of the BZ ($k_x = k_y \cong + 0.5$).

Momentum broadening due to thermal diffuse scattering has a marked effect on the Cu spectra. Increasing temperature broadens the d-band region of the spectra of Cu (110) collected at $h\nu = 80$ eV by ~0.15 eV, which is five times the maximum phonon energy for Cu. This broadening, as well as the dramatic intensity loss of the band six resonance of $h\nu = 45$ eV, is due to sampling a larger number of states in momentum space. As with momentum broadening caused by finite photoelectron attenuation lengths, a small amount of momentum smearing due to phonon excitations can change the energy distribution curves of ARPES spectra drastically due to the dispersion of the initial state bands. An idea of how much smearing temperature effects cause may be gained by comparing the 600° spectrum of Fig. 1 of this chapter to the room temperature spectrum at $h\nu = 130$ eV shown in Fig. 2 of Chapter V. The similarity of the spectra reveals that the effective momentum broadening in the two cases is roughly equivalent.

The effect of thermal disorder on photoemission spectra is now established. More work is needed to test its range of applicability. It is already clear, however that many uses can be made of this effect to

elucidate atomic properties in solids. It is also clear that thermal disorder is an essential ingredient in understanding the transition of ARPES spectra from UPS energies to the XPS regime, because of the dependence of the Debye-Walter factor on the $\vec{G}$ - vector, and thus the kinetic energy, of the photoelectron.

REFERENCES

*This chapter appeared in part as "Thermally Induced Breakdown of the Direct Transition Model in Cu," R. S. Williams, P. S. Wehner, J. Stöhr and D. A. Shirley, Phys. Rev. Letts. 39, 302 (1977).

1. N. J. Shevchik, private communication, 1977.
2. See for example D. E. Eastman, in Proceedings of the Fourth International Conference on Vacuum Ultraviolet Radiation Physics, Hamburg, July 1974, edited by E. Koch, R. Haensel, and C. Kunz (Pergamon, Vieweg, 1974).
3. J. W. Gadzuk, Phys. Rev. B10, 5030 (1974).
4. B. E. Warren, X-ray Diffraction, (Addison-Wesley, 2969), p. 159-169.
5. F. R. McFeely, J. Stöhr, G. Apai, P. S. Wehner and D. A. Shirley, Phys. Rev. B14, 3273 (1976).
6. L. F. Wagner, Z. Hussain, and C. S. Fadley, Solid State Commun. 21, 257 (1977).
7. J. Stöhr, P. S. Wehner, R. S. Williams, G. Apai, and D. A. Shirley, Lawrence Berkeley Laboratory Report LBL-6066, to be published.
8. P. S. Wehner, J. Stöhr, G. Apai, F. R. McFeely, and D. A. Shirley, Phys. Rev. Lett. 38, 169 (1977).
9. G. E. Laramore and C. B. Duke, Phys. Rev. B2, 4783 (1970).
10. International Tables for X-ray Crystallography, ed. C. H. McGillavry, G. D. Rieck, and K. Lonsdale (The Kynoch Press, Birmingham, England, 1962) p. 237.

11. R. F. Wallis, B. C. Clark, and R. Herman, Phys. Rev. 167, 652 (1968).

12. I. Lindau and W. E. Spicer, J. Electron Spectr. and Rel. Phen. 3, 409 (1974).

13. A. D. McLachlan, J. G. Jenkin, J. Liesegang, and R. C. G. Leckey, J. Electron Spectr. and Rel. Phen. 5, 593 (1974); J. Stöhr, F. R. McFeely, G. Apai, P. S. Wehner, and D. A. Shirley, Phys. Rev. B14, 4431 (1976).

14. R. M. Nicklow, G. Gilat, H. G. Smith, L. J. Raubenheimer, and M. K. Wilkinson, Phys. Rev. 164, 922 (1967).

FIGURE CAPTIONS

Fig. 1. Temperature dependence of the normal photoemission spectrum from a Cu(110) crystal at $h\nu$ = 45 eV.

Fig. 2. The (0 0) LEED spot intensity for a 26 volt incident electron beam. The dashed line is the spot intensity versus sample temperature curve as measured by a spot photometer (the upward turn seen near 700° C is due to light emitted by the sample and heater). The dotted line is a measure of the background light on the LEED screen, collected by moving the spot photometer just off the (0 0) LEED spot. The solid curve is the difference between these two measurements and represents the actual I vs. T behavior of the LEED spot.

Fig. 3. a) Experimental intensity of the peak at ~ 0.5 eV binding energy in Fig. 1 (Band 6 resonance) as a function of temperature (full circles connected by a dashed line) as compared to the Debye-Waller factor f^n (solid lines). The different curves for f^n correspond to calculations assuming a mean-square displacement of n times the bulk value.

b) Ratio of indirect to direct transitions as derived from the spectra in Fig. 1 versus temperature. For the data points shown as squares and triangles we have assumed that at room temperature the main d-band peak is composed of 100% and 85% direct transitions, respectively.

Fig. 4. Normal emission ARPES spectra of the Cu(110) face collected of room temperature (solid lines) and 600° C (dashed lines) for photon energies of 80 and 140 eV.

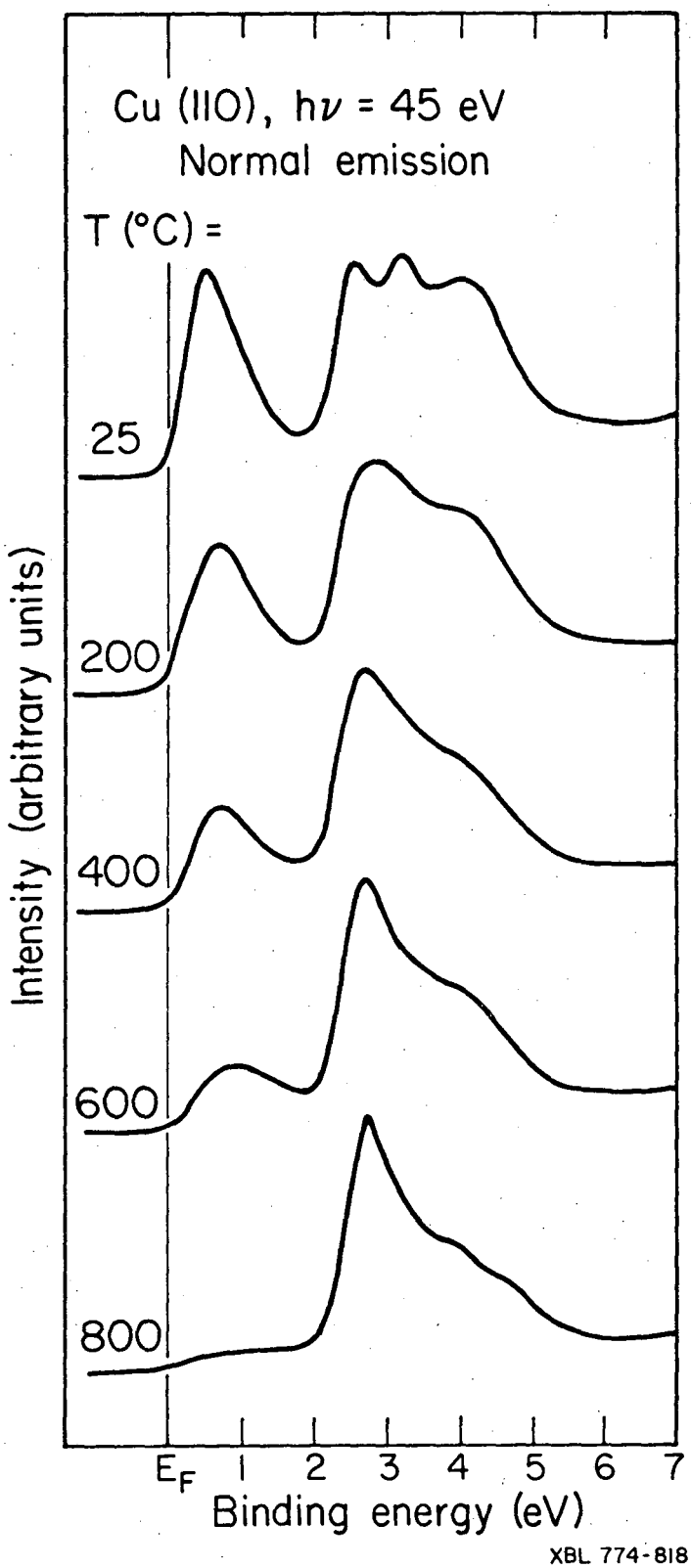
Cu (110), hν = 45 eV
Normal emission
T (°C) =
25
200
400
600
800
Intensity (arbitrary units)
E_F
1
2
3
4
5
6
7
Binding energy (eV)
XBL 774-818

Fig. 1

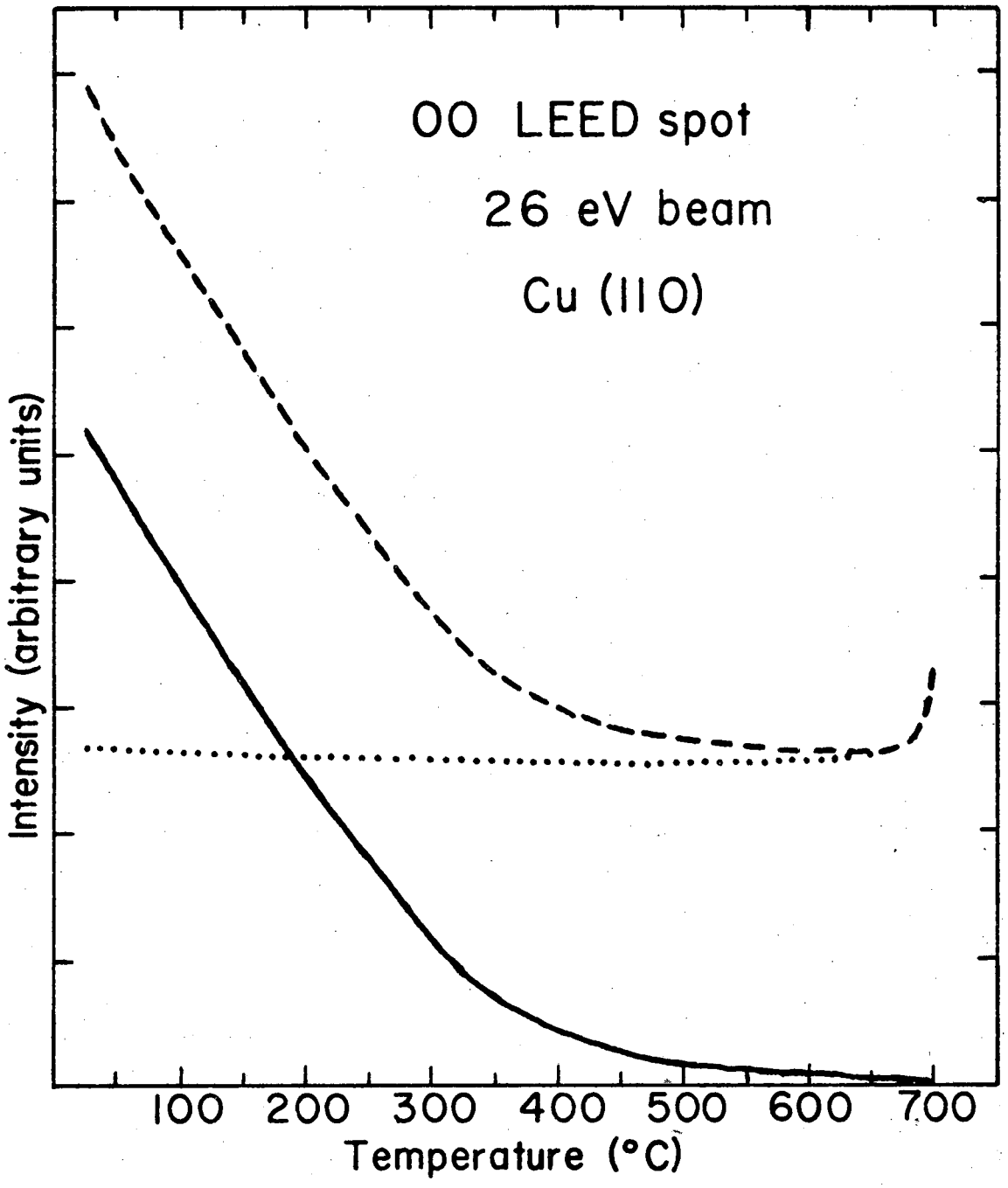

XBL 785-8689

Fig. 2

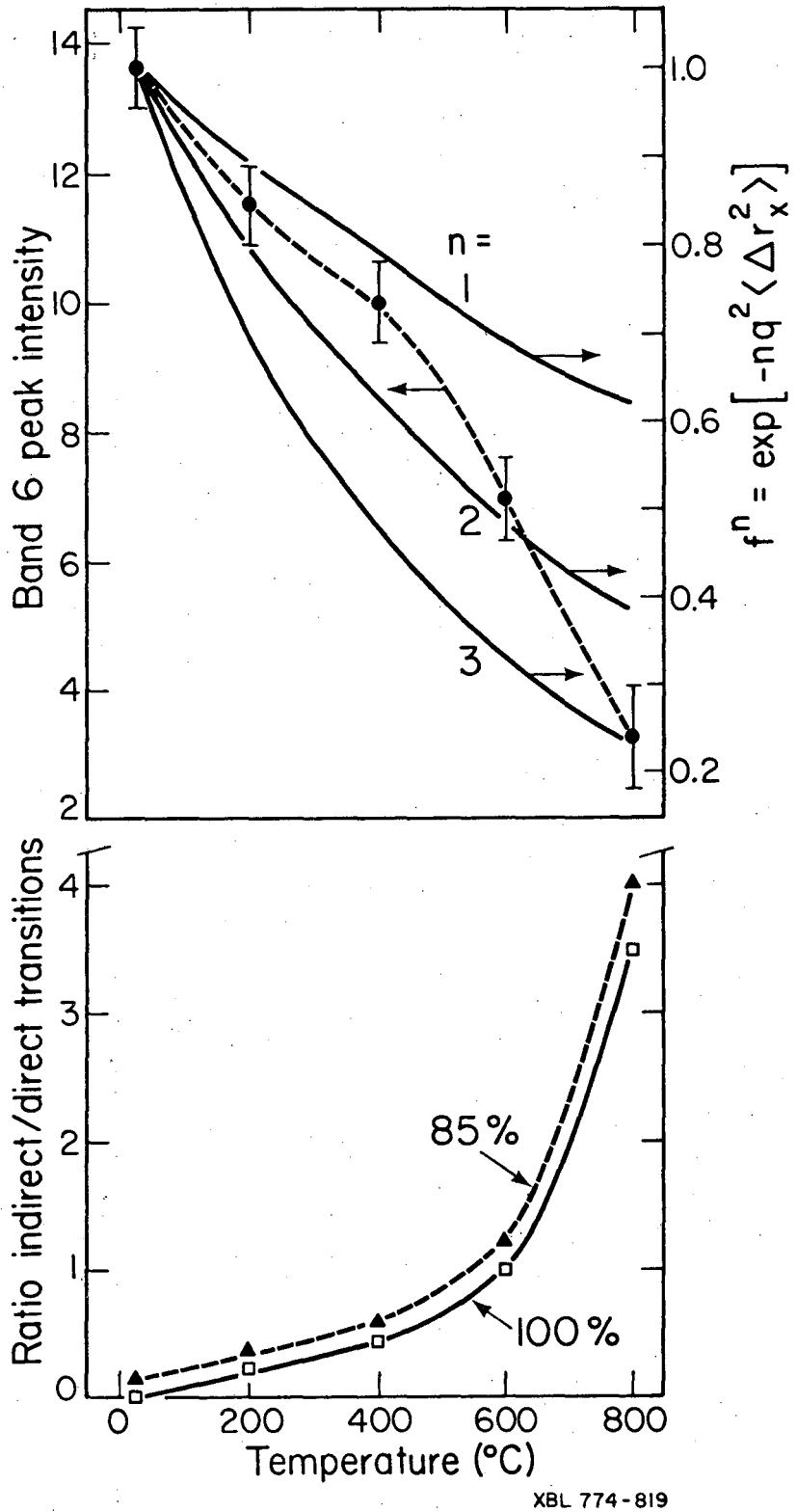
Band 6 peak intensity
$f^n = \exp[-nq^2\langle\Delta r_x^2\rangle]$
n =
1
2
3
Ratio indirect/direct transitions
85%
100%
Temperature (°C)
XBL 774-819

Fig. 3

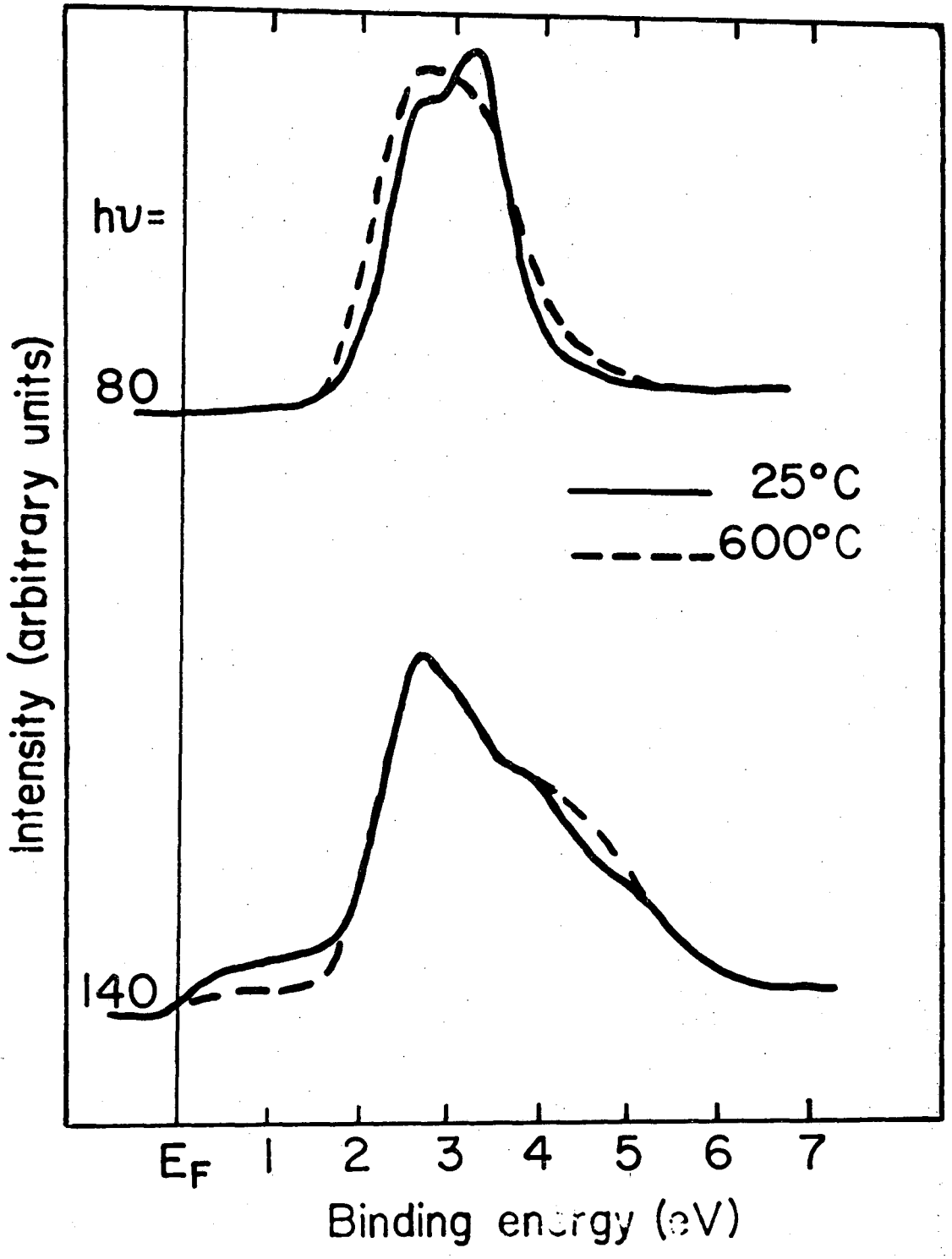

XBL 785-8690

Fig. 4

ACKNOWLEDGEMENTS

The attainment of a Ph.D. degree is the culmination of many years of hard work and sacrifice which is impossible without the support of a great many people. This is my chance to thank those who have helped me pursue my interest in science from rural southern Texas to the Department of Chemistry at Berkeley, California. The chase has been long and often frustrating, but the rewards have been many; I have found the study of science truly exhilirating, and I have never, ever been bored.

First I must acknowledge the love, encouragement and enthusiastic support of my parents, and I deeply regret that my father did not live to see me achieve this goal. My mother has been a constant source of strength to me, for which I am grateful beyond words to express.

My first fledgling steps as a scientist were taken at Rice University; I owe a special debt of thanks to Professors Robert Curl and Phillip Brooks and many more of my friends there gor getting me started.

The biggest influence on my graduate career has been Professor David Shirley, my thesis supervisor. His qualities as a scientist, the depth of knowledge, physical insight and command of theory, have been a continual source of amazement and inspiration to me, and he is besides a damn nice guy. I have had the good fortune do work with and learn from many members of (and visitors to) our research group: Dr. Gary Schwartz, Dr. Salim Banna, Dr. Bernice Mills, Dr. Richard Streater, Dr. Sefik Suzer, Dr. Shuit-Tong Lee, Prof. Eckart Matthias, Dr. Teikichi

Sasaki, Prof. Peter Sherwood, Prof. Nicholas Winograd, Dr. Paolo Perfetti, Dr. Vic Rehn, Mr. Alan Ewing, Mr. Peter Young, Mr. Richard Rosenberg, Mr. Michael White, Mr. Erwin Poliakoff, Mr. Dennis Trevor, Mr. Kenneth Mills, and Mr. James Wong. I am especially indebted to Dr. Richard Martin, Prof. Read McFeely, and Dr. Steven Kowalczyk for their scientific guidance and friendship. Mr. David Denley, Mr. Steven Kevan, and Mr. Richard Davis have been valuable additions to the solid state research group, and their efforts in behalf of this last year's research are gratefully acknowledged. My research colleaques throughout most of my graduate career have been Dr. Joachim Stöhr, Dr. Gus Apai, and Dr. Paul Wehner; I thank them sincerely for the years we spent collecting and arguing over data, because in the last analysis it was teamwork that brought us so far so fast.

The success of most of the scientific programs reported in this dissertation has been due in large part to the efforts of several of the people on the staff at Lawrence Berkeley Laboratory. Mr. Joseph Katz and Mr. Richard Strudwick of the electronics support group have rescued many experiments from disaster with their prompt, efficient, and remarkably cheerful work. The counseling of Mr. Gene Miner, Mr. Dick Escobales, and Mr. Don Malone in engineering matters has been invaluable. Mr. Ed Voronin and Mr. Charley Butler provided excellent shop support whenever needed. Mrs. Wini Heppler deserves special thanks not only for her diligent technical services but also for her friendship, which I value greatly. Mrs. Karen Janes has worked remarkably hard at preparing manuscripts and in handling the tangles of administrative red tape, for

which she should be granted Sainthood.

My graduate career has also been enriched by my associations with Prof. George Jura, Prof. Kenneth Pitzer and Prof. Leo Falicov, all of Berkeley. I have further benefited greatly through interactions with members of Prof. William Spicer's research group at Stanford University; in particular I wish to thank Dr. Ingolf Lindau, Dr. Pierro Pianetta, Mr. Dan Ling, Mr. Mike Garner and Mr. Jeff Miller. Most of the experiments reported in this thesis were performed at the Stanford Synchrotron Radiation Laboratory, and the cooperation of the staff of the facility, Dr. Herman Winick, Mr. Ben Salsberg, Mr. Axel Golde, Mr. Ralph Gaxiola and many others was essential to the work done there. In this line, the work of Dr. Bob Bachrach of Xerox Palo Alto in getting us started in our efforts at Stanford is acknowledged.

I have also enjoyed the assistance and friendship of dozens of other people too numerous to mention. However, I must name here some people who have been very special to me, the folks with whom I have lived (and who put up with me) for the past two years: Ms. Cathy Pearsall, Ms. Shirley Richberger, Mr. Bill Butler, and Ms. Renelle Johnson, and more recently Ms. Kirsten Jacobs and Ms. Carol Young.

I have much to be thankful for, and so many to be thankful to. The years preceding my doctorate, have been very fulfilling, and the opportunities I have been given bountiful. I am grateful for my career in science not only because of the discoveries I have made concerning the physical world, but also for what I have learned about

myself and for all the exceptional people I have met. I close with a quotation from a fictional character, Jeremy Hilary Boob, Ph.D., the nowhere man,

"Ad hoc, Ad loc,
Quid Pro Quo,
So little time
And so much to know."

Work supported by the U. S. Department of Energy.

This report was done with support from the Department of Energy. Any conclusions or opinions expressed in this report represent solely those of the author(s) and not necessarily those of The Regents of the University of California, the Lawrence Berkeley Laboratory or the Department of Energy.

TECHNICAL INFORMATION DEPARTMENT
LAWRENCE BERKELEY LABORATORY
UNIVERSITY OF CALIFORNIA
BERKELEY, CALIFORNIA 94720